



**UiT** The Arctic University of Norway

Faculty of Science and Technology

Department of Physics and Technology

**Numerical simulations and stochastic modeling of intermittent  
fluctuations in magnetized plasmas**

**Gregor Dechristoforo**

A dissertation for the degree of Philosophiae Doctor, March 2021





## Abstract

The exhaust of particles and heat in the boundary of contemporary magnetic confinement experiments remains to this day a major obstacle on the road to commercially viable fusion energy production. It is recognized, that coherent structures of hot and dense plasma, called blobs or filaments, are the dominant mechanism for cross-field particle transport. These filaments are created by plasma turbulence at the outboard midplane and move radially outwards driven by interchange motions. This leads to high average particle densities and relative fluctuation levels in the scrape-off layer, which increases plasma-wall interactions.

Time series of the plasma density measured at a fixed point using either Langmuir probes or gas puff imaging have shown highly intermittent fluctuations across a variety of devices, plasma parameters and confinement modes. Recent statistical analysis of measurement data time series has revealed that the fluctuations are well described as a superposition of uncorrelated exponential pulses with fixed duration and exponentially distributed pulse amplitudes, arriving according to a Poisson process.

Due to the complexity of the physics involved in the boundary of fusion devices, numerical simulations are utilized to gain an accurate description of scrape-off layer plasmas. This approach requires a validation metric for simulations of plasma turbulence such as the statistical framework based on filtered Poisson processes. In this thesis, well-established models for scrape-off layer plasmas are analyzed. These models use two-fluid equations simulating plasma evolution in the two-dimensional plane perpendicular to the magnetic field. Time series of the plasma density are measured at a fixed point and their fluctuation statistics are compared to experimental measurements utilizing the statistical framework. This includes probability density functions, power spectral densities and conditionally averaged waveforms. In addition, simulations of a population of seeded blobs are performed in order to study the effects of blob interactions. It is shown that the fluctuation statistics of single-point measurements in simple numerical models stand in excellent agreement with their experimental counterparts. This work thereby sets a new standard and methodology for validating scrape-off layer turbulence simulations.



## Acknowledgements

After three and a half years as a PhD student, I would like to thank a number of people who have supported me on this journey. First, I would like to thank my main supervisor, Odd Erik Garcia. In addition to his guidance and support, Odd Erik also gave me the opportunity to participate at summer schools at CCFE and MIT, visit DTU for two weeks during my first year and spend a whole year at CCFE. Visiting different research facilities and meeting many gifted scientists was one of the highlights during this time.

I would also like to thank Fulvio Militello for hosting me at CCFE and proofreading parts of this thesis. Our weekly catch-ups in the last year and a half were extremely insightful and productive. I am grateful to him reserving time for me even though I am not directly supervised by him.

I am very grateful for being part of such friendly and supportive research groups. These include Audun Theodorsen, Ralph Kube, Juan Manuel Losada and Magdalena Korzeniowska at UiT. From CCFE these include John Omotani, Tom Nicholas, Fabio Riva, Sarah Newton and Nick Walkden as well as Matthias Wiesenberger at DTU. Further thanks go to my office mates, Patrick Stoll, Sindre Fritzner, Tuomas Heiskanen, Tom Farley, Daljeet Singh Gahle, Enrique Miralles and Joe Allcock. Raheesty Nishta Nem deserves my gratitude for proof-reading my thesis and giving me valuable comments. I am also grateful to the University of Tromsø – The Arctic University of Norway for funding my PhD.

On a less academic note, I would like to thank my landlord in Oxford, Michael Butcher, for letting Sajidah and me stay in his flat during the UK-wide lockdown due to the COVID-19 pandemic. Being able to stay together with Sajidah made this challenging time much easier. Thanks also to my friends in Tromsø and Oxford, I have always been looking forward to spending time with you during band practice and other occasions.

Vielen Dank an meine Familie für eure Unterstützung und euer Verständnis für die örtliche Distanz. Auch wenn ich euch pandemiebedingt schon lange nicht mehr persönlich sehen konnte, bleibt ihr in meinem Herzen.

Finally, I would like to thank Sajidah for her patience, laughter and support. This PhD would not have been as joyful without you.



# Contents

<b>1 Fluctuations in magnetized plasmas</b>	<b>1</b>
1.1 Nuclear fusion . . . . .	2
1.2 Magnetic confinement . . . . .	2
1.3 Radial transport in the SOL . . . . .	4
1.4 Intermittent fluctuations in the SOL . . . . .	6
1.5 Plasma filaments . . . . .	11
1.6 Numerical modeling of SOL plasmas . . . . .	16
<b>2 Reduced fluid models for SOL plasmas</b>	<b>21</b>
2.1 Braginskii fluid equations . . . . .	21
2.2 Drift reduction . . . . .	22
2.3 Further approximations and simplifications . . . . .	25
2.4 Reduced two-fluid model . . . . .	29
2.5 Idealized interchange model . . . . .	32
<b>3 Stochastic modeling</b>	<b>35</b>
3.1 Filtered Poisson Process . . . . .	35
3.2 Moments and PDFs . . . . .	38
3.3 Second order statistics . . . . .	39
3.4 Excess time statistics . . . . .	41
3.5 Density profiles . . . . .	42
3.6 Deconvolution method . . . . .	44
<b>4 Summary of Papers</b>	<b>47</b>
<b>5 Conclusion and future work</b>	<b>51</b>
<b>Bibliography</b>	<b>53</b>

**Paper I:**

Intermittent fluctuations due to Lorentzian pulses in turbulent thermal convection	73
--	----

**Paper II:**

Dirac comb and exponential frequency spectra in chaotic dynamics	77
--	----

**Paper III:**

Numerical turbulence simulations of intermittent fluctuations in the scrape-off layer of magnetized plasmas	105
---	-----

**Paper IV:**

Blob interactions in 2D scrape-off layer simulations	109
--	-----

# 1 | Fluctuations in magnetized plasmas

Nuclear fusion is the process by which light atomic nuclei fuse together to form heavier nuclei and smaller by-products, releasing large amounts of energy. Since the middle of the last century, different strategies to harness fusion energy have been investigated. At present magnetic confinement is considered the most promising approach to deliver fusion power in the foreseeable future. To this day, however, controlling and harnessing nuclear fusion remains one of the greatest engineering challenges. Magnetically confined fusion requires the fuel to have enormously high temperatures while the vessel walls must be at room temperature or lower. The heat exhaust problem has therefore famously been referred to as “probably the main challenge towards the realization of magnetic confinement fusion” [1]. A detailed understanding of the intricate physics involved in the boundary of fusion devices therefore remains crucial in order to provide fusion energy as a sustainable and CO<sub>2</sub> emission free option for the future energy grid.

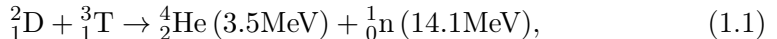
This thesis project is concerned with numerical simulations of boundary plasmas and a statistical analysis of plasma fluctuations. These simulations require a method of validation with experimental observations. In this thesis, a recently developed stochastic model for fluctuation statistics is utilized to identify suitable numerical models for boundary plasmas.

This thesis is structured as follows: This chapter delivers a brief overview of the current state of knowledge on the boundary of fusion plasmas. The main emphasis will lie on plasma fluctuations for reasons that will become clear over the course of this chapter. Chapter 2 is dedicated to the derivation of reduced fluid models for the boundary plasma, which are used for the numerical simulations presented in this thesis. Chapter 3 introduces the Filtered Poisson Process, a phenomenological model which is able to describe all relevant statistical properties of plasma fluctuations in the boundary region. Chapter 4 delivers a summary of the publications and unpublished manuscripts included

in this thesis and Chapter 5 provides the conclusion and outlook. The published papers and unpublished manuscripts are attached at the end of this thesis, representing the main contribution of this work.

## 1.1 Nuclear fusion

Although a multitude of nuclear reactions produces fusion energy, only the reaction of the hydrogen isotopes Deuterium  ${}_1^2\text{D}$  and Tritium  ${}_1^3\text{T}$ ,



is feasible with the prevailing technology. This reaction produces a helium particle  ${}_2^4\text{He}$  and a neutron  ${}_0^1\text{n}$  together with 17 MeV of kinetic energy. This exothermic, single-step reaction has the largest fusion cross section at the lowest temperatures of all potential reactions. In addition, the low atomic number results in a lower electrostatic potential that must be overcome, making this the most promising candidate for fusion power plants. With one in 6420 hydrogen atoms in sea water, Deuterium can be considered abundant, while the radioactive Tritium must be obtained from breeding of the lithium isotope  ${}_3^6\text{Li}$ , which can be found in minerals from the Earth's crust. Due to the high temperature of approximately  $10^8\text{ K}$  for D-T fusion, no solid vessel could achieve steady-state confinement at these temperatures. The fuel would instantaneously lose its heat when colliding with the vessel walls. In order to achieve long enough energy confinement times, required for producing fusion power in a steady-state, a different approach has to be adopted. Since all hydrogen particles are fully ionized at these temperatures, i.e., in a plasma state, the particles can be confined with magnetic fields [2].

## 1.2 Magnetic confinement

Magnetic Confinement Fusion (MCF) chooses the approach to use the gyro-motion of charged particles in a magnetic field to confine the plasma. An array of cylindrical solenoidal coils creating a uniform magnetic field can confine the plasma in the radial direction, however charged particles moving along these field lines can intersect material surfaces at both ends. The simplest method to mitigate these end losses is to bend the magnetic field to connect the ends, which results in a torus shape. The resulting inhomogeneity of the magnetic field due to its curvature and radial gradient, however, complicates plasma confinement. Since a gyrating particle experiences a stronger magnetic field on one side of its orbit than the other, it will experience a change in its gyration

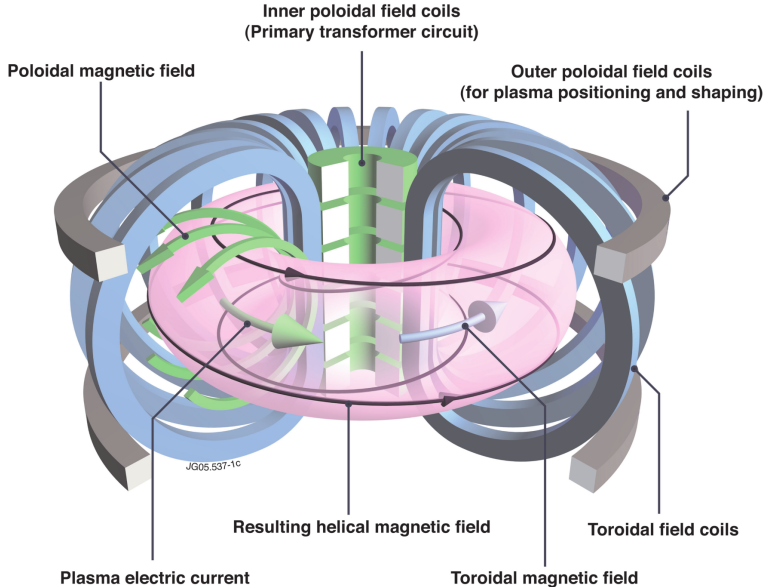


Figure 1.1: Schematic illustration of a tokamak device [3].

radius, resulting in a net drift which is in opposite direction for ions and electrons. These “guiding-center drifts” which are perpendicular to the magnetic field  $\mathbf{B}$  and its variation  $\nabla B$ , create a vertical electric field  $\mathbf{E}$ . The resulting fields give rise to another guiding-center drift, the electric or  $\mathbf{E} \times \mathbf{B}$  drift, which moves both negatively and positively charged particles radially outwards. A toroidal plasma current, induced by a central transformer, creates a poloidal magnetic field. Introducing this poloidal field results in helical magnetic field lines, which mitigates this problem since the guiding-center drifts cancel out as the particles rotate poloidally while following the magnetic field lines. Outer poloidal field coils are used in addition to shape and position the plasma column. This concept is known as a tokamak, invented in the 1950s in the Soviet Union and to this day considered to be the most promising route for plasma confinement and nuclear fusion. A schematic illustration of the tokamak concept is shown in Fig. 1.1.

Despite the advanced magnetic geometry of tokamak devices which establish a perfect equilibrium, experimental measurements indicate that large amounts of particles and heat are still transported across the magnetic flux surfaces. This transport is caused by plasma turbulence, which is particularly strong at the boundary of the device. All modern tokamak experiments adopted the “divertor configuration”, which is illustrated in Fig. 1.2. This configuration is achieved by creating a magnetic null point (X-point) in the

poloidal plane with a divertor coil carrying a current parallel to the plasma current. Within this point, the magnetic field lines are closed with the last closed flux surface (LCFS), often referred to as the separatrix. The outward region is called the Scrape-Off Layer (SOL), in which the magnetic field lines intersect the divertor plates. Ideally, all plasma leaking from the core through the separatrix into the SOL flows down to the divertor plates where it interacts with the material surfaces, with little to no influence on the fusion process in the core. The poloidal flux expansion near the X-point increases the distance of the magnetic field lines to the divertor plates, letting the plasma cool down before it reaches the material surfaces. Additional precautions, such as tilted target plates, buffers of neutralized gas in front of the target (divertor detachment) or installing a second divertor above the plasma column (double-null configuration) are applied in some experiments to reduce the heat flux on the divertor plates further. Despite all these efforts, plasma turbulence leads to highly intermittent bursts of particles and heat propagating through the SOL to the main chamber walls, leading to erosion, damages of sensitive equipment and the release of impurities into the core plasma, where they may degrade confinement and create radiative instabilities. An accurate description for the cross-field transport in the SOL is therefore required in order to predict and handle plasma and heat exhaust in future devices [2].

### 1.3 Radial transport in the SOL

Historically, the first attempts to describe cross-field transport in tokamak plasmas used a simple diffusive model in the SOL [4]. In this case the transport follows Fick's law

$$\Gamma_{\perp} = -D_{\perp} \frac{\partial n}{\partial r}, \quad (1.2)$$

where  $\Gamma_{\perp}$  stands for the cross-field particle flux,  $D_{\perp}$  is the diffusion coefficient estimated from the plasma parameters [5],  $n$  stands for the plasma density and  $r$  for the radial/cross field dimension. This model, however, fails to account for experimental observations, requiring significantly higher diffusion coefficients than expected from classical or Bohm diffusion [6, 7]. Experimental radial profiles in the SOL could only be reproduced by numerical simulations by assuming large cross field drifts or high effective diffusion coefficients  $D_{\perp}^{\text{eff}}$ , often referred to as “anomalous” diffusion [8]. It was expected that the SOL is dominated by strong flows parallel to the magnetic field, transporting most of the plasma to the divertor targets, resulting in exponential profiles with constant  $D_{\perp}^{\text{eff}}$ . These assumptions were refuted by experimental measurements such as presented for the TCV tokamak in Fig. 1.3. Here, the variable  $\rho$  stands for the distance to the separatrix and the dashed line indicates the beginning

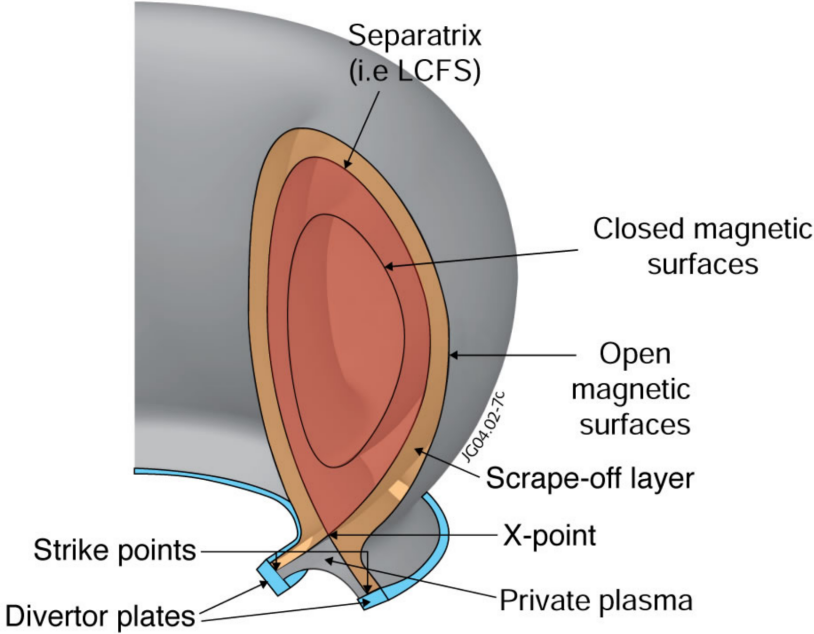


Figure 1.2: Schematic illustration of the boundary region of a tokamak in a divertor configuration [3].

of the wall shadow, the region in which the magnetic field lines interact with the vessel walls. For the lowest line-averaged densities  $\bar{n}$  a sharp decay in the density profile is observed close to the separatrix, with a much slower decay radially outwards. These regions are referred to as the near-SOL for the region of steep profiles and far-SOL, respectively [10]. For increasing  $\bar{n}$  the break point between these two regions moves radially inwards, resulting in a long decay length in the whole SOL, called broadening [11]. This radial variation is also observed in other tokamak experiments such as Alcator C-Mod, MAST, NSTX, ASDEX, JET and DIII-D [12–18], and in numerical simulations with SOL turbulence codes such as ESEL [19]. For a purely diffusive transport this effect requires a significant radial increase of the effective diffusion coefficient as indicated in Fig. 1.4 for Alcator C-Mod plasmas, questioning the concept of purely diffusive transport. In the case of the DIII-D experiment, UEDGE transport simulations were unable to find any matching diffusion coefficient [21]. This motivates the introduction of an effective anomalous velocity  $v_{\perp}^{\text{eff}}$  to the diffusion model,

$$\Gamma_{\perp} = -D_{\perp}^{\text{eff}} \frac{\partial n}{\partial r} + v_{\perp}^{\text{eff}} n. \quad (1.3)$$

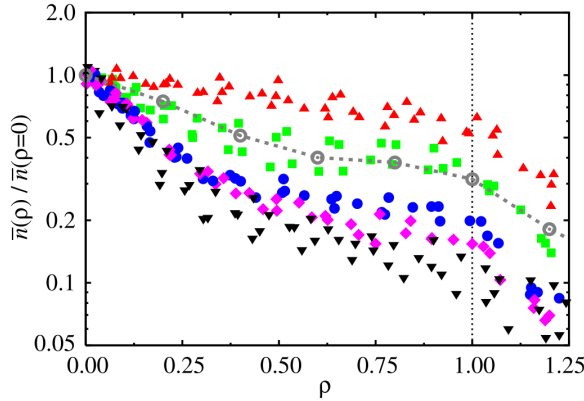


Figure 1.3: Time-averaged, radial profile of the particle density normalized to the separatrix value in the TCV tokamak. The different colored symbols refer to different line-averaged core plasma densities with the black triangles referring to the lowest and the red triangles to the highest value. Reprinted from [9], with permission from IAEA.

For an advective-diffusive transport, however, the particle flux would follow a linear relationship with the inverse density scale length  $\lambda_n$  [22] as

$$\frac{\Gamma_\perp}{n} = v_\perp^{\text{eff}} - \frac{D_\perp^{\text{eff}}}{n} \frac{\partial n}{\partial r} = v_\perp^{\text{eff}} + \frac{D_\perp^{\text{eff}}}{\lambda_n}. \quad (1.4)$$

In experimental measurements, such as for TCV shown in Fig. 1.5, no linear relationship can be found. Similar studies on the flux-gradient relation in a simple ESEL interchange model of the SOL at constant temperatures, shown in Fig. 1.6, draw an equivalent conclusion [19].

These findings clearly indicate that a different model is needed in order to describe turbulence and cross-field transport in the SOL adequately.

## 1.4 Intermittent fluctuations in the SOL

In the process of finding a better model describing plasma transport in the SOL of tokamak experiments, measurements of the relative fluctuation levels provide additional insight. Among the first experiments investigating this is the Caltech tokamak where fluctuation levels of 10-90% of the mean were measured in ion saturation current measurements in the edge [23, 24]. Similar observations were made in other experimental devices where these include the TEXT device, shown in Fig. 1.7, and in TCV, Fig. 1.8. The fluctuation profiles

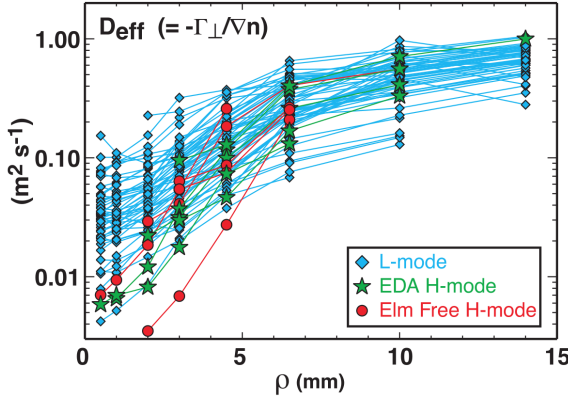


Figure 1.4: Effective diffusivity profiles for different operational modes of the Alcator C-Mod experiment. The effective diffusion coefficient must vary by several orders of magnitude in order to match purely diffusive transport models. Reprinted from [20], with the permission of IAEA.

of the TCV experiment correspond to the time averaged profiles shown in Fig. 1.3. In the low-density case the relative fluctuation levels increase radially in the near SOL and stay approximately constant in the far SOL. Note that the fluctuation levels in the far SOL are independent of the line-averaged core density. For all densities the relative fluctuation levels in the far SOL range between 0.5 and 1, indicating that the broad profiles are dominated by large fluctuations. These findings differ drastically from the plasma core, where fluctuation levels are only around 1% [25].

A more detailed picture of SOL fluctuations can be obtained by analyzing time series of the plasma parameters. These time series are typically obtained by Langmuir probes, consisting of a conducting element which is inserted into the plasma and draws a measurable current [27, 28]. Another well-known method is Gas puff imaging (GPI), where a puff of neutral gas is injected into the plasma edge, so that excitation radiation can be measured [29]. Examples for time series measured at the outboard mid-plane in the far SOL of TCV, Alcator C-Mod and KSTAR are shown in Fig. 1.9. Here,  $\tilde{\Phi}$  stands for the time series  $\Phi(t)$  normalized to have zero mean and unit standard deviation. In all three devices, the time series show strongly intermittent positive bursts, which suggests an explanation for the large relative fluctuation levels in the SOL. A stochastic model describing these fluctuations as a superposition of uncorrelated pulses was introduced in 2012 [30]. This phenomenological model, known in the context of stochastic processes as the Filtered Poisson Process

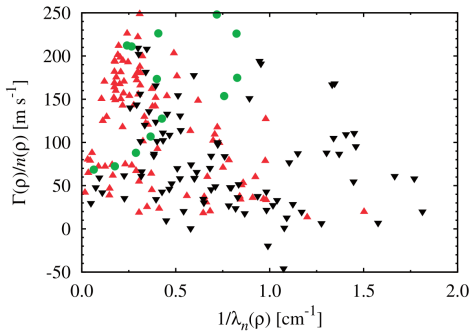


Figure 1.5: The relationship between the normalized radial particle flux and the inverse density scale length for a range of TCV experiments. Reprinted from [22], with the permission from Elsevier.

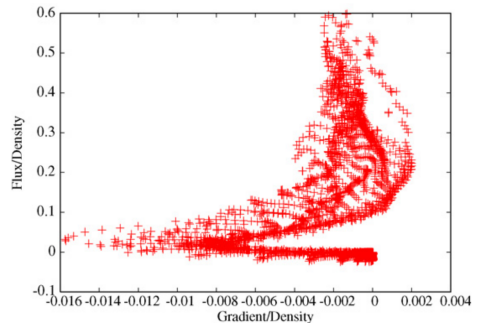


Figure 1.6: The flux–gradient relation in a simple ESEL interchange model of the SOL at constant temperatures. Reprinted from [19], with the permission from Elsevier.

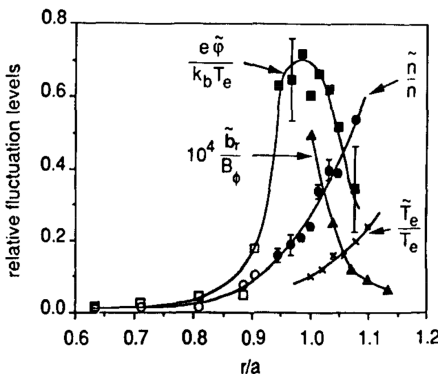


Figure 1.7: Radial dependencies of fluctuation levels of different plasma parameters in the TEXT tokamak experiment. Reprinted from [26], with the permission from Elsevier.

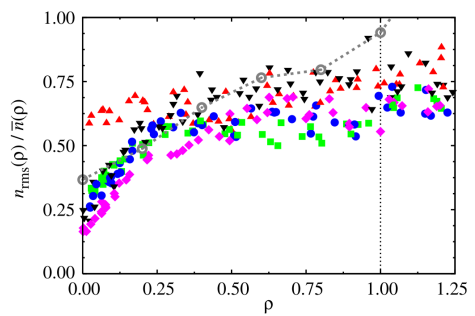


Figure 1.8: Radial profile of the relative fluctuation level of the particle density in the TCV SOL. Reprinted from [9], with permission from IAEA.

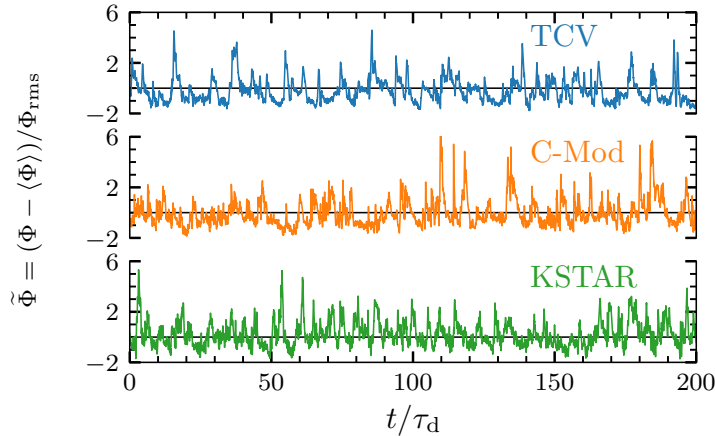


Figure 1.9: Fluctuation time series measured from different tokamak experiments. The time is normalized by the characteristic duration time of the underlying bursts. The black line indicates the mean value of the signal. Image courtesy of A. Theodorsen [39].

(FPP), remains to the day of writing this thesis the most accurate statistical description of SOL fluctuations, as all of its major assumptions and predictions agree with the statistical properties of experimental measurements [31–38]. A detailed discussion of the FPP model is provided in Chapter 3 of this thesis.

The statistical properties of the fluctuations appear to be remarkably universal across numerous tokamak experiments, confinement modes and plasma parameters. Since positive fluctuations dominate over negative ones, the probability density functions (PDFs) are positively skewed and flattened. Fig. 1.10 shows the PDFs of the ion saturation current measured in the boundary of four different devices, exhibiting almost identical results. Time series obtained at different radial positions in the boundary region of Alcator C-Mod exhibit close to normal distributions near the separatrix, whereas in the far SOL show increasingly skewed PDFs with an exponential tail towards positive values, as shown in Fig. 1.11. Collectively, all of these PDFs are well described by a Gamma distribution with a shape parameter depending on the intermittency of the time series [40]. PDFs with exponential tails towards positive events have also been observed in multiple other devices such as TCV, Tore Supra and KSTAR [9, 35, 41–45]. The skewness and kurtosis of these time series are exceeding 0 and 3 respectively, as they would be for a normal distribution. A parabolic relationship between skewness and kurtosis has been demonstrated in [46–48] which remains consistent with predictions of the FPP model [49].

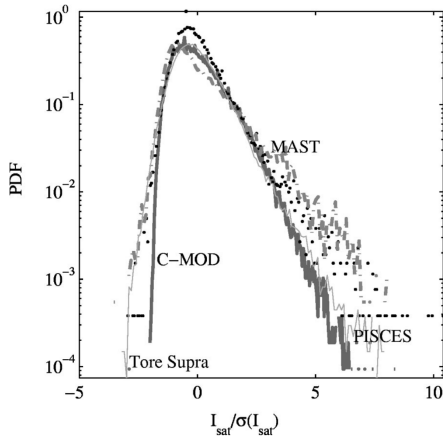


Figure 1.10: PDF of the ion saturation current in the boundary of Tore Supra, Alcator C-Mod, MAST and PISCES. Reprinted from [42], with permission from AIP Publishing.

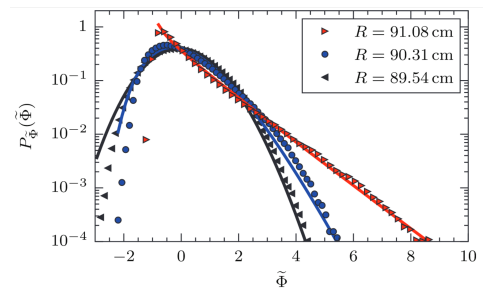


Figure 1.11: PDFs of gas puff imaging data time series at different radial positions in the boundary of Alcator C-Mod. The full lines represent the predictions of the FPP model. Reprinted from [40], with permission from IAEA.

The universality of plasma fluctuations in the SOL is also observed in the power spectral densities (PSDs) of the measured time series [36–38, 40, 50, 51]. The PSDs of time series for the ion saturation current in a variety of devices are shown in Fig. 1.12. For a given scaling factor for the frequency axis all PSDs collapse to a single curve. In contrast to the PDFs, the radial position does not seem to have any influence on the PSDs as shown for Alcator C-Mod in Fig. 1.13. In all experimental measurements the PSD remains flat for low frequencies and shows a power law decay for high frequencies. The analysis of these fluctuations utilizing the FPP framework has shown that the shape of the PSD can be attributed to the shape of the underlying pulses from the time series [52], providing further support for the stochastic model.

Apart from stochastic modeling, conditional averaging can be applied in order to reveal the shape of these large-amplitude fluctuations. Hereby all events above a certain threshold, typically 2.5 times the rms-value above the signal mean, are considered and their peak is stored within a time window. The average over all windows is referred to as the conditionally averaged waveform, showing a sharp peak with a short rise and longer decay [9, 31, 33, 35–37, 42, 44, 53]. The conditionally averaged waveform of time series acquired from the boundary of TCV are shown in Fig. 1.14. The shape of these large-amplitude fluctuations remain similar for all line-averaged core densities of the experiment and are reproducible by numerical simulations of the two-dimensional ESEL

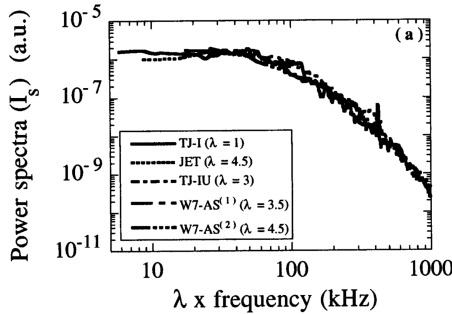


Figure 1.12: PSDs of fluctuation time series of the ion saturation current in various devices. Reprinted figure with permission from [50]. Copyright (1999) by the American Physical Society.

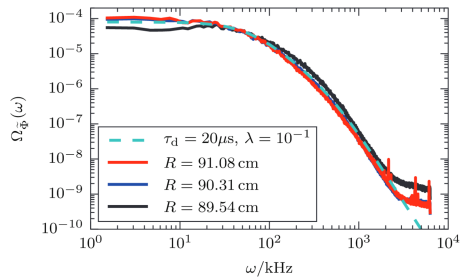


Figure 1.13: PSDs for gas puff imaging time series at different radial positions in the edge of Alcator C-Mod. The broken line shows the FPP predictions. Reprinted from [40], with permission from IAEA.

model. Fig. 1.15 shows the agreement of conditionally averaged waveforms for time series measured in different tokamak experiments and compared to an asymmetric, two-sided exponential function. Both the distribution of the maximal amplitude of the conditional structures and the waiting times between two consecutive peaks are found to be exponentially distributed [33, 35–37, 54].

In conclusion, the statistical properties of time series measured at the mid-plane boundary of tokamak devices indicate that the SOL is dominated by intermittent structures. In order to investigate the shape of these objects and to gain more information about the physical mechanisms responsible for their transport, stochastic modeling alone, however, does not suffice.

## 1.5 Plasma filaments

2D imaging diagnostics such as GPI and wide angle visible imaging reveal that edge transport in the SOL can be attributed to coherent structures. These objects have historically been featured under a variety of names, such as intermittent plasma objects (IPOs), avaloids, solitary vortices and streamers, but are most commonly referred to as filaments or blobs in recent literature. First observations of plasma filaments were made with fast cameras at the Caltech tokamak in the mid 1980’s [55–57] and with 2D probe arrays in the 1990’s [58, 59]. The importance of filaments for edge transport, however, has only been considered at the discovery of the main chamber recycling regime at Al-

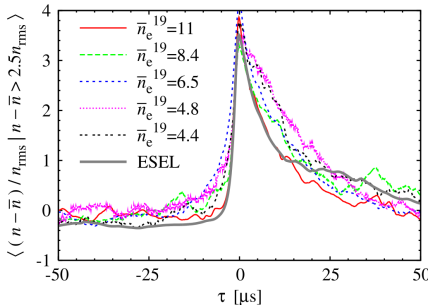


Figure 1.14: Conditionally averaged waveform of particle density time series from TCV and ESEL simulations. Reprinted from [9], with permission from IAEA.

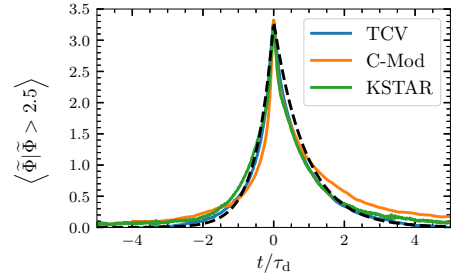


Figure 1.15: Conditionally averaged waveform for time series measured in the edge of TCV, Alcator C-Mod and KSTAR. The broken line shows a two-sided exponential fit. Image courtesy of A. Theodorsen [39].

cator C-Mod in 1998 [60]. Since then, plasma filaments have been observed in over 40 devices, including all major tokamak experiments, with a variety of diagnostics [61]. Filaments typically have a significantly higher density than the surrounding plasma and are aligned to the local magnetic field with their scale lengths much larger in the direction parallel to the magnetic field compared to the perpendicular direction. Filaments have a cross-field size between 2 mm and 10 cm, radial velocity of 0.2 to 2 km/s and a lifetime in the range of tens of  $\mu\text{s}$  [62–70]. Examples of plasma filaments for different confinement modes in the MAST device are shown in Fig. 1.16. The elongation of the filaments along the magnetic field, stretching from the upper to the lower divertor is clearly visible. Filaments propagate through the SOL due to interchange motion, illustrated in Fig. 1.17. A simplified model ignoring parallel dynamics explains filament motion as follows: Due to the magnetic geometry at the outboard mid-plane, magnetic gradient and curvature drifts result in a charge polarization, perpendicular to the magnetic field  $\mathbf{B}$ . This results in an electric field  $\mathbf{E}$ , transporting the filament in the radial direction with the  $\mathbf{E} \times \mathbf{B}$  velocity  $\mathbf{u}_E$ . While the filaments propagate outwards they carry particles and heat much faster than purely diffusive transport would allow, explaining the broad profiles in the SOL. Fig. 1.18 shows an example of a filament propagating through the SOL of NSTX. Here, the filament is visualized in the plane perpendicular to the field lines. Due to their appearance in the two-dimensional plane, filaments are often referred to as blobs in this context.

Measurements using Langmuir probes and GPI simultaneously confirmed that propagating filaments are the same structures that cause intermittent

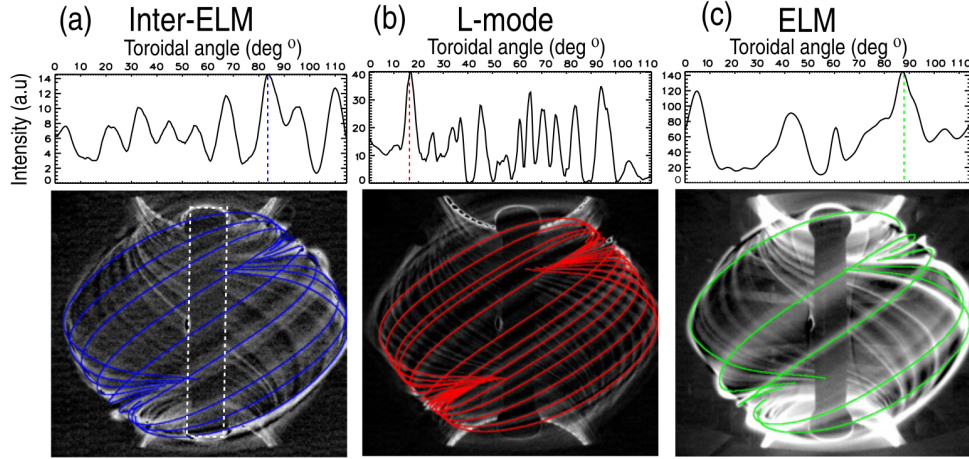


Figure 1.16: Wide angle fast visible imaging of inter-ELM, L-mode and ELM filaments in the MAST device. The panels above show the toroidal variation in emission across the center column, the peaks are used to label the filaments. Reprinted from [71], © IOP Publishing. Reproduced with permission. All rights reserved.

bursts in the time series [74, 75]. The intermittency of the time series and the length and amplitude of individual bursts are therefore given by the filament parameters.

Even though radial blob propagation can be qualitatively understood with the presented two-dimensional model, parallel dynamics must be considered for a more accurate picture [7]. Since the filament plasma is neutral, the current due to magnetic gradient and curvature drifts must be closed. The charged particles stream along the magnetic field lines until they reach the target plates where the resulting parallel current can close in the plasma Debye sheath. The parallel resistivity of the plasma and the sheath resistivity limits the magnitude of the parallel current. Alternatively, the current can be closed by polarization currents in the cross-field plane, thereby creating the dipolar electric potential. A schematic illustration of the current paths are shown in Fig. 1.19. The ratio of the current closed through the parallel and perpendicular path determines the strength of the electric field in the filament and therefore its  $\mathbf{E} \times \mathbf{B}$  velocity. If the parallel currents are dominant and close mainly in the plasma sheath the filament is said to be in the “sheath limited” regime, while in the case where the currents are closed in the cross-field plane, the filament is in the “inertial” regime. Analytical velocity scaling laws show that the radial velocity of a filament  $v_{\perp}$  is strongly dependent on its perpendicular size  $a$  of a filament

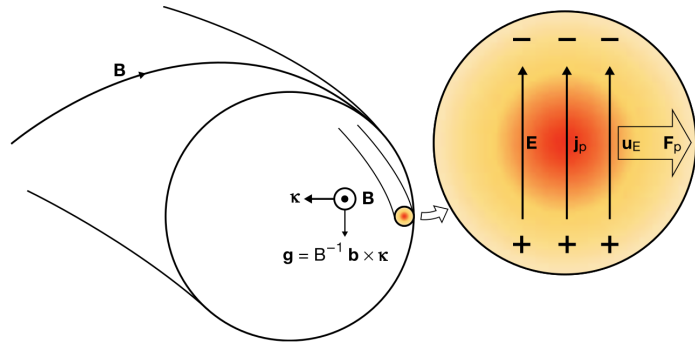


Figure 1.17: Illustration of charge separation in the filament and the resulting  $\mathbf{E} \times \mathbf{B}$  drift, transporting the filament in the radial direction. Reprinted from [72], with the permission from AIP Publishing.

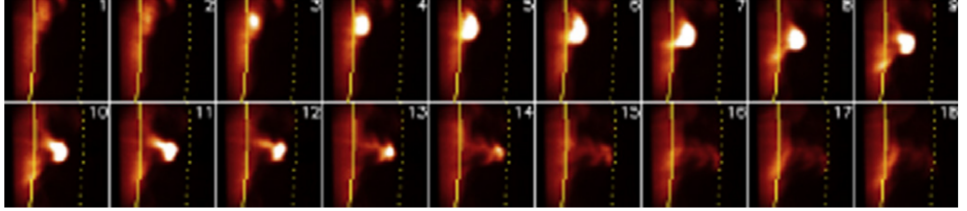


Figure 1.18: Propagation of a blob from the main plasma through the SOL in the NSTX device. Each box shows a  $24 \times 24$  cm portion of the edge at the outer mid-plane and the frame rate is  $7\mu\text{s}$ . The position of the separatrix is given by the full line and the the wall shadow by the broken line. Reprinted from [73], with the permission from Elsevier.

[76, 77], as

$$v_{\perp}(a) \propto \begin{cases} \sqrt{2a} & \text{for } a \gg a^* \\ 1/a^2 & \text{for } a \ll a^* \end{cases} \quad (1.5)$$

where  $a^*$  is defined as

$$a^* = \left( \frac{4L^2}{\rho_s R} \right)^{1/5} \rho_s. \quad (1.6)$$

In this expression  $L$  stands for the connection length to the divertor targets,  $R$  is the major radius of the tokamak and  $\rho_s$  the ratio between the acoustic speed and the ion gyration radius. These velocity scaling laws are reproduced with numerical simulations [78–80]. However, it is found difficult to match these laws to experimental observations in both asymptotic limits, as small

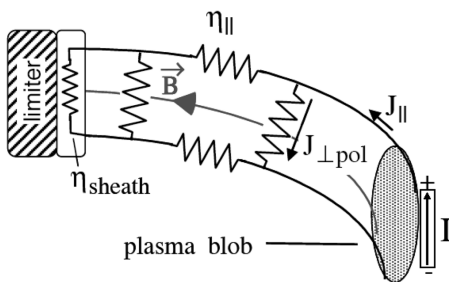


Figure 1.19: Schematic illustration of current paths within a filament. Reprinted from [7]. Copyright © Cambridge University Press 2008.

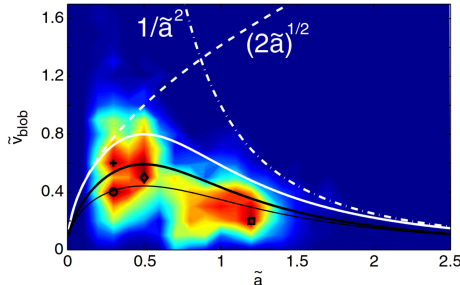


Figure 1.20: Joint probability of the normalized filament velocity and cross field size in the TORPEX device. Reprinted figure with permission from [76]. Copyright (2009) by the American Physical Society.

filaments are difficult to identify and filaments cannot become larger than the SOL width [65, 66]. Relatively good agreement has been found in the toroidal plasma device TORPEX shown in Fig. 1.20, showing the joint probability of the filament velocity and cross-field size [76]. Here, the perpendicular width of the filaments is normalized by  $a^*$  and the filament velocity by

$$v^* = \left( \frac{2L\rho_s^2}{R^3} \right)^{1/5} c_s \quad (1.7)$$

with  $c_s$  standing for the ion sound speed. The dashed and dotted lines show the ideal scaling laws for the inertial and sheath connected regimes. It is found that the cross-field size of filaments is in between the scale length of the plasma pressure gradient and the particle gyration radius, hence, filaments are often referred to as mesoscale structures.

Even though filament generation has been extensively studied in tokamak plasmas [81, 82], simple toroidal plasmas [83–86] and numerical simulations [87–90], to this day no quantitatively accurate analytical model of filament generation has been developed [61, 91, 92]. A number of linear instabilities have been identified that are attributed to cause filament generation, namely the interchange, drift-wave, Kelvin-Helmholtz, Rayleigh–Taylor, resistive-ballooning and conducting-wall instabilities [61, 93]. Due to the limited understanding of the intricate physics responsible for filament generation in tokamak plasmas, this topic remains a field of active research.

## 1.6 Numerical modeling of SOL plasmas

As experimental measurements and analytical models for SOL turbulence and plasma filaments face intrinsic limitations, numerical simulations of first principle based models have provided further insight. Due to the complexity of the involved physics, it remains a delicate task to derive models with appropriate approximations that still capture the most relevant physical mechanisms of SOL turbulence. Attempts to model the SOL with gyrokinetic particle-in-cell codes are limited by their enormous computational costs and their dependence on poorly understood boundary conditions [94, 95]. Electromagnetic gyrofluid models have been derived [96] and applied for studying temperature dynamics and finite Larmor radius effects on filaments [97, 98], as well as turbulence in open and closed magnetic field lines [99, 100]. At present, most numerical models for SOL turbulence and filament dynamics originate from the standard plasma fluid transport equations derived by Braginskii [101]. The derivations of the fluid models used in the papers and manuscripts included in this thesis are discussed in Chapter 2.

Numerical simulations of SOL plasmas can be categorized into models of saturated turbulence where filament-like structures are created due to non-linear dynamics, and simulations of explicitly seeded, isolated filaments. The first self-consistent evolution of a seeded plasma blob in two dimensions has been studied in 2003 [102], shown in Fig. 1.21. Here, the blob is initialized as a symmetrical 2D-Gaussian on a constant plasma background. The radial propagation and the evolution of the blob into a mushroom-shaped object with a steep front has been observed. The radial variation of the density of the blob and its according  $\mathbf{E} \times \mathbf{B}$  velocity is shown in Fig. 1.22. The peak of the radial velocity is trailing the density peak, resulting in a steepening of the blob front. The according temporal evolution is shown in Fig. 1.23, where the observed pulses have a short rise and long fall time; an observation consistent with the underlying pulses of time series in experiments such as in Fig. 1.9. Studies of isolated filaments have been extended to three dimensions, considering dynamics parallel to the magnetic field [103–108] and have been used to investigate specific physical effects such as electromagnetic effects or finite ion Larmor radius effects [103, 109–111]. Models for radial blob velocity dependencies on filament amplitudes and sizes have been developed [78, 80, 112, 113]. Simulations of multiple simultaneously seeded filaments discovered that filaments in close proximity interact through the electric potential they generate [114, 115]. A systematical analysis of blob interaction in dependence of the intermittency, defined as the level of blob overlap, is presented in Paper IV.

First attempts of modeling plasma turbulence typically use two-dimensional slab geometries, where curvature effects are modeled by effective gravity terms.

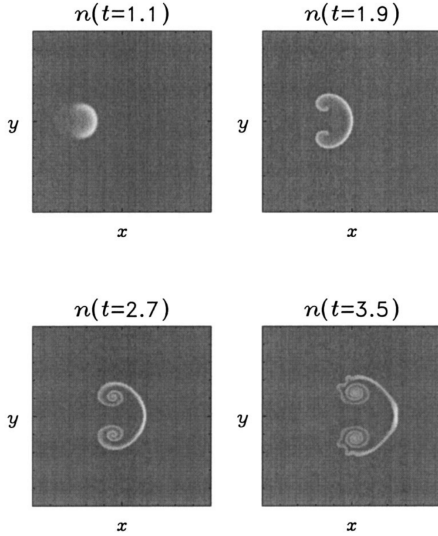


Figure 1.21: Contour plot of the evolution of a 2D density blob. Reprinted from [102], with the permission from AIP Publishing.

Rayleigh–Bénard convection models have been used as a simplified description of the non-linear interchange dynamics in the SOL [116–123]. These models have been further extended by including sheath dissipation due to losses along magnetic field lines and drift wave dynamics in the edge region [87, 124–133]. One example for a turbulence simulation in a 2D slab geometry of a model including sheath dissipation is presented in Fig. 1.24. Plasma streaming from the core into the SOL is modeled as a density source term in the left hand side of the simulation domain. Small perturbations in the plasma density become unstable and result in coherent structures that propagate radially outwards due to the interchange mechanism. The transition from closed to open magnetic field lines is simulated by applying different closures for the parallel dynamics. These 2D turbulence simulations have contributed to the understanding of the stability of filaments in the SOL and were able to reproduce the characteristic PDFs of plasma fluctuations and their radial variations [131, 134]. Further investigations on the statistical properties in turbulence simulations can be performed by analyzing time series [9, 123, 135–137] and blob tracking methods in order to investigate filament properties [138–141].

Advances in computing power enabled three-dimensional turbulence simulations in the last decade, taking into account the parallel dynamics in SOL plasmas [106, 142–147]. Three-dimensional simulations enable implementing realistic geometries and can therefore be used to explore X-point effects and dif-

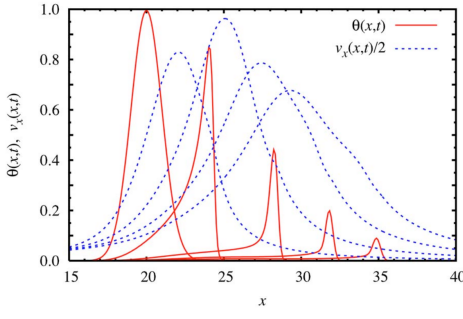


Figure 1.22: Radial variation of the plasma density (full line) and the radial velocity (broken line) at the symmetry axis of a seeded blob. Reprinted from [112], with the permission from AIP Publishing.

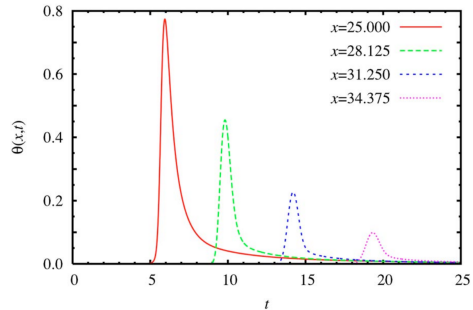


Figure 1.23: Temporal evolution of the plasma density recorded at the symmetry axis at different radial positions. Reprinted from [112], with the permission from AIP Publishing.

ferent divertor configurations [139, 148]. Due to their immense computational costs, three-dimensional turbulence simulations have relatively short runs, limiting the amount of statistical analysis that can be performed.

A variety of comparisons between the output from numerical simulation codes and experiments have been performed in order to validate simulation codes. These studies mainly focused on the dynamics of individual blob structures or on specific physical effects on turbulence and transport. Surprisingly little attention has been attributed to comparisons of fluctuation statistics, considering their universal nature in experiments. The published papers and yet unpublished manuscripts included in this thesis attempt to fill this gap. Here, the main focus lies on utilizing the FPP model, which predicts all major statistical properties of experimental measurements at the outboard mid-plane. By comparing time series from numerical simulations to the predictions of the FPP model one can identify which parameters and assumptions conform to experimental observations. We can thereby gain additional insight and a better understanding of the intricate physics of the boundary of present and future fusion devices.

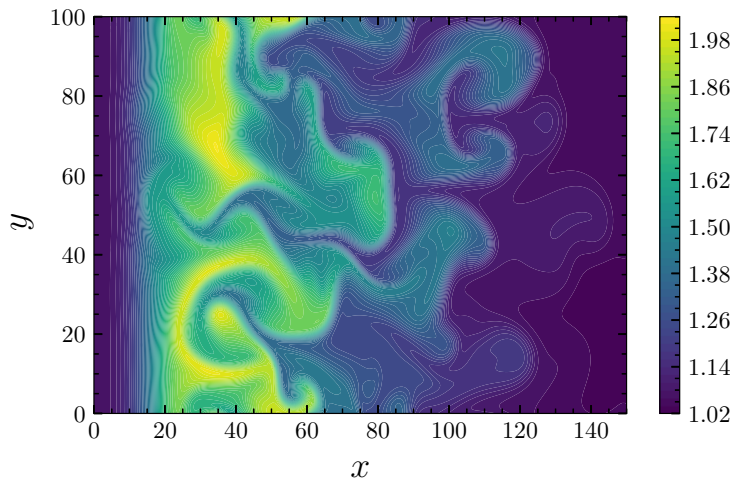


Figure 1.24: Snapshot of plasma density of a two-dimensional turbulence simulation. Plasma is injected into the simulations domain at a constant rate and generates blob-like structures due to turbulence. Reprinted from [141], with the permission from AIP Publishing.



# 2 | Reduced fluid models for SOL plasmas

In this chapter, a brief derivation of the reduced fluid models used in the included publications is presented. The derivations start from the Braginskii fluid equations whose assumptions and validity for SOL plasmas are discussed. Applying drift reduction, Bohm-normalization and a number of approximations, results in the reduced two-fluid model, equivalent to the two-dimensional fluid models used in Paper III and IV. By applying interchange normalization this model will be further modified to the idealized interchange model, used in Paper I.

## 2.1 Braginskii fluid equations

The Braginskii fluid model is derived by taking successive velocity moments of the kinetic Boltzmann equation and applying a collisional closure. Each moment depends on the next higher order and therefore require additional assumptions to obtain a closure for the model. The Braginskii equations describe the evolution of the three lowest order fluid moments. The assumptions and the formulation of this closure are presented in [101]. The standard Braginskii fluid equations describing the evolution of the particle density  $n_\alpha$ , fluid velocity  $\mathbf{u}_\alpha$  and temperature  $T_\alpha$  for particle species  $\alpha$  are given by

$$\frac{\partial n_\alpha}{\partial t} + \nabla \cdot (n_\alpha \mathbf{u}_\alpha) = 0, \quad (2.1)$$

$$m_\alpha n_\alpha \left( \frac{\partial}{\partial t} + \mathbf{u}_\alpha \cdot \nabla \right) \mathbf{u}_\alpha = -\nabla p_\alpha - \nabla \cdot \Pi_\alpha + Z_\alpha e n_\alpha (\mathbf{E} + \mathbf{u}_\alpha \times \mathbf{B}) + \mathbf{R}_\alpha, \quad (2.2)$$

$$\frac{3}{2} n_\alpha \left( \frac{\partial}{\partial t} + \mathbf{u}_\alpha \cdot \nabla \right) T_\alpha + p_\alpha \nabla \cdot \mathbf{u}_\alpha = -\nabla \cdot \mathbf{q}_\alpha - \Pi_\alpha : \nabla \mathbf{u}_\alpha + Q_\alpha. \quad (2.3)$$

Here,  $\alpha$  determines the particle species, i.e., electrons and ions,  $m$  the particle mass,  $p$  the pressure,  $Z_\alpha e$  the particle charge,  $\mathbf{R}$  the friction force,  $\Pi$

the viscous stress tensor,  $\mathbf{q}$  the heat flux, : the tensor inner product and  $Q$  the frictional interspecies heating and energy exchange.

The Braginskii equations are only applicable if certain assumptions for the modeled system are valid. Applying fluid equations requires that the distribution of particle velocities is close to Maxwellian, i.e., the time scale of relaxation back to a Maxwellian must be shorter than the characteristic time scales of the modeled system. If this condition is fulfilled, the system is referred to as collisional. In addition to being collisional, a plasma must be strongly magnetized to be adequately described by the Braginskii equations. This implies that the particles complete many gyrations between collisions, setting an upper limit for the collisionality of the plasma.

In summary, the phenomenon we want to model needs to satisfy the following conditions in order to be well described by the Braginskii equations:

$$L_{\perp} \gg \rho_{\alpha}, \quad (2.4)$$

$$L_{\parallel} \gg \lambda, \quad (2.5)$$

$$\tau \gg \tau_c \gg \Omega_{\alpha}^{-1}. \quad (2.6)$$

In these expressions  $L_{\perp}$  stands for the characteristic size of the modeled phenomena perpendicular to the magnetic field,  $\rho_{\alpha}$  is the gyration radius for species  $\alpha$ ,  $L_{\parallel}$  the parallel size of the system,  $\lambda$  the collisional mean free path,  $\tau$  the characteristic time of the problem,  $\tau_c$  the collision time and  $\Omega_{\alpha}$  the gyration frequency of the referred particle species [149].

For the further derivation using drift reduction it will be useful to quantify the magnetization. We thereby define the magnetization parameter  $\delta$  as

$$\delta = \frac{\rho_{\alpha}}{L_{\perp}}. \quad (2.7)$$

The magnetization can be equivalently expressed in the temporal domain by

$$\delta = \frac{\nu_{ie}}{\Omega_i} \quad (2.8)$$

where  $\nu_{ie}$  stands for the collisional frequency between ions and electrons.

For both electrons and ions the magnetization parameter is  $\delta \ll 1$  for a fully magnetized plasma.

## 2.2 Drift reduction

The Braginskii model given by Eqs. (2.1) - (2.3) is very general, making modeling of SOL plasmas with the presented equations relatively inefficient. A

more suitable description of plasma phenomena in the SOL can be derived by simplifying the presented model with an approach called drift ordering. Since turbulence and filaments in the SOL evolve with velocities much lower than the plasma sound speed  $c_s = \sqrt{(T_e + T_i)/m_i}$  we apply the ordering

$$\mathbf{u}_\perp \sim \frac{\rho_\alpha}{L_\perp} c_s \sim \delta c_s. \quad (2.9)$$

This ordering assumes that the transverse electric fields are small, resulting in the perpendicular electric field being substantially electrostatic. This is a direct consequence of the  $\mathbf{E} \times \mathbf{B}$  velocity being a factor  $\delta$  smaller than sound speed and Faraday's law [149]. We can now determine the perpendicular part of the momentum equation, given by Eq. (2.2), by taking the cross product with  $\mathbf{B}$  resulting in

$$\mathbf{u}_{\alpha,\perp} = \frac{\mathbf{E} \times \mathbf{B}}{B^2} - \frac{\nabla p_\alpha \times \mathbf{B}}{e_\alpha n_\alpha B^2} - \frac{m_\alpha d\mathbf{u}_\alpha/dt \times \mathbf{B}}{e_\alpha B^2} - \frac{\nabla \cdot \Pi_\alpha \times \mathbf{B}}{e_\alpha n_\alpha B^2} + \frac{\mathbf{R}_\alpha \times \mathbf{B}}{e_\alpha n_\alpha B^2}, \quad (2.10)$$

where we used  $d/dt = \partial/\partial t + (\mathbf{u}_\alpha \cdot \nabla)$  and assumed single charge particle species, i.e.,  $Z_\alpha e = e_\alpha$ . The terms in this expression display the fluid drifts occurring in the system, namely from left to right: the  $\mathbf{E} \times \mathbf{B}$  drift; the diamagnetic drift; the polarization drift; the viscous drift and the collisional drift. From this expression we can determine the dominant drifts and thereby simplify the model.

As mentioned previously, the electric drift velocity is of  $\mathcal{O}(\delta)$  compared to the plasma sound speed:

$$\mathbf{u}_E = \frac{\mathbf{E} \times \mathbf{B}}{B^2} \sim \delta c_s. \quad (2.11)$$

Similarly, the diamagnetic drift is also of  $\mathcal{O}(\delta)$  since

$$\mathbf{u}_{\text{dia}} = -\frac{\nabla p_\alpha \times \mathbf{B}}{e_\alpha n_\alpha B^2} \sim \frac{n_\alpha T_\alpha B}{L_\perp e_\alpha n_\alpha B^2} \sim \frac{T_\alpha}{L_\perp \Omega_\alpha m_\alpha} \sim \delta c_s. \quad (2.12)$$

The polarization drifts for both ions and electrons are smaller in comparison, as can be shown by

$$\mathbf{u}_{\text{pol},i} = \frac{m_i d\mathbf{u}_i/dt \times \mathbf{B}}{e_i B^2} \sim \delta^3 c_s, \quad (2.13)$$

and

$$\mathbf{u}_{\text{pol},e} \sim \frac{m_e}{m_i} \delta^3 c_s. \quad (2.14)$$

For the viscous drift we use Bragniskii's approximation for the perpendicular component of the viscous stress tensor  $\Pi_\alpha \sim (p_\alpha/\Omega_\alpha)\nabla v_\alpha$  which shows that this term is of  $\mathcal{O}(\delta^3)$  since

$$\mathbf{u}_{\text{vis},i} = \frac{\nabla \cdot \Pi_\alpha \times \mathbf{B}}{e_\alpha n_\alpha B^2} \sim \frac{nT\delta c_s}{e_i n_i B L_\perp^2 \Omega} \sim \delta^3 c_s, \quad (2.15)$$

and

$$\mathbf{u}_{\text{vis},e} \sim \frac{m_e}{m_i} \delta^3 c_s, \quad (2.16)$$

respectively. Lastly, we need to find an approximation for the collisional drift. For this we use  $\mathbf{R}_\perp = en\mathbf{J}_\perp/\sigma_\perp$  for the perpendicular momentum transfer from electron-ion friction and  $\sigma_\perp = ne^2\nu_{ei}/m_e$ . From the ordering follows  $\mathbf{J}_\perp \sim en\delta c_s$  which leads to the approximation of the frictional drift

$$\mathbf{u}_{\text{fri}} = \frac{\mathbf{R}_\alpha \times \mathbf{B}}{e_\alpha n_\alpha B^2} \sim \frac{ne\delta c_s}{B\sigma_\perp} \sim \frac{m_e}{m_i} \frac{\nu_{ei}}{\Omega} \delta c_s. \quad (2.17)$$

For SOL conditions we can typically assume that  $\nu_{ei}/\Omega \sim \delta$  so that the collisional drift is of  $\mathcal{O}(\delta^2)$ .

This ordering reveals that the dominant perpendicular drifts are the electric and the diamagnetic drifts as all other drifts are at least one order of magnitude smaller. By substituting the remaining drifts into the Braginskii equation we can rewrite the electron density equation in a simpler form,

$$\frac{\partial n_e}{\partial t} + \nabla \cdot [n_e (\mathbf{u}_E + \mathbf{u}_{\text{dia},e} + \mathbf{u}_{e\parallel})] = 0. \quad (2.18)$$

Since the plasma is quasi-neutral, i.e.  $n_e \simeq n_i \simeq n$ , this equation is used to describe the evolution of the total plasma density  $n$ . Eq. (2.18) is usually manipulated to

$$\frac{\partial n}{\partial t} + \mathbf{u}_E \cdot \nabla n = -\nabla \cdot (n\mathbf{u}_{\parallel,e}) + \left( \frac{1}{e} \nabla p_e - n \nabla \phi \right) \cdot \nabla \times \left( \frac{\mathbf{b}}{B} \right). \quad (2.19)$$

Instead of explicitly deriving separate continuity equations for electrons and ions, we can utilize quasi-neutrality and charge conservation to derive an equation for the fluid velocity, which will prove to be very handy. For this we use  $\nabla \cdot \mathbf{J} = 0$  with  $\mathbf{J} = en(\mathbf{u}_i - \mathbf{u}_e)$ . Inserting all drifts that give rise to a net current results in

$$\nabla \cdot (\mathbf{J}_{\text{dia}} + \mathbf{J}_{\text{pol}} + \mathbf{J}_{\text{vis}} + \mathbf{J}_\parallel) = 0. \quad (2.20)$$

In the following we only include the leading order drifts in the ion polarization velocity and neglect the electron polarization drift entirely due to the small electron mass. The sum of the ion polarization and viscous drifts using the

lowest order solution of the perpendicular momentum equation and the parallel velocity  $\mathbf{u}_0 = \mathbf{u}_{0\perp} + \mathbf{u}_{i\parallel}$  is then given by

$$\mathbf{u}_{\text{pol},i} + \mathbf{u}_{\text{vis},i} = \mathbf{b} \times \frac{1}{enB} \left[ m_i n \left( \frac{\partial}{\partial t} + \mathbf{u}_{i0} \cdot \nabla \right) \mathbf{u}_{i0} + \nabla \cdot \Pi_{i0} \right], \quad (2.21)$$

where  $\Pi_{i0}$  is the viscous stress tensor calculated with  $\mathbf{u}_{i0}$  and

$$\mathbf{u}_{0\perp} = \mathbf{b} \times \frac{1}{B} \left( \nabla \phi + \frac{1}{en} \nabla p_i \right). \quad (2.22)$$

Inserting this into Eq. (2.20) leads to the drift-reduced charge conservation equation [149]

$$\begin{aligned} -\nabla \cdot \left\{ \mathbf{b} \times \frac{1}{B} \left[ m_i n \left( \frac{\partial}{\partial t} + \mathbf{u}_{i0} \cdot \nabla \right) \mathbf{u}_{i0} + \nabla \cdot \Pi_{i0} \right] \right\} = \\ \nabla \cdot \mathbf{J}_{\parallel} + \nabla (p_i + p_e) \cdot \nabla \times \left( \frac{\mathbf{b}}{B} \right), \end{aligned} \quad (2.23)$$

which will be further simplified in the following.

## 2.3 Further approximations and simplifications

A number of additional approximations are applied to simplify the model and make it efficiently numerically solvable.

First of all, we apply the electrostatic approximation, and thereby neglect all time derivatives of  $\mathbf{B}$  and calculate the electric field  $\mathbf{E}$  directly from the electric potential. Under this approximation, Eq. (2.23) can be expressed in the more readable form

$$\begin{aligned} m_i \nabla \cdot \left[ \frac{n}{B} \frac{d_0}{dt} \left( \frac{\nabla_{\perp} \phi}{B} + \frac{\nabla_{\perp} p_i}{enB} \right) \right] - \nabla \cdot (\mathbf{b} \times \nabla \cdot \Pi_0) = \\ \nabla \cdot \mathbf{J}_{\parallel} + \nabla (p_i + p_e) \cdot \nabla \times \left( \frac{\mathbf{b}}{B} \right), \end{aligned} \quad (2.24)$$

where we used  $d_0/dt = \partial/\partial t + (\mathbf{u}_{i0} \cdot \nabla)$ . In addition, we neglected spatial non-uniformity of  $\mathbf{B}$ , which will be discussed in further detail later. Studies of electromagnetic effects on plasma blob-filament transport showed that these effects in high temperature or high beta plasmas suppress the resistive drift wave turbulence in filaments [109, 150] but will not be considered in the following.

We can further simplify Eq. (2.24) by applying scale separation for the plasma density, so that  $\nabla n \sim \nabla n_0 + \nabla \tilde{n} \sim 1/L_n + k\tilde{n}$ , where the particle density

has been separated into a background  $n_0$  and a fluctuation  $\tilde{n}$ .  $L_n$  stands for the characteristic scale length for the background density and  $k$  for the wave number for the particle density fluctuations. Dividing by  $n_0$  leads to  $\nabla \ln n \sim 1/L_n + k\tilde{n}/n_0$ . We now assume that  $1/kL_n \ll 1$  and  $\tilde{n}/n_0 \ll 1$ . The latter assumption is the so called thin layer or Boussinesq approximation where we assume that the density perturbations are small compared to the equilibrium. This assumption is hardly justified since relative fluctuations in the SOL can be of order unity as discussed in the previous chapter. This approximation is, however, commonly used since it makes the numerical integration of Eq. (2.24) significantly more efficient. By introducing a generalized vorticity,

$$\varpi = \nabla \cdot \left( \nabla_{\perp} \phi + \frac{\nabla_{\perp} p_i}{en} \right), \quad (2.25)$$

we can now simplify the first term in Eq. (2.24) to

$$m_i \nabla \cdot \left[ \frac{n}{B} \frac{d_0}{dt} \left( \frac{\nabla_{\perp} \phi}{B} + \frac{\nabla_{\perp} p_i}{enB} \right) \right] \approx \frac{m_i n}{B^2} \frac{d_0 \varpi}{dt}. \quad (2.26)$$

From this expression,  $\varpi$  can be relatively easily inverted, especially when assuming that ions are cold, leading us to the next approximation.

For the remaining derivation we will assume small ion temperature,  $T_i \ll T_e$ , simplifying the equations significantly. This is a restrictive assumption, as experimental measurements indicate that the ion temperature is higher than the electron temperature in the SOL [151, 152]. Numerical simulations incorporating finite ion temperature have shown that the coherency of filaments is increased [153]. However, since the simplified model still captures the fundamental dynamics in the SOL, this approximation is commonly used to reduce the model complexity.

As for the electrons, all models in the included publications and manuscripts assume isothermal electrons. This assumption simplifies the model drastically, as it makes Eq. (2.3) obsolete. Numerical simulations of isolated filaments with dynamic electron temperature have shown that thermal effects lead to a strong increase in the filament propagation in the poloidal direction and reduce the net radial propagation. These effects arise from the electron temperature dependence of the sheath currents, which will be discussed later in this chapter [154].

Next, we will define the geometry of the magnetic field. For the whole simulation domain, we assume straight magnetic field lines with constant field strength. We need to make one exception to this assumption, as no curvature term would remain in a completely homogeneous field. As there would be no drive for filament motion without this term, it is required to capture some

effects of curvature in the model. With the use of vector algebra presented in [149] we can write the curvature term from Eqs. (2.19) and (2.24) as

$$\nabla \times \left( \frac{\mathbf{b}}{B} \right) = 2 \frac{\mathbf{b} \times \boldsymbol{\kappa}}{B} + \frac{\mu_0 (\mathbf{J}_{\parallel} - \mathbf{J}_{\perp})}{B^2}, \quad (2.27)$$

where we introduced the curvature vector  $\boldsymbol{\kappa} = (\mathbf{b} \cdot \nabla) \mathbf{b}$ . Note that one unit of the term  $\mathbf{b} \times \boldsymbol{\kappa}/B$  originates from the magnetic gradient and one from the curvature. The second term on the right hand side can be neglected due to charge conservation [149]. The magnetic field in a tokamak can be approximated to lowest order to be purely toroidal and falling radially with  $1/R$ . In a cylindrical coordinate system  $(R, \Phi, Z)$  the toroidal magnetic field is therefore

$$\mathbf{B} = \frac{B_0 R_0}{R} \hat{\Phi}. \quad (2.28)$$

In a slab geometry with  $Z$  being replaced with the binormal direction  $y$  which is perpendicular to  $\hat{\mathbf{R}}$  and  $\hat{\Phi}$  this motivates the definition of the curvature operator

$$\mathcal{K}(u) = \nabla \times \left( \frac{\mathbf{b}}{B} \right) \cdot \nabla u \approx -\frac{2}{B_0 R_0} \frac{\partial u}{\partial y}. \quad (2.29)$$

Despite arguing that the frictional drift is negligible in Eq. (2.30) one typically retains an approximation of this term due to numerical reasons. We therefore add this term to Eq. (2.19) as

$$\nabla \cdot (n_e \mathbf{u}_{\text{fri}}) \approx -\nabla \cdot (D_n \nabla_{\perp} n_e) \approx -D_n \nabla_{\perp}^2 n_e, \quad (2.30)$$

where we introduced the density diffusion coefficient  $D_n$  which we assumed to be spatially constant. Similarly, one can derive the diffusion term for Eq. (2.24) from its ion viscosity term, since we can use the approximation

$$\nabla \cdot \Pi_i = -m_i n \mu_{\omega} \nabla_{\perp}^2 \mathbf{u}_E, \quad (2.31)$$

where  $\mu_{\omega}$  stands for the effective cross-field kinematic viscosity of the ions. Inserting the electric drift and taking the divergence results in the diffusion term for  $\nabla_{\perp}^2 \phi$  as

$$\nabla \cdot \left( \frac{m_i \mu_{\omega}}{e B^2} \nabla_{\perp} \nabla_{\perp}^2 \phi \right). \quad (2.32)$$

The diffusion coefficients can be approximated from classical or neo-classical diffusion such as presented in [155], or are chosen for numerical accuracy and stability.

Arguably the starker simplification of the presented models in this thesis is the restriction to only two dimensions, the plane perpendicular to  $\mathbf{B}$ . The

parallel closure of the model equations is different for closed and open field lines, i.e., whether the simulation domain is located in the SOL or in the edge region. Since the parallel direction plays an important role in the SOL for particle and current dissipation as plasma flows along the magnetic field lines towards the divertor plates, a suitable approximation for the parallel losses is required. This closure is achieved by integrating over the parallel direction where the so-called sheath boundary conditions come into play. In the initial transient period where the plasma vessel is filled and the cold wall surface electrically neutral, electrons will strike the surface at a higher rate than the ions due to their higher speed. This charges the vessel walls negatively which impedes further electron flow towards the surface and results in a thin sheath at material surfaces. Here, the ions shield the electric potential of the surface and the sheath extends a few Debye lengths,  $\lambda_D = \sqrt{\epsilon_0 T_e / n_e e^2}$ , outwards from the surface into the plasma. In this region quasi neutrality is violated since the ion density is higher than the electron density,  $n_i > n_e$ . The electric current density drawn by the vessel walls is governed by the influx of electrons and ions at the sheath surface. It depends on the potential  $\phi$  at the sheath entrance and can be written as

$$\mathbf{J}_{\parallel}|_{\text{sheath}} = en_{se}c_s \left[ 1 - e^{\Lambda - e\phi/T_e} \right], \quad (2.33)$$

with the plasma density at the sheath edge  $n_{se}$ , the acoustic speed  $c_s$  and the floating potential  $\Lambda = \ln \sqrt{m_i/2\pi m_e}$ . The first term in the parenthesis is due to the ion flux and the second due to the electron flux [17]. We can now take the average of the parallel dimension in a slab geometry with  $\mathbf{B} = B\hat{\mathbf{z}}$ ,

$$\frac{1}{L_{\parallel}} \int_{-L_{\parallel}/2}^{L_{\parallel}/2} \nabla_{\parallel} \cdot \mathbf{J}_{\parallel} dz, \quad (2.34)$$

and use Eq. (2.33) as the boundary conditions. The first term on the right hand side of Eq. (2.19) can be handled analogously for the parallel electron velocity.

Paper III includes a core region in the simulation domain, requiring a different closure for the parallel dynamics. In this model we include resistivity in the parallel component of the electron momentum equation neglecting inertia, i.e.,

$$en \frac{\partial \phi}{\partial z} - T_e \frac{\partial n}{\partial z} + \chi en J_{\parallel} = 0, \quad (2.35)$$

where the resistivity is given by  $\chi = m\nu_{ei}/n_e e^2$ . Rearranging Eq. (2.35) for  $J_{\parallel}$  and taking the parallel derivative results in [156, 157]

$$\nabla_{\parallel} \cdot \mathbf{J}_{\parallel} = \frac{T_e}{e\chi} \frac{\partial^2}{\partial z^2} \left( \ln n_e - \frac{e\phi}{T_e} \right). \quad (2.36)$$

From this we can take the average of the parallel dimension by integrating over  $z$ , resulting in the desired 2D model equations. A systematic analysis of the dimensionality of scrape-off layer turbulence is presented in [147, 158].

## 2.4 Reduced two-fluid model

Since the Braginskii fluid model is only valid in a specific range of time and length scales it seems natural to normalize all physical variables to values that are characteristic for the modeled system. We will first discuss the so-called Bohm normalization where we normalize the spatial and temporal units by  $\rho_s$  and  $\Omega_i$ , respectively, i.e.,

$$\nabla \rightarrow \nabla' = \rho_s \nabla, \quad \frac{\partial}{\partial t} \rightarrow \frac{\partial}{\partial t'} = \frac{1}{\Omega_i} \frac{\partial}{\partial t}. \quad (2.37)$$

Here,  $\rho_s$  stands for the ion sound Larmor radius defined as  $\rho_s = \sqrt{T_e m_i}/eB$ . We normalize the remaining variables with their characteristic values for SOL conditions  $N$  and  $T_0$  as

$$n \rightarrow n' = \frac{n}{N}, \quad T_e \rightarrow T' = \frac{T_e}{T_0}, \quad \phi \rightarrow \phi' = \frac{e\phi}{T_0}. \quad (2.38)$$

From these expressions we can define the characteristic magnitude for the density source, diffusion coefficients and effective gravity drive as

$$S \rightarrow S' = SN\Omega_i, \quad D_n \rightarrow D'_n = D_{\text{Bohm}}D_n, \quad \mu_\omega \rightarrow D'_\Omega = D_{\text{Bohm}}\mu_\omega, \quad g = \frac{2\rho_s}{R}, \quad (2.39)$$

where the collisional diffusion is defines as  $D_{\text{Bohm}} = \rho_s^2\Omega_i$ . Applying this normalization to Eq. (2.19) and dropping the dash sign, inserting the curvature operator from Eq. (2.29) and adding the diffusion term of Eq. (2.30) results in the electron density equation

$$\frac{dn}{dt} + g \left( \frac{\partial n}{\partial y} - n \frac{\partial \phi}{\partial y} \right) = D_n \nabla_\perp^2 n + S_n + \left\langle \nabla_\parallel (nu_{e\parallel}) \right\rangle_\parallel, \quad (2.40)$$

where the advective derivative is given by  $d/dt = \partial/\partial t + \mathbf{u}_E \cdot \nabla_\perp$  and  $\mathbf{u}_E = -\nabla_\perp \phi \times \mathbf{B}/B^2$  is the  $\mathbf{E} \times \mathbf{B}$  drift. Here,  $\langle \cdot \rangle_\parallel$  refers to the average over the parallel dimension. We also added the density source term  $S_n$ . Performing the same kind of operations on Eq. (2.24) after applying the Boussinesq approximation results in the vorticity equation

$$\frac{d\nabla_\perp^2 \phi}{dt} + \frac{g}{n} \frac{\partial n}{\partial y} = D_\Omega \nabla_\perp^4 \phi + \left\langle \frac{1}{n} \nabla_\parallel J_\parallel \right\rangle_\parallel, \quad (2.41)$$

where we introduced  $D_\Omega$  as the collisional dissipation term representing viscosity. Averaging over the parallel direction after inserting Eq. (2.34) and Eq. (2.36) can be expressed as

$$\left\langle \nabla_{\parallel} (n u_{e\parallel}) \right\rangle_{\parallel} = -\eta(x)n \exp(\Lambda - \phi) + \chi(x)(\hat{\phi} - \hat{n}), \quad (2.42a)$$

$$\left\langle \frac{1}{n} \nabla_{\parallel} J_{\parallel} \right\rangle_{\parallel} = \eta(x) [1 - \exp(\Lambda - \phi)] + \chi(x)(\hat{\phi} - \hat{n}), \quad (2.42b)$$

where the spatially fluctuating electron density  $\hat{n}$  and plasma potential  $\hat{\phi}$  are defined as  $\hat{n} = n - \langle n \rangle_y$  and  $\hat{\phi} = \phi - \langle \phi \rangle_y$  and  $\langle \cdot \rangle_y$  refers to the flux surface average. Note, that we neglect  $1/n$  in the plasma conductivity term for the vorticity equation, since we assume the plasma density to have small relative fluctuation levels in the edge region and  $n \sim 1$ . We redefined  $\chi = (\rho_s/L_{\parallel})^2 (m_i/m_e)(\Omega_s/\nu_{ei})$  as the normalized parallel plasma conductivity where we used  $\nabla_{\parallel}^2 \rightarrow -k_{\parallel}^2 \simeq -L_{\parallel}^{-2}$  and introduced  $\eta = \rho_s/L_{\parallel}$  as the normalized sheath dissipation coefficient.  $\nu_{ei}$  stands for the collision frequency between electrons and ions given by

$$\nu_{ei} = \frac{\log \Lambda_c e^4 Z^2 n_i}{6\sqrt{2}\pi^{3/2} \epsilon_0^2 \sqrt{m_e T_e^{3/2}}}, \quad (2.43)$$

and the Coulomb logarithm is approximately [149]

$$\log \Lambda_c \approx 18 - \log \left[ \left( \frac{n_e}{10^{19}} \right)^{1/2} \left( \frac{T_e}{10^3 e} \right)^{-3/2} \right]. \quad (2.44)$$

These parameters depend on the radial position, the sheath dissipation term only occurs in the SOL and the plasma conductivity term is finite in the plasma edge region. A schematic illustration of these two regions in the simulation domain is shown in Fig. 2.1.

This model is equivalent to the one used in Paper III. Paper IV utilizes a slightly simpler model placing the whole domain in the SOL by choosing  $\eta = \text{constant}$  and  $\chi = 0$ , and discarding  $\Lambda$  in the sheath dissipation term. A list of representative machine parameters relevant for the reduced two-fluid models is presented in Table 2.1. Since each device performs a range of experiments with slightly different configurations, these parameters might vary. The presented parameters are consistent with those used in the numerical simulations in the included references. The radial position of the SOL is indicated by the sum of the major and minor radius and the parallel connection length is estimated as

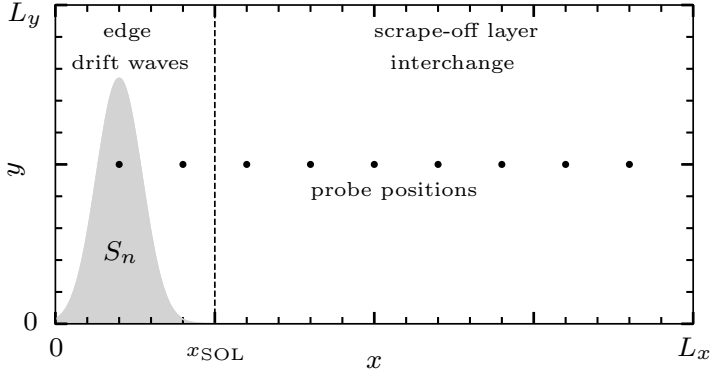


Figure 2.1: Schematic illustration of the edge and scrape-off layer region in the simulation domain. The position of the plasma source term (gray shaded) and the border between edge and SOL (dashed vertical line) are indicated [137].

$L_{\parallel} = \pi q_{95} R$ , with  $q_{95}$  as the safety factor at the 95% poloidal magnetic flux surface, if not explicitly stated in the references. It should also be noted, that the definition of the connection length varies from source to source as it may refer to the whole poloidal length or only to the length between the outboard midplane to the outer divertor plates.

Table 2.1: Machine parameters.

	$n_e [\text{m}^{-3}]$	$T_e [\text{eV}]$	$B [\text{T}]$	$L_{\parallel} [\text{m}]$	$R + r [\text{m}]$	reference
MAST	$8 \times 10^{18}$	40	0.5	30	1.5	[106]
C-Mod	$1.4 \times 10^{19}$	23	4.5	20	0.9	[159]
TCV	$5 \times 10^{18}$	25	1.45	15	1.13	[138, 160]
KSTAR	$7 \times 10^{17}$	35	2.0	26	2.3	[161]
AUG	$8 \times 10^{18}$	40	2.5	25	2.15	[162]
JET	$2 \times 10^{19}$	45	3.45	25	4.21	[155]
NSTX	$6 \times 10^{18}$	13	0.25	20	1.53	[159]

The plasma parameters calculated for these device parameters are presented in Table 2.2. Based on these values, we can estimate the input parameters for the reduced two-fluid model shown in Table 2.3. Note that the diffusion and viscosity coefficients for the model are not presented as they are chosen arbitrarily high for numerical stability in the included publications.

Table 2.2: Physical parameters.

	$\rho_s[\text{m}]$	$\Omega_i[\text{s}^{-1}]$	$c_s[\text{ms}^{-1}]$
MAST	$1.8 \times 10^{-3}$	$2.4 \times 10^7$	$4.4 \times 10^4$
C-Mod	$1.5 \times 10^{-4}$	$2.2 \times 10^8$	$3.3 \times 10^4$
TCV	$5.0 \times 10^{-4}$	$6.9 \times 10^7$	$3.5 \times 10^4$
KSTAR	$4.3 \times 10^{-4}$	$9.6 \times 10^7$	$4.1 \times 10^4$
AUG	$3.7 \times 10^{-4}$	$1.2 \times 10^8$	$4.4 \times 10^4$
JET	$2.8 \times 10^{-4}$	$1.7 \times 10^8$	$4.6 \times 10^4$
NSTX	$2.1 \times 10^{-3}$	$1.2 \times 10^7$	$2.5 \times 10^4$

Table 2.3: Input parameters.

	$g$	$\eta$	$\chi$
MAST	$2.4 \times 10^{-3}$	$6.1 \times 10^{-5}$	$2.7 \times 10^{-4}$
C-Mod	$3.4 \times 10^{-4}$	$7.7 \times 10^{-6}$	$1.0 \times 10^{-5}$
TCV	$8.8 \times 10^{-4}$	$3.3 \times 10^{-5}$	$1.9 \times 10^{-4}$
KSTAR	$3.7 \times 10^{-4}$	$1.6 \times 10^{-5}$	$6.8 \times 10^{-4}$
AUG	$3.4 \times 10^{-4}$	$1.5 \times 10^{-5}$	$7.7 \times 10^{-5}$
JET	$1.3 \times 10^{-4}$	$1.1 \times 10^{-5}$	$3.1 \times 10^{-5}$
NSTX	$2.7 \times 10^{-3}$	$1.0 \times 10^{-4}$	$1.1 \times 10^{-4}$

## 2.5 Idealized interchange model

A minimal model for SOL plasma dynamics in the cross-field plane can be obtained by ignoring parallel dynamics entirely and applying the so called interchange normalization. We start again with Eq. (2.19) and Eq. (2.24), use the curvature operator given by Eq. (2.29), and include the diffusion terms. The perpendicular components then take the form

$$\left( \frac{\partial}{\partial t} + \frac{1}{B} \hat{\mathbf{z}} \times \nabla \phi \cdot \nabla \right) n - \frac{2n}{B_0 R_0} \frac{\partial \phi}{\partial y} + \frac{2T_e}{e B_0 R_0} \frac{\partial n}{\partial y} = D_n \nabla_{\perp}^2 n, \quad (2.45a)$$

$$\left( \frac{\partial}{\partial t} + \frac{1}{B} \hat{\mathbf{z}} \times \nabla \phi \cdot \nabla \right) \nabla_{\perp}^2 \phi + \frac{2c_s^2}{R_0 n} \frac{\partial n}{\partial y} = D_{\Omega} \nabla_{\perp}^4 \phi. \quad (2.45b)$$

Under the interchange normalization, length scales are normalized by the characteristic length  $l$  of the system, time scales by the ideal interchange rate  $\gamma = \sqrt{g/l}$  with  $g = 2c_s^2/R_0$  and the plasma density and electrostatic potential

accordingly, i.e.,

$$\nabla \rightarrow \nabla' = l\nabla, \quad \frac{\partial}{\partial t} \rightarrow \frac{\partial}{\partial t'} = \frac{1}{\gamma} \frac{\partial}{\partial t}, \quad n \rightarrow n' = \frac{n}{N}, \quad \phi \rightarrow \phi' = \frac{\phi}{\gamma B_0 l^2}. \quad (2.46)$$

Inserting these expressions into the equations for plasma density and vorticity results in

$$\left( \frac{\partial}{\partial t'} + \hat{\mathbf{z}} \times \nabla' \phi' \cdot \nabla' \right) n' - 2n' \frac{l}{R_0} \frac{\partial \phi'}{\partial y'} + \frac{\gamma}{\Omega_i} \frac{\partial n'}{\partial y'} = \frac{D_n}{\gamma l^2} \nabla'^2_{\perp} n', \quad (2.47a)$$

$$\left( \frac{\partial}{\partial t'} + \hat{\mathbf{z}} \times \nabla' \phi' \cdot \nabla' \right) \nabla'^2_{\perp} \phi' + \frac{1}{n'} \frac{\partial n'}{\partial y'} = \frac{D_{\Omega}}{\gamma l^2} \nabla'^4_{\perp} \phi'. \quad (2.47b)$$

We neglect the term resulting from the compression of the electric drift since its prefactor is  $l/R_0 \ll 1$ . The term resulting from the compression of the diamagnetic drift will also be neglected in the continuity equation as previous work has shown that it has a negligible contribution to the cross-field dynamics and since  $\gamma/\Omega_i \ll 1$  [163]. In addition we introduce the normalized particle diffusion and viscosity coefficients

$$\kappa = D_n/\gamma l^2 \text{ and } \mu = D_{\phi}/\gamma l^2, \quad (2.48)$$

neglect  $1/n$  in front of the interchange term as we apply the Boussinesq approximation and drop the dash notation to receive the minimal model for plasma convection

$$\left( \frac{\partial}{\partial t} + \hat{\mathbf{z}} \times \nabla \phi \cdot \nabla \right) n = \kappa \nabla^2_{\perp} n, \quad (2.49a)$$

$$\left( \frac{\partial}{\partial t} + \hat{\mathbf{z}} \times \nabla \phi \cdot \nabla \right) \nabla^2_{\perp} \phi + \frac{\partial n}{\partial y} = \mu \nabla^4_{\perp} \phi. \quad (2.49b)$$

The emphasis of this model lies on reducing the complexity and the number of free parameters as drastically as possible without losing the capability of modeling plasma advection self-consistently. This model has also been used in the past to describe buoyancy-driven convection in a fluid confined between two horizontal plates and heated from below. The model, named the Rayleigh-Bénard convection model after the original experimental work of Henri Bénard [164] and the first analytical work on this model of Lord Rayleigh [165], has become a paradigm to investigate nonlinear phenomena due to its rich dynamics [123, 166–170]. The normalized particle diffusion and viscosity coefficients in the presented formulation are related to the Rayleigh and Prandtl numbers as  $R = 1/\kappa\mu$  and  $R = \mu/\kappa$ , which are typically used as model parameters for the Rayleigh-Bénard model. We use this model in Paper I.



# 3 | Stochastic modeling

This chapter is dedicated to describing the Filtered Poisson Process (FPP), a stochastic model used for describing the intermittent fluctuations in single point measurements obtained in the boundary of fusion experiments. The basis of this model was already developed in 1909 [171] and was further extended in the 1940s to describe noise in vacuum tubes [172, 173]. Since then, the model has been extended and used to describe fluctuations in numerous academic fields, including neuroscience, fluid dynamics and nuclear fission [174–180]. The FPP has first been introduced as a model describing SOL fluctuations in 2012 [30] and has since then shown excellent agreement with the statistical properties of fluctuations in various fusion experiments [31–38].

## 3.1 Filtered Poisson Process

The FPP is a stochastic process, given by a superposition of uncorrelated pulses which are distributed according to a Poisson process. For a given time  $t \in [0, T]$  the process  $\Phi_k(t)$  can be written as [30, 49]

$$\Phi_k(t) = \sum_{k=1}^{K(T)} A_k \phi\left(\frac{t - t_k}{\tau_d}\right). \quad (3.1)$$

Here, the random variables are defined as follows:  $K(T)$  stands for the number of pulses arriving in the time interval  $[0, T]$ ,  $A_k$  is the pulse amplitude and  $t_k$  the pulse arrival time. It is further assumed that all pulses have the same pulse shape  $\phi$  and duration time  $\tau_d$ .

Alternatively, the process can be expressed as a convolution of the pulse shape and a delta pulse train

$$\Phi_k(t) = [\phi * f_K]\left(\frac{t}{\tau_d}\right), \quad (3.2)$$

where  $f_K$  is the forcing defined as a train of delta pulses

$$f_K(\theta) = \sum_{k=1}^{K(T)} A_k \delta \left( \theta - \frac{t_k}{\tau_d} \right). \quad (3.3)$$

As the process can be expressed as a train of delta pulses filtered through the pulse shape, it is called a *Filtered Poisson Process*.

For a given time interval  $[0, T]$ , the number of pulses  $K(T)$  follows a Poisson distribution

$$P_K(K|T) = \frac{1}{K!} \left( \frac{T}{\tau_w} \right)^K \exp \left( -\frac{T}{\tau_w} \right), \quad (3.4)$$

with intensity  $T/\tau_w$ . The waiting times between two consecutive pulses are independent and exponentially distributed with mean value  $\tau_w$  and the arrival times  $t_k$  are independent and uniformly distributed in the interval  $[0, T]$ . These properties of the process are consistent with experimental measurements, showing exponentially distributed waiting times [33, 35–37]. Time series with quasi-periodic arrival times are observed in SOL simulations utilizing Rayleigh–Bénard like convection models [123] and are discussed in Paper II in further detail. The amplitudes are chosen to be exponentially distributed, as this is observed in experimental measurements [35–37].

In the following, we will discuss two pulse shapes that are most relevant for SOL fluctuation measurements and corresponding numerical simulations. Firstly, the pulse shape of an asymmetric, two-sided exponential pulse is defined as

$$\phi(\theta, \lambda) = \begin{cases} \exp \left( -\frac{\theta}{1-\lambda} \right), & \theta \geq 0, \\ \exp \left( \frac{\theta}{\lambda} \right), & \theta < 0. \end{cases} \quad (3.5)$$

Here,  $\theta$  is a dimensionless variable and  $\lambda$  stands for the asymmetry parameter with  $\lambda \in (0, 1)$ . In some cases, a one-sided exponential pulse is applied with  $\lambda = 0$ , which refers to the limit  $\lim_{\lambda \rightarrow 0} \phi(\theta, \lambda)$ . Exponential pulses stand in good agreement with experimental measurements [9, 31, 33, 35–37, 42, 44, 53] and numerical SOL simulations [9, 137]. Secondly, Lorentzian pulses are considered which are defined as

$$\psi(\theta) = \frac{1}{\pi} \frac{1}{1 + \theta^2}. \quad (3.6)$$

These can also be generalized to a skewed Lorentzian, however no closed analytical form is known and require a definition via the inverse Fourier transform [181]. Indications for Lorentzian pulses in time series in the edge region [182–185] and corresponding numerical simulations [123] have been reported. Exponential pulses consist of a discontinuous peak and exponential tails, whereas

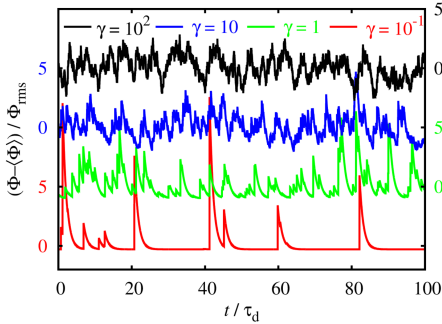


Figure 3.1: Realizations of the FPP with one-sided exponential pulses and different intermittency parameters. Reprinted from [49], with the permission from AIP Publishing.

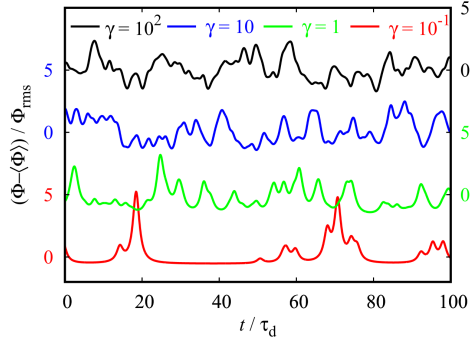


Figure 3.2: Realizations of the FPP with Lorentzian pulses and different intermittency parameters. Reprinted from [186], with the permission from AIP Publishing.

Lorentzian pulses have a smooth peak and algebraic tails. The consequences of these properties will be apparent in the following discussions.

Calculating moments of distributions of the process requires the integrals of the pulse shapes, defined as

$$I_n = \int_{-\infty}^{\infty} d\theta [\phi(\theta)]^n. \quad (3.7)$$

For exponential pulses this results in  $I_{\phi,n} = 1/n$ , independent of the pulse asymmetry  $\lambda$ . For Lorentzian pulses the first four integrals are given by  $I_{\psi,1} = 1$ ,  $I_{\psi,2} = 1/2\pi$ ,  $I_{\psi,3} = 3/8\pi^2$  and  $I_{\psi,4} = 5/16\pi^3$ .

The main property of the FPP is given by the ratio of the pulse duration and average waiting time,

$$\gamma = \frac{\tau_d}{\tau_w}, \quad (3.8)$$

which is referred to as the intermittency parameter. For short waiting times and long duration times,  $\gamma \gg 1$ , the level of pulse overlap is high, resulting in a large mean value and small relative variation around the mean. In the opposite limit,  $\gamma \ll 1$ , the signal is dominated by individual, isolated pulses, resulting in a small mean value and large relative fluctuations. Numerical realizations of the FPP with different intermittency parameters are shown for one-sided exponential pulses in Fig. 3.1 and for symmetric Lorentzian pulses in Fig. 3.2 displaying the features of these processes.

## 3.2 Moments and PDFs

The four lowest order central moments of the FPP take the form

$$\langle \Phi \rangle = \gamma \langle A \rangle I_1, \quad (3.9a)$$

$$\Phi_{\text{rms}}^2 = \gamma \langle A^2 \rangle I_2, \quad (3.9b)$$

$$S_\Phi = \frac{1}{\gamma^{1/2}} \frac{\langle A^3 \rangle I_3}{\langle A^2 \rangle^{3/2} I_2^{3/2}}, \quad (3.9c)$$

$$F_\Phi = 3 + \frac{1}{\gamma} \frac{\langle A^4 \rangle I_4}{\langle A^2 \rangle^2 I_2^2}, \quad (3.9d)$$

where  $S_\Phi$  stands for the skewness of the process and  $F_\Phi$  is the kurtosis or flatness [30]. The last two moments exhibit the parabolic relationship

$$F_\Phi = 3 + \frac{\langle A^2 \rangle \langle A^4 \rangle}{\langle A^3 \rangle^2} \frac{I_2 I_4}{I_3^2} S_\Phi^2. \quad (3.10)$$

Inserting the expressions for the integrals of the pulse shapes for two-sided exponential and Lorentzian pulses and assuming exponentially distributed amplitudes simplifies these expressions further. For exponential pulses the expression for the relative fluctuation level becomes

$$\frac{\Phi_{\text{rms}}}{\langle \Phi \rangle} = \gamma^{-1/2}, \quad (3.11)$$

and the universal parabolic relationship of Eq. (3.10) reduces to

$$F_\Phi = 3 + \frac{3}{2} S_\Phi^2, \quad (3.12)$$

which stands in good agreement with experimental measurements [46–48]. Notably, these expressions do not depend on the pulse asymmetry parameter,  $\lambda$ .

The PDF of the process with exponential pulses is given by a Gamma distribution with shape parameter  $\gamma$  and scale parameter  $\langle A \rangle$  [187],

$$P_{\Phi,\phi}(\Phi) = \frac{\Phi^{\gamma-1}}{\langle A \rangle^\gamma \Gamma(\gamma)} \exp\left(-\frac{\Phi}{\langle A \rangle}\right). \quad (3.13)$$

Typically, the realization of the process is normalized to have zero mean and unit standard deviation,

$$\tilde{\Phi} = \frac{\Phi - \langle \Phi \rangle}{\Phi_{\text{rms}}}, \quad (3.14)$$

with the according PDF [187],

$$P_{\tilde{\Phi},\phi}(\tilde{\Phi}) = \frac{\gamma^{\gamma/2}}{\Gamma(\gamma)} \left( \tilde{\Phi} + \gamma^{1/2} \right)^{\gamma-1} \exp\left(-\gamma^{1/2} \tilde{\Phi} - \gamma\right). \quad (3.15)$$

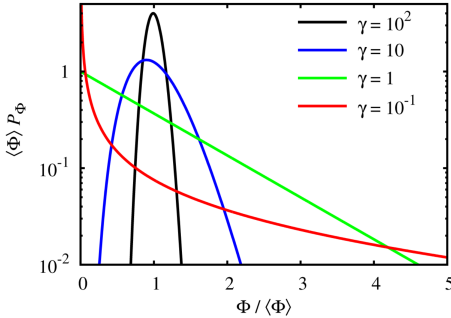


Figure 3.3: PDFs of a FPP with exponential pulses with different intermittency parameters  $\gamma$ . Reprinted from [49], with the permission from AIP Publishing.

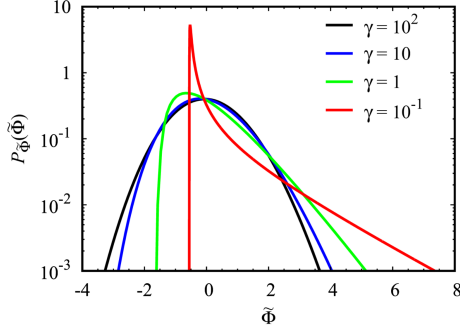


Figure 3.4: PDFs of a normalized FPP with Lorentzian pulses with different intermittency parameters  $\gamma$ . Reprinted from [188], with the permission from AIP Publishing.

This expression is used as a fit in Fig. 1.11. For an FPP of Lorentzian pulses no closed expressions for its PDF is known. However, it can be derived by taking the inverse Fourier transform of its corresponding characteristic function resulting in [188]

$$P_{\tilde{\Phi},\psi}(\tilde{\Phi}) = \left(\frac{\pi}{\gamma}\right)^{1/2} \int_0^\infty dw \exp\left(-\frac{\gamma\pi w \sin(1/2 \arctan w)}{(1+w^2)^{1/4}}\right) \times \cos\left(\pi\gamma w + \sqrt{\pi\gamma}\tilde{\Phi}w - \frac{\gamma\pi w \cos(1/2 \arctan w)}{(1+w^2)^{1/4}}\right). \quad (3.16)$$

For both exponential and Lorentzian pulses the PDF of the processes are characterized by the intermittency parameter. The PDFs are shown for a range of different  $\gamma$  in Fig. 3.3 and Fig. 3.4. The PDFs are unimodal for all values of  $\gamma$  and have an exponential tail towards large fluctuation amplitudes for small values of  $\gamma$ . In the opposite limit, the PDFs approach a normal distribution with vanishing mean and unit standard deviation for  $\tilde{\Phi}$ .

### 3.3 Second order statistics

In order to calculate the second order moments, namely the power spectral density (PSD) and the Auto-correlation function (ACF), we consider the FPP as a convolution of a pulse train  $f_K$  and a pulse shape  $\phi$ . The Fourier transform of the FPP is given by the product of the Fourier transform of  $f_K$  and  $\phi$ . The power spectrum of  $\Phi$  can therefore be expressed as the product of the power

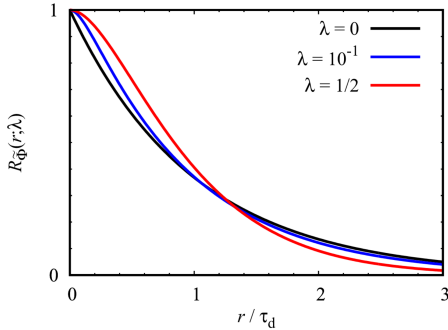


Figure 3.5: Auto-correlation function of a normalized FPP consisting of two-sided exponential pulses with different asymmetry parameters  $\lambda$ . Reprinted from [52], with the permission from AIP Publishing.

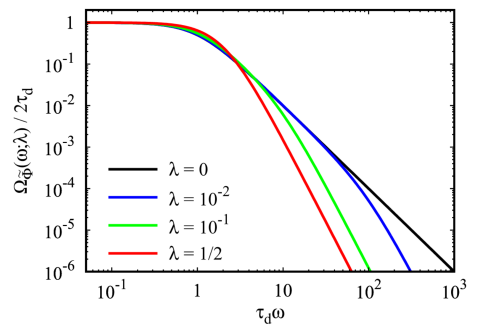


Figure 3.6: Power spectral density of a normalized FPP consisting of two-sided exponential pulses with different asymmetry parameters  $\lambda$ . Reprinted from [52], with the permission from AIP Publishing.

spectrum of  $f_K$  and  $\phi$ . The power spectrum of  $f_K$  is flat due to the uncorrelated delta pulses, so that the frequency dependence of the spectrum of  $\Phi$  is only dependent on  $\phi$ . The ACF is given by the Fourier transform of the PSD. For two-sided exponential pulses the PSD of an FPP normalized according to Eq. (3.14), takes the form [52]

$$\Omega_{\tilde{\Phi},\phi}(\omega; \lambda) = \frac{2\tau_d}{[1 + (1 - \lambda)^2\tau_d^2\omega^2][1 + \lambda^2\tau_d^2\omega^2]}, \quad (3.17)$$

with the according ACF

$$R_{\tilde{\Phi},\phi}(r; \lambda) = \frac{1}{1 - 2\lambda} \left[ (1 - \lambda) \exp \left( -\frac{|r|}{(1 - \lambda)\tau_d} \right) - \lambda \exp \left( -\frac{|r|}{\lambda\tau_d} \right) \right]. \quad (3.18)$$

The ACF and PSD are displayed for a range of  $\gamma$ -values in Figs. 3.5 and 3.6. In contrast to the PDFs, the second order statistics are independent of  $\gamma$  but change for different  $\lambda$ . In the limits of a one-sided exponential pulse, the ACF is purely exponential and the PSD is Lorentzian shaped. For  $\lambda$  close to zero or 1, the spectrum has an intermediate range where the spectrum falls with  $\omega^{-2}$  before it falls with  $\omega^{-4}$  in the high frequency limit. This expression is in excellent agreement with the experimental measurements shown in Fig. 1.13 with  $\lambda = 0.1$ .

For Lorentzian pulses the PSD of a normalized FPP takes an exponential form [181]

$$\Omega_{\tilde{\Phi},\psi}(\omega) = 2\pi\tau_d \exp(-2\tau_d|\omega|), \quad (3.19)$$

and the ACF is Lorentzian shaped,

$$R_{\tilde{\Phi},\psi}(r) = \frac{4}{4 + (r/\tau_d)^2}. \quad (3.20)$$

These expressions can be generalized to skewed Lorentzian pulses, however no closed expressions are known. An alternative formulation is presented in [181].

### 3.4 Excess time statistics

Expressions for excess time statistics, specifically the rate of level crossings above a given threshold and the average time spent above this threshold, can be derived for an FPP. In the context of fluctuations in the SOL of fusion experiments, these quantities are crucial considering the energy of incoming particles to the vessel walls and the energy threshold of physical sputtering. The number of sputtered particles per incoming particle is specified by the modified Bohdansky yield function [189]. The mean yield as a function of energy of an incoming deuterium particle on a tungsten wall is plotted for a range of relative fluctuation levels in Fig. 3.7. For constant energy, no sputtering occurs beneath 200 eV. For realistic scenarios of  $E_{\text{rms}}/\langle E \rangle > 0$  sputtering already occurs at significantly lower mean energies. An accurate description of excess time statistics is therefore of importance for fusion experiments.

For an FPP the number of level crossings is given by Rice's formula [173]

$$X(\Phi) = T \int_0^\infty d\dot{\Phi} \dot{\Phi} P_{\Phi,\dot{\Phi}}(\Phi, \dot{\Phi}). \quad (3.21)$$

Here  $\dot{\Phi}$  stands for the derivative of the process  $\Phi$  and  $P_{\Phi,\dot{\Phi}}(\Phi, \dot{\Phi})$  for the joint PDF between  $\Phi$  and  $\dot{\Phi}$ . This formulation requires the process to be differentiable, hence an FPP consisting of one-sided exponential pulses cannot be considered this way. For two-sided exponential pulses with  $\lambda \in (0, 1)$  the rate of up-crossings is given by [190]

$$\frac{\tau_d}{T} X(\Phi) = \frac{\lambda^{\gamma\lambda-1} (1-\lambda)^{\gamma(1-\lambda)-1}}{\gamma \Gamma(\gamma\lambda) \Gamma(\gamma(1-\lambda))} \left( \frac{\gamma\Phi}{\langle \Phi \rangle} \right)^\gamma \exp \left( -\frac{\gamma\Phi}{\langle \Phi \rangle} \right). \quad (3.22)$$

For this expression, the limit  $\lambda \rightarrow 0$  exists. Eq. (3.22) is plotted for exponential pulses with  $\lambda = 0$  and  $\lambda = 1/2$  and a range of  $\gamma$ -values in Fig. 3.8. From this, the PDF of time as well as mass above a given threshold can be determined analytically for the limits  $\gamma \rightarrow 0$  and  $\gamma \rightarrow \infty$  and numerically with Monte Carlo simulations for general  $\gamma$  [190].

At the time of writing this thesis, excess time statistics of an FPP consisting of Lorentzian pulses have not been investigated.

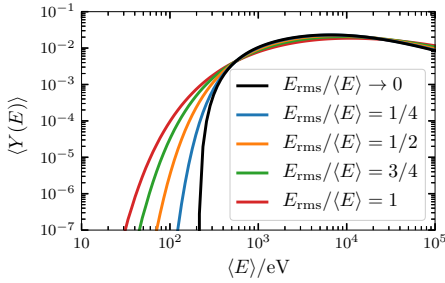


Figure 3.7: Mean yield function for a range of relative fluctuation levels. Image courtesy of A. Theodorsen [39].

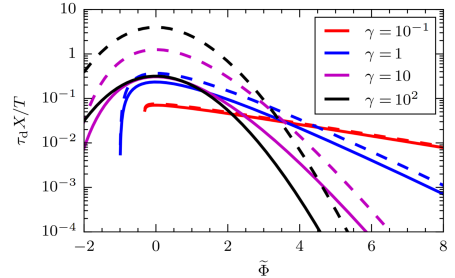


Figure 3.8: Rate of up-crossings for a FPP consisting of exponential pulses with  $\lambda = 0$  (dashed line) and  $\lambda = 1/2$  (full line) for various  $\gamma$ -values. Reprinted figure with permission from [190]. Copyright (2018) by the American Physical Society.

### 3.5 Density profiles

The FPP can be extended to include a spatial variable  $x$ , resulting in a model of advecting single pulses and corresponding profiles. In the following, this model is discussed in the context of filament motion in SOL plasmas. The presented notation is consistent with [49]. Alternative formulations based on a Lagrangian approach to filament dynamics result in equivalent expressions [11, 191–193].

The model is given by a superposition of pulses

$$\Phi_K(x, t) = \sum_{k=1}^K \phi_k(x, t). \quad (3.23)$$

In contrast to previous sections  $\phi_k$  is compounded by both amplitude and pulse shape. For simplicity, we keep  $K$  constant in the following derivation. The evolution of individual pulses, neglecting pulse interaction, is given by the modified advection equation,

$$\frac{\partial \phi_k}{\partial t} + v_\perp \frac{\partial \phi_k}{\partial x} + \frac{\phi_k}{\tau_\parallel} = 0, \quad (3.24)$$

with  $v_\perp$  as the radial velocity and  $\tau_\parallel$  representing the parallel transit time, describing parallel losses along the magnetic field. Note, that we assume  $v_\perp$  and  $\tau_\parallel$  to be constant for all filaments. Following Eq. (3.24), individual pulses can be written as the product of their amplitude and pulse shape,  $\phi_k(x, t) =$

$A_k(t)\varphi_k(x - x_k - v_k t)$  with  $x_k$  as the position of the pulse at  $t = 0$ . The individual amplitudes are assumed to satisfy the expression

$$\frac{dA_k}{dt} = -\frac{A_k}{\tau_{\parallel}}. \quad (3.25)$$

The solution for this amplitude equation can be expressed by introducing the initial amplitude  $A_{0k}$  resulting in

$$A_k(t) = A_{0k} \exp\left(-\frac{t + x_k/v_{\perp}}{\tau_{\parallel}}\right), \quad (3.26)$$

with the pulse  $k$  being located at  $x = 0$  at time  $-x_k/v_{\perp}$ . We further assume the pulse shape to take the form of an exponential function,

$$\varphi_k(x) = \Theta\left(-\frac{x}{l_{\perp}}\right) \exp\left(\frac{x}{l_{\perp}}\right), \quad (3.27)$$

where  $\Theta$  is the Heaviside function and  $l_{\perp}$  is the radial size of the pulse. Note, that this pulse shape is consistent with the findings shown in Fig. 1.22. We now consider the signal at a reference position  $\xi$ . At the reference time  $t_k = (\xi - x_k)/v_{\perp}$  for pulse  $k$  at position  $\xi$ , the process takes the form

$$\Phi_K(\xi, t) = \sum_{k=1}^K A_{0k} \exp\left(-\frac{\xi}{v_{\perp}\tau_{\parallel}}\right) \Theta\left(\frac{t - t_k}{\tau_{\perp}}\right) \exp\left(-\frac{t - t_k}{\tau_d}\right), \quad (3.28)$$

with  $\tau_{\perp} = l_{\perp}/v_{\perp}$  and the pulse duration given by the harmonic mean of the perpendicular and parallel transit time  $\tau_d = \tau_{\parallel}\tau_{\perp}/(\tau_{\parallel} + \tau_{\perp})$ . By averaging over uniformly distributed pulse arrivals, the resulting radial profile takes the exponential form

$$\langle \Phi \rangle(\xi) = \frac{\tau_d}{\tau_w} \langle A_0 \rangle \exp\left(-\frac{\xi}{v_{\perp}\tau_{\parallel}}\right). \quad (3.29)$$

The resulting scale length of the profile is governed by the radial velocity of the filaments and the parallel transit time. Multiple realizations at individual points in time and the corresponding mean profile are shown in Fig. 3.9.

The application of this model exhibits numerous limitations. The assumption of constant radial velocities and pulse size is an overly simplified description for filament transport in the SOL. In addition, the assumption of radially constant  $\tau_w$  and therefore radially constant  $\gamma$  does not hold in experimental observations. Interactions between individual filaments and two-dimensional motion are also not considered. However, this mathematical model still provides valuable insight in the relation between individual filaments and radial profiles in the SOL and can serve as a framework to relate isolated blob and filament studies to turbulence simulations and experimental measurements.

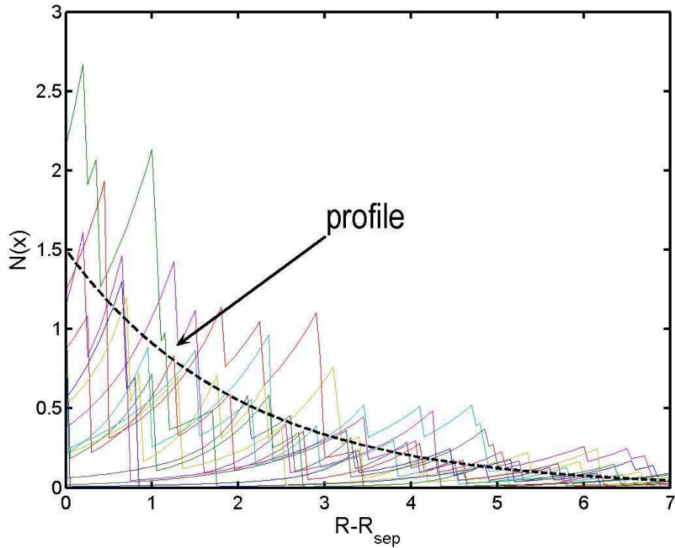


Figure 3.9: Radial exponential density profile (black dashed line) illustrated as the mean of individual density realizations (colored lines) given by a superposition of individual exponentially shaped pulses. Image courtesy of F. Militello [194].

### 3.6 Deconvolution method

Since the FPP can be expressed as a convolution of a pulse function  $\phi$  and a forcing, consisting of delta-function pulses  $f_K$ , shown in Eq. (3.2), one can attempt to estimate the forcing if the pulse shape is known [38, 123, 195]. For a given forcing, one can determine the pulse amplitudes  $\{A_k\}_{k=1}^K$  and arrival times  $\{t_k\}_{k=1}^K$  directly. This method has the advantage of capturing pulses of all sizes, not only events above a certain threshold as is the case for conditional averaging. Additionally, the problem of pulse overlap is less severe. In order to estimate the forcing, a modified Richardson-Lucy deconvolution algorithm can be used [196, 197]. The algorithm is initialized with a first guess for the forcing  $f_K^{(1)}$ . This value is iteratively updated with the  $n$ -th iteration given by

$$f_K^{(n+1)} = f_K^{(n)} \frac{D * \hat{\phi}}{f_K^{(n)} * \phi * \hat{\phi}}. \quad (3.30)$$

Here,  $\hat{\phi}(t) = \phi(-t)$  and  $D$  denotes the investigated time series. This algorithm converges to the least squares solution [198]. The initial guess for the forcing matters little as it only determines the number of iterations required until the algorithm converges.

This deconvolution algorithm thereby provides a versatile tool to analyze time series of SOL fluctuations in experiments and simulations, as it can provide clear results even for relatively short time series.



## 4 | Summary of Papers

The main focus of this thesis is on investigating the statistical properties of fluctuations in numerical simulations of SOL plasmas. Papers I and III study time series of single point measurements of established fluid models utilizing the FPP framework. Paper II provides additional theoretical insight to the results obtained in Paper I. Lastly, Paper IV investigates the interaction of filaments in SOL simulations and thereby discusses to what degree filaments can be considered uncorrelated, which is a basic assumption for the FPP model. The papers are ordered thematically.

In order to investigate the statistical properties of fluctuations described by different SOL models, we start with the idealized interchange model discussed in Paper I, arguably the simplest self-consistent description of SOL turbulence. Fluctuation time series at different radial positions are obtained and analyzed by stochastic modeling. We observe that the PDFs for the temperature fluctuations change from a normal distribution in the center of the simulation domain to a distribution with an exponential tail at the boundary of the simulation domain, a result consistent with experimental measurements of SOL plasmas. The PSDs have an exponential shape, which can be attributed to the underlying Lorentzian pulses, identified by a deconvolution method. The time series of the temperature show periods of strongly intermittent fluctuations with large bursts, interrupted by quiescent periods with quasi-periodic oscillations. These alternating periods can be attributed to the generation of a sheared mean flow through the fluid layer resulting in predator-prey-like dynamics of the kinetic energy integrals. Since this behavior has not been observed in time series of experimental measurements, it becomes clear that the utilized Rayleigh-Bénard-like model is insufficient to reproduce all statistical properties of SOL fluctuations.

Paper II provides additional theoretical insight as the shot noise process with periodic arrivals is investigated. It is shown analytically that the PSD of a shot noise process with periodic arrivals, Lorentzian pulses and exponentially distributed amplitudes has an exponentially modulated Dirac comb of

decaying amplitudes. In addition, we provide numerical realizations of a shot noise process with quasi-periodic arrival times by using a narrow, uniform distribution for each arrival around the strictly periodic arrival time. We find that moderate deviations from perfect periodicity destroys the Dirac comb as it leads to a broadening of its peaks and the decrease of the peak amplitudes for higher harmonics. The resulting PSD resembles the findings of Paper I, thereby confirming that the statistical properties of the fluctuation time series of the idealized interchange model are due to the presence of quasi-periodic Lorentzian pulses.

In Paper III we study the statistical properties of reduced two-fluid models and thereby increase the model complexity and number of considered physical effects compared to the idealized interchange equations. Again, we observe that the PDFs of fluctuation time series of the plasma density show an exponential tail in the far SOL. In contrast to the model discussed in Paper I, we find that the average burst or pulse shape is well described by a two-sided exponential function. The PSD of the particle density is that of the average pulse shape and does not change with radial position. The amplitudes and the waiting times between two consecutive arrivals are exponentially distributed. The profiles have an exponential form with radially constant scale length. As for the moments, we find that the fluctuation level increases with radial position and a nearly parabolic relationship between skewness and flatness moments. All of these results stand in perfect agreement with the predictions of the FPP model. In contrast to experimental measurements, we can choose an arbitrarily high sampling frequency for the single point measurements in these simulations. For frequencies higher than what is experimentally feasible, we observe an exponential spectrum in the PSD and a continuous, Lorenztian-like peak in the averaged pulse shape. These results cannot be compared directly to experimental counterparts due to the poor sampling rate by the diagnostics.

The last paper included in this thesis investigates the interaction of single filaments with each other and thereby addresses the question to what extent filaments can be considered isolated. As the FPP model assumes all pulses in a time series to be uncorrelated, this study remains highly relevant for the work presented in Papers I-III. A reduced two-fluid model is used for this investigation. In order to track filaments and determine filament parameters, a blob tracking algorithm based on an amplitude threshold method is presented. The velocity estimates of the algorithm are validated by a conventional center of mass approach. We introduce a model of multiple seeded filaments where the filament parameters, i.e. size, initial position, amplitude and arrival time, are sampled from appropriate distribution functions. A model-specific intermittency parameter is introduced which quantifies the level of filament interac-

tions as a function of their average size, velocity and waiting time. This model is then studied for different levels of complexity and filament interaction compared to theoretical size-velocity scaling laws of perfectly isolated filaments. We observe an increase in the average radial velocity for strongly interacting filaments. This is found to be caused by the interaction of filaments with the electrostatic potential of one another. The blob tracking approach is then applied on full plasma turbulence simulations where a strong correlation is found between filament amplitudes, sizes and velocities. Despite the observed increase in the radial velocities for strongly interacting filaments, we observe a systematical size-velocity relationship consistent with theoretical predictions. We therefore conclude that filaments can be regarded to lowest order as isolated structures, i.e., that the corresponding pulses in the FPP model can be assumed to be uncorrelated.



## 5 | Conclusion and future work

The exhaust of particles and heat in the boundary of contemporary magnetic confinement experiments remains to this day one of the biggest challenges on the road to commercially viable fusion energy production. Due to the complexity of the physics involved in the boundary of fusion devices, the scientific community relies increasingly on numerical simulations. This approach requires a validation metric for boundary turbulence simulations such as the Filtered Poisson Process (FPP), a model which is capable to predict all relevant statistical properties of fluctuations in the scrape-off layer (SOL). In this thesis, two models for boundary plasmas are analyzed in detail. The idealized interchange model, one of the simplest models used in the past, has shown to only reproduce some of the statistical properties observed in experimental measurements. The reduced two-fluid model has proven to reproduce all relevant properties of the FPP model and experimental measurements. These results are especially encouraging when considering the assumptions and simplifications of this model, such as the reduction to two dimensions, cold ions and isothermal electrons. In addition, this thesis provides a systematical study of plasma filament interaction, concluding that studies of isolated filaments adequately describe filament motion in turbulent SOL plasmas. This thesis thereby displays the relevance and importance of numerical simulations of reduced two-fluid models for gaining a better understanding of the intricate physics of boundary plasmas.

Based on the presented results, a number of ideas for future work can be proposed. One next step would be the analysis of three-dimensional turbulence simulations utilizing the FPP model, as the restriction to two dimensions remains arguably the strongest simplification of the presented simulations. Recent work studying the dimensionality of SOL turbulence utilizing the STORM code, the same code basis as used in Paper III and IV, provides a useful starting point for this investigation [147, 158]. The short time durations of 3D codes due to their computational costs remain a limitation for this project. However, this limitation could be compensated by placing several measurement probes

at different binormal/poloidal positions, where we expect the statistical properties of the fluctuation time series to be statistically identical. Including additional physical parameters such as evolving electron and ion temperature, using non-Boussinesq models or a more realistic magnetic geometry may also provide additional insight.

Hitherto, we have only considered models derived from the Braginskii fluid equations, leaving out codes utilizing different models that are commonly used for SOL plasmas. An obvious next candidate for stochastic validation would be fully self-consistent global gyrofluid models [96–98, 199, 200]. These models incorporate high fluctuation amplitude levels and finite Larmor radius effects and are considered to be a more complete description of the physical mechanisms in the SOL.

As for the reduced two-fluid model, a systematical parameter scan should be performed in order to identify the model variables relevant for the moments and fluctuation statistics. Unpublished work on this topic has found a non-trivial relationship between the sheath dissipation coefficient and the scale length of the radial profile. The blob tracking algorithm presented in Paper IV might provide further insight as the blob parameters could be compared to the FPP framework for density profiles discussed in chapter 3.5.

The role of neutral particles in the SOL has been studied in various turbulence codes [201–204]. To this day however, no attempt has been made to analyze the effects of local ionization and recombination on the fluctuation statistics. Applying the FPP framework on one of the existing models incorporating plasma-neutral interactions would be another interesting extension of the presented work.

Lastly, the stochastic model of multiple seeded filaments discussed in Paper IV opens the door to a number of applications. Since it enables to define all filament parameters it provides a perfect tool to bridge the gap between isolated filaments and turbulence simulations. One example would be the evaluation of the FPP framework for density profiles in a controlled environment if turbulence simulations prove to be too demanding.

# Bibliography

- [1] F. Romanelli, P. Barabaschi, D. Borba, G. Federici, L. Horton, R. Neu, D. Stork, and H. Zohm. *EU-EFDA report: Fusion Electricity - A roadmap to the realisation of fusion energy.* 2012.
- [2] J. P. Freidberg. *Plasma Physics and Fusion Energy.* Cambridge University Press, 2008.
- [3] “EUROfusion”. <https://www.euro-fusion.org>.
- [4] J. W. Connor, G. F. Counsell, S. K. Erents, S. J. Fielding, B. LaBombard, and K. Morel. Comparison of theoretical models for scrape-off layer widths with data from COMPASS-D, JET and Alcator C-Mod. *Nuclear Fusion*, 39:169, 1999.
- [5] D. Bohm. *The Characteristics of Electrical Discharges in Magnetic Fields.* New York: McGraw-Hill, 1949.
- [6] B. Lipschultz, B. LaBombard, C. S. Pitcher, and R. Boivin. Investigation of the origin of neutrals in the main chamber of Alcator C-Mod. *Plasma Physics and Controlled Fusion*, 44:733, 2002.
- [7] S. I. Krasheninnikov, D. A. D’ippolito, and J. R. Myra. Recent theoretical progress in understanding coherent structures in edge and SOL turbulence. *Journal of Plasma Physics*, 74:679, 2008.
- [8] J. Wesson and D. J. Campbell. *Tokamaks.* Oxford University Press, 2011.
- [9] O. E. Garcia, J. Horacek, R. A. Pitts, A. H. Nielsen, W. Fundamenski, V. Naulin, and J. Juul Rasmussen. Fluctuations and transport in the TCV scrape-off layer. *Nuclear Fusion*, 47:667, 2007.
- [10] B. LaBombard, R. L. Boivin, M. Greenwald, J. Hughes, B. Lipschultz, D. Mossessian, C. S. Pitcher, J. L. Terry, S. J. Zweben, and Alcator

- Group. Particle transport in the scrape-off layer and its relationship to discharge density limit in Alcator C-Mod. *Physics of Plasmas*, 8:2107, 2001.
- [11] F. Militello and J. T. Omotani. Scrape off layer profiles interpreted with filament dynamics. *Nuclear Fusion*, 56:104004, 2016.
  - [12] M. V. Umansky, S. I. Krasheninnikov, B. LaBombard, B. Lipschultz, and J. L. Terry. Modeling of particle and energy transport in the edge plasma of Alcator C-Mod. *Physics of Plasmas*, 6:2791, 1999.
  - [13] D. L. Rudakov, J. A. Boedo, R. A. Moyer, P. C. Stangeby, J. G. Watkins, D. G. Whyte, L. Zeng, N. H. Brooks, R. P. Doerner, T. E. Evans, M. E. Fenstermacher, M. Groth, E. M. Hollmann, S. I. Krasheninnikov, C. J. Lasnier, A. W. Leonard, M. A. Mahdavi, G. R. McKee, A. G. McLean, A. Y. Pigarov, W. R. Wampler, G. Wang, W. P. West, and C. P. C. Wong. Far SOL transport and main wall plasma interaction in DIII-D. *Nuclear Fusion*, 45:1589, 2005.
  - [14] F. Militello, P. Tamain, W. Fundamenski, A. Kirk, V. Naulin, A. H. Nielsen, and the MAST team. Experimental and numerical characterization of the turbulence in the scrape-off layer of MAST. *Plasma Physics and Controlled Fusion*, 55:025005, 2013.
  - [15] J. A. Boedo, J. R. Myra, S. Zweben, R. Maingi, R. J. Maqueda, V. A. Soukhanovskii, J. W. Ahn, J. Canik, N. Crocker, D. A. D'Ippolito, R. Bell, H. Kugel, B. Leblanc, L. A. Roquemore, D. L. Rudakov, and NSTX Team. Edge transport studies in the edge and scrape-off layer of the National Spherical Torus Experiment with Langmuir probes. *Physics of Plasmas*, 21:042309, 2014.
  - [16] D. Carralero, G. Birkenmeier, H. W. Müller, P. Manz, P. DeMarne, S. H. Müller, F. Reimold, U. Stroth, M. Wischmeier, E. Wolfrum, and The ASDEX Upgrade Team. An experimental investigation of the high density transition of the scrape-off layer transport in ASDEX Upgrade. *Nuclear Fusion*, 54:123005, 2014.
  - [17] P. C. Stangeby. *The Plasma Boundary of Magnetic Fusion Devices*. Institute of Physics Publishing, 2000.
  - [18] B. Lipschultz, D. Whyte, and B. LaBombard. Comparison of particle transport in the scrape-off layer plasmas of Alcator C-Mod and DIII-D. *Plasma Physics and Controlled Fusion*, 47:1559, 2005.

- [19] V. Naulin. Turbulent transport and the plasma edge. *Journal of Nuclear Materials*, 363:24, 2007.
- [20] B. LaBombard, M. V. Umansky, R. L. Boivin, J. A. Goetz, J. Hughes, B. Lipschultz, D. Mossessian, C. S. Pitcher, J. L. Terry, and Alcator Group. Cross-field plasma transport and main-chamber recycling in diverted plasmas on Alcator C-Mod. *Nuclear Fusion*, 40:2041, 2000.
- [21] A. Y. Pigarov, S. I. Krasheninnikov, T. D. Rognlien, M. J. Schaffer, and W. P. West. Tokamak edge plasma simulation including anomalous cross-field convective transport. *Physics of Plasmas*, 9:1287, 2002.
- [22] O. E. Garcia, R. A. Pitts, J. Horacek, A. H. Nielsen, W. Fundamenski, J. P. Graves, V. Naulin, and J. Juul Rasmussen. Turbulent transport in the TCV SOL. *Journal of Nuclear Materials*, 363:575, 2007.
- [23] S. Zweben, P. C. Liewer, and R. W. Gould. Edge plasma transport experiments in the Caltech tokamak. *Journal of Nuclear Materials*, 111: 39, 1982.
- [24] S. J. Zweben and R. W. Gould. Scaling of edge-plasma turbulence in the Caltech tokamak. *Nuclear Fusion*, 23:1625, 1983.
- [25] G. R. McKEE, R. J. Fonck, D. K. Gupta, D. J. Schlossberg, M. W. Shafer, R. L. Boivin, and W. Solomon. Plasma turbulence imaging via beam emission spectroscopy in the core of the DIII-D tokamak. *Plasma and Fusion Research*, 2:S1025, 2007.
- [26] A. J. Wootton. Edge turbulence. *Journal of Nuclear Materials*, 176:77, 1990.
- [27] I. Langmuir. Positive ion currents from the positive column of mercury arcs. *Science*, 58:290, 1923.
- [28] H. M. Mott-Smith and I. Langmuir. The theory of collectors in gaseous discharges. *Physical Review*, 28:727, 1926.
- [29] S. J. Zweben, J. L. Terry, D. P. Stotler, and R. J. Maqueda. Invited Review Article: Gas puff imaging diagnostics of edge plasma turbulence in magnetic fusion devices. *Review of Scientific Instruments*, 88:041101, 2017.
- [30] O. E. Garcia. Stochastic modeling of intermittent scrape-off layer plasma fluctuations. *Physical Review Letters*, 108:265001, 2012.

- [31] O.E. Garcia, S. M. Fritzner, R. Kube, I. Cziegler, B. LaBombard, and J. L. Terry. Intermittent fluctuations in the Alcator C-Mod scrape-off layer. *Physics of Plasmas*, 20:055901, 2013.
- [32] O. E. Garcia, I. Cziegler, R. Kube, B. LaBombard, and J. L. Terry. Burst statistics in Alcator C-Mod SOL turbulence. *Journal of Nuclear Materials*, 438:S180, 2013.
- [33] O. E. Garcia, J. Horacek, and R. A. Pitts. Intermittent fluctuations in the TCV scrape-off layer. *Nuclear Fusion*, 55:062002, 2015.
- [34] R. Kube, A. Theodorsen, O. E. Garcia, B. LaBombard, and J. L. Terry. Fluctuation statistics in the scrape-off layer of Alcator C-Mod. *Plasma Physics and Controlled Fusion*, 58:054001, 2016.
- [35] O. E. Garcia, R. Kube, A. Theodorsen, J. G. Bak, S. H. Hong, H. S. Kim, the KSTAR Project Team, and R. A. Pitts. SOL width and intermittent fluctuations in KSTAR. *Nuclear Materials and Energy*, 12:36, 2017.
- [36] R. Kube, O. E. Garcia, A. Theodorsen, D. Brunner, A. Q. Kuang, B. LaBombard, and J. L. Terry. Intermittent electron density and temperature fluctuations and associated fluxes in the Alcator C-Mod scrape-off layer. *Plasma Physics and Controlled Fusion*, 60:065002, 2018.
- [37] O. E. Garcia, R. Kube, A. Theodorsen, B. LaBombard, and J. L. Terry. Intermittent fluctuations in the Alcator C-Mod scrape-off layer for ohmic and high confinement mode plasmas. *Physics of Plasmas*, 25:056103, 2018.
- [38] A. Theodorsen, O. E. Garcia, R. Kube, B. LaBombard, and J. L. Terry. Universality of Poisson-driven plasma fluctuations in the Alcator C-Mod scrape-off layer. *Physics of Plasmas*, 25:122309, 2018.
- [39] A. Theodorsen. Statistical properties of intermittent fluctuations in the boundary of fusion plasmas. *PhD thesis, University of Tromsø*, 2018.
- [40] A. Theodorsen, O. E. Garcia, R. Kube, B. LaBombard, and J. L. Terry. Relationship between frequency power spectra and intermittent, large-amplitude bursts in the Alcator C-Mod scrape-off layer. *Nuclear Fusion*, 57:114004, 2017.
- [41] G. Y. Antar, P. Devynck, X. Garbet, and S. C. Luckhardt. Turbulence intermittency and burst properties in tokamak scrape-off layer. *Physics of Plasmas*, 8:1612, 2001.

- [42] G. Y. Antar, G. Counsell, Y. Yu, B. Labombard, and P. Devynck. Universality of intermittent convective transport in the scrape-off layer of magnetically confined devices. *Physics of Plasmas*, 10:419, 2003.
- [43] J. P. Graves, J. Horacek, R. A. Pitts, and K. I. Hopcraft. Self-similar density turbulence in the TCV tokamak scrape-off layer. *Plasma Physics and Controlled Fusion*, 47:L1, 2005.
- [44] O. E. Garcia, R. A. Pitts, J. Horacek, J. Madsen, V. Naulin, A. H. Nielsen, and J. Juul Rasmussen. Collisionality dependent transport in TCV SOL plasmas. *Plasma Physics and Controlled Fusion*, 49:B47, 2007.
- [45] O. E. Garcia. Blob transport in the plasma edge: a review. *Plasma and Fusion Research*, 4:019, 2009.
- [46] B. Labit, I. Furno, A. Fasoli, A. Diallo, S. H. Müller, G. Plyushchev, M. Podestà, and F. M. Poli. Universal statistical properties of drift-interchange turbulence in TORPEX plasmas. *Physical Review Letters*, 98:255002, 2007.
- [47] F. Sattin, M. Agostini, P. Scarin, N. Vianello, R. Cavazzana, L. Marrelli, G. Serianni, S. J. Zweben, R. J. Maqueda, Y. Yagi, et al. On the statistics of edge fluctuations: comparative study between various fusion devices. *Plasma Physics and Controlled Fusion*, 51:055013, 2009.
- [48] F. Sattin, M. Agostini, R. Cavazzana, G. Serianni, P. Scarin, and N. Vianello. About the parabolic relation existing between the skewness and the kurtosis in time series of experimental data. *Physica Scripta*, 79: 045006, 2009.
- [49] O. E. Garcia, R. Kube, A. Theodorsen, and H. L. Pécseli. Stochastic modelling of intermittent fluctuations in the scrape-off layer: Correlations, distributions, level crossings, and moment estimation. *Physics of Plasmas*, 23:052308, 2016.
- [50] M. A. Pedrosa, C. Hidalgo, B. A. Carreras, R. Balbin, I. García-Cortés, D. Newman, B. Van Milligen, E. Sánchez, J. Bleuel, M. Endler, S. Davies, and G. F. Matthews. Empirical similarity of frequency spectra of the edge-plasma fluctuations in toroidal magnetic-confinement systems. *Physical Review Letters*, 82:3621, 1999.
- [51] B. A. Carreras, R. Balbin, B. Van Milligen, M. A. Pedrosa, I. García-Cortés, E. Sanchez, C. Hidalgo, J. Bleuel, M. Endler, H. Thomsen,

- A. Chankin, S. Davies, K. Erents, and G. F. Matthews. Characterization of the frequency ranges of the plasma edge fluctuation spectra. *Physics of Plasmas*, 6:4615, 1999.
- [52] O. E. Garcia and A. Theodorsen. Auto-correlation function and frequency spectrum due to a super-position of uncorrelated exponential pulses. *Physics of Plasmas*, 24:032309, 2017.
- [53] J. A. Boedo, D. L. Rudakov, E. Hollmann, D. S. Gray, K. H. Burrell, R. A. Moyer, G. R. McKee, R. Fonck, P. C. Stangeby, T. E. Evans, P. B. Snyder, A. W. Leonard, M. A. Mahdavi, M. J. Schaffer, W. P. West, M. E. Fenstermacherd, M. Grothd, S. L. Allend, C. Lasnierd, G. D. Porterd, N. S. Wolfd, R. J. Colchinel, G. Zengf, L. Wangf, J. G. Watkinsg, T. Takahashih, and The DIII-D Team. Edge-localized mode dynamics and transport in the scrape-off layer of the DIII-D tokamak. *Physics of Plasmas*, 12:072516, 2005.
- [54] G. Y. Antar, G. Counsell, and J. W. Ahn. On the scaling of avaloids and turbulence with the average density approaching the density limit. *Physics of Plasmas*, 12:082503, 2005.
- [55] S. J. Zweben. Search for coherent structure within tokamak plasma turbulence. *The Physics of Fluids*, 28:974, 1985.
- [56] S. J. Zweben and R. W. Gould. Structure of edge-plasma turbulence in the Caltech tokamak. *Nuclear Fusion*, 25:171, 1985.
- [57] S. J. Zweben, D. Manos, R. V. Budny, P. Efthimion, E. Fredrickson, H. Greenside, K. W. Hill, S. Hiroe, S. Kilpatrick, K. McGuire, S. S. Medley, H. K. Park, A. T. Ramsey, and J. Wilgen. EDGE TURBULENCE MEASUREMENTS IN TFTR. *Journal of Nuclear Materials*, 145:250, 1987.
- [58] M. Endler, H. Niedermeyer, L. Giannone, E. Kolzhauer, A. Rudyj, G. Theimer, and N. Tsois. Measurements and modelling of electrostatic fluctuations in the scrape-off layer of ASDEX. *Nuclear Fusion*, 35:1307, 1995.
- [59] M. Endler. Turbulent SOL transport in stellarators and tokamaks. *Journal of Nuclear Materials*, 266:84, 1999.
- [60] M. V. Umansky, S. I. Krasheninnikov, B. LaBombard, and J. L. Terry. Comments on particle and energy balance in the edge plasma of Alcator C-Mod. *Physics of Plasmas*, 5:3373, 1998.

- [61] D. A. D'ippolito, J. R. Myra, and S. J. Zweben. Convective transport by intermittent blob-filaments: Comparison of theory and experiment. *Physics of Plasmas*, 18:060501, 2011.
- [62] A. Kirk, A. J. Thornton, J. R. Harrison, F. Militello, and N. R. Walkden. L-mode filament characteristics on MAST as a function of plasma current measured using visible imaging. *Plasma Physics and Controlled Fusion*, 58:085008, 2016.
- [63] B. D. Dudson, N. B. Ayed, A. Kirk, H. R. Wilson, G. Counsell, X. Xu, M. Umansky, P. B. Snyder, B. LLoyd, and the MAST team. Experiments and simulation of edge turbulence and filaments in MAST. *Plasma Physics and Controlled Fusion*, 50:124012, 2008.
- [64] S. J. Zweben, D. P. Stotler, J. L. Terry, B. LaBombard, M. Greenwald, M. Muterspaugh, C. S. Pitcher, Alcator C-Mod Group, K. Hallatschek, R. J. Maqueda, et al. Edge turbulence imaging in the Alcator C-Mod tokamak. *Physics of Plasmas*, 9:1981, 2002.
- [65] R. Kube, O. E. Garcia, B. LaBombard, J. L. Terry, and S. J. Zweben. Blob sizes and velocities in the Alcator C-Mod scrape-off layer. *Journal of Nuclear Materials*, 438:S505, 2013.
- [66] J. R. Myra, D. A. D'Ippolito, D. P. Stotler, S. J. Zweben, B. P. LeBlanc, J. E. Menard, R. J. Maqueda, and J. Boedo. Blob birth and transport in the tokamak edge plasma: Analysis of imaging data. *Physics of Plasmas*, 13:092509, 2006.
- [67] J. A. Boedo, D. Rudakov, R. Moyer, S. Krasheninnikov, D. Whyte, G. McKee, G. Tynan, M. Schaffer, P. Stangeby, P. West, et al. Transport by intermittent convection in the boundary of the DIII-D tokamak. *Physics of Plasmas*, 8:4826, 2001.
- [68] C. Silva, B. Goncalves, C. Hidalgo, M. A. Pedrosa, K. Erents, G. Matthews, and R. A. Pitts. Fluctuation measurements using a five-pin triple probe in the Joint European Torus boundary plasma. *Review of Scientific Instruments*, 75:4314, 2004.
- [69] D. Carralero, P. Manz, L. Aho-Mantila, G. Birkenmeier, M. Brix, M. Groth, H. W. Müller, U. Stroth, N. Vianello, E. Wolfrum, and ASDEX Upgrade team. Experimental validation of a filament transport model in turbulent magnetized plasmas. *Physical Review Letters*, 115: 215002, 2015.

- [70] S. H. Müller, C. Theiler, A. Fasoli, I. Furno, B. Labit, G. R. Tynan, M. Xu, Z. Yan, and J. H. Yu. Studies of blob formation, propagation and transport mechanisms in basic experimental plasmas (TORPEX and CSDX). *Plasma Physics and Controlled Fusion*, 51:055020, 2009.
- [71] N. B. Ayed, A. Kirk, B. Dudson, S. Tallents, R. G. L. Vann, H. R. Wilson, and the MAST team. Inter-ELM filaments and turbulent transport in the Mega-Amp Spherical Tokamak. *Plasma Physics and Controlled Fusion*, 51:035016, 2009.
- [72] G. S. Xu, V. Naulin, W. Fundamenski, J. Juul Rasmussen, A. H. Nielsen, and B. N. Wan. Intermittent convective transport carried by propagating electromagnetic filamentary structures in nonuniformly magnetized plasma. *Physics of Plasmas*, 17:022501, 2010.
- [73] R. J. Maqueda, D. P. Stotler, S. J. Zweben, and NSTX team. Intermittency in the scrape-off layer of the National Spherical Torus Experiment during H-mode confinement. *Journal of Nuclear Materials*, 415:S459, 2011.
- [74] O. Grulke, J. L. Terry, I. Cziegler, B. LaBombard, and O. E. Garcia. Experimental investigation of the parallel structure of fluctuations in the scrape-off layer of Alcator C-Mod. *Nuclear Fusion*, 54:043012, 2014.
- [75] S. J. Zweben, W. M. Davis, S. M. Kaye, J. R. Myra, R. E. Bell, B. P. LeBlanc, R. J. Maqueda, T. Munsat, S. A. Sabbagh, Y. Sechrest, D. P. Stotler, and the NSTX Team. Edge and SOL turbulence and blob variations over a large database in NSTX. *Nuclear Fusion*, 55:093035, 2015.
- [76] C. Theiler, I. Furno, P. Ricci, A. Fasoli, B. Labit, S. H. Müller, and G. Plyushchev. Cross-field motion of plasma blobs in an open magnetic field line configuration. *Physical Review Letters*, 103:065001, 2009.
- [77] J. R. Angus, S. I. Krasheninnikov, and M. V. Umansky. Effects of parallel electron dynamics on plasma blob transport. *Physics of Plasmas*, 19:082312, 2012.
- [78] O. E. Garcia, N. H. Bian, and W. Fundamenski. Radial interchange motions of plasma filaments. *Physics of Plasmas*, 13:082309, 2006.
- [79] R. Kube and O. E. Garcia. Effect of dynamical friction on interchange motion of plasma filaments. *Physics of Plasmas*, 19:042305, 2012.

- [80] R. Kube, O. E. Garcia, and M. Wiesenberger. Amplitude and size scaling for interchange motions of plasma filaments. *Physics of Plasmas*, 23:122302, 2016.
- [81] J. L. Terry, N. P. Basse, I. Cziegler, M. Greenwald, O. Grulke, B. LaBombard, S. J. Zweben, E. M. Edlund, J. W. Hughes, L. Lin, M. Porkolab, M. Sampsell, B. Veto, and S. J. Wukitch. Transport phenomena in the edge of Alcator C-Mod plasmas. *Nuclear Fusion*, 45:1321, 2005.
- [82] M. Agostini, S. J. Zweben, R. Cavazzana, P. Scarin, G. Serianni, R. J. Maqueda, and D. P. Stotler. Study of statistical properties of edge turbulence in the National Spherical Torus Experiment with the gas puff imaging diagnostic. *Physics of Plasmas*, 14:102305, 2007.
- [83] C. Theiler, A. Diallo, A. Fasoli, I. Furno, B. Labit, M. Podestà, F. M. Poli, and P. Ricci. The role of the density gradient on intermittent cross-field transport events in a simple magnetized toroidal plasma. *Physics of Plasmas*, 15:042303, 2008.
- [84] S. H. Müller, A. Diallo, A. Fasoli, I. Furno, B. Labit, and M. Podesta. Plasma blobs in a basic toroidal experiment: Origin, dynamics, and induced transport. *Physics of Plasmas*, 14:110704, 2007.
- [85] I. Furno, B. Labit, M. Podestà, A. Fasoli, S. H. Müller, F. M. Poli, P. Ricci, C. Theiler, S. Brunner, A. Diallo, and J. Graves. Experimental observation of the blob-generation mechanism from interchange waves in a plasma. *Physical Review Letters*, 100:055004, 2008.
- [86] I. Furno, B. Labit, A. Fasoli, F. M. Poli, P. Ricci, C. Theiler, S. Brunner, A. Diallo, J. P. Graves, M. Podestà, and S. H. Müller. Mechanism for blob generation in the TORPEX toroidal plasma. *Physics of Plasmas*, 15:055903, 2008.
- [87] O. E. Garcia, V. Naulin, A. H. Nielsen, and J. Juul Rasmussen. Computations of intermittent transport in scrape-off layer plasmas. *Physical Review Letters*, 92:165003, 2004.
- [88] N. Bisai, A. Das, S. Deshpande, R. Jha, P. Kaw, A. Sen, and R. Singh. Edge and scrape-off layer tokamak plasma turbulence simulation using two-field fluid model. *Physics of Plasmas*, 12:072520, 2005.
- [89] D. A. Russell, J. R. Myra, and D. A. D'Ippolito. Collisionality and magnetic geometry effects on tokamak edge turbulent transport. II. Many-blob turbulence in the two-region model. *Physics of Plasmas*, 14:102307, 2007.

- [90] D. A. Russell, J. R. Myra, and D. A. D'Ippolito. Saturation mechanisms for edge turbulence. *Physics of Plasmas*, 16:122304, 2009.
- [91] S. I. Krasheninnikov and A. I. Smolyakov. Generation of mesoscale convective structures in tokamak edge plasma. *Physics of Plasmas*, 14:102503, 2007.
- [92] S. I. Krasheninnikov and A. I. Smolyakov. Dynamics and generation mechanisms of mesoscale structures in tokamak edge plasmas. *Physics of Plasmas*, 15:055909, 2008.
- [93] P. Manz, T. T. Ribeiro, B. D. Scott, G. Birkenmeier, D. Carralero, G. Fuchert, S. H. Müller, H. W. Müller, U. Stroth, and E. Wolfrum. Origin and turbulence spreading of plasma blobs. *Physics of Plasmas*, 22:022308, 2015.
- [94] C. S. Chang and S. Ku. Spontaneous rotation sources in a quiescent tokamak edge plasma. *Physics of Plasmas*, 15:062510, 2008.
- [95] R. M. Churchill, C. S. Chang, S. Ku, and J. Dominski. Pedestal and edge electrostatic turbulence characteristics from an XGC1 gyrokinetic simulation. *Plasma Physics and Controlled Fusion*, 59:105014, 2017.
- [96] J. Madsen. Full-F gyrofluid model. *Physics of Plasmas*, 20:072301, 2013.
- [97] M. Wiesenberger, J. Madsen, and A. Kendl. Radial convection of finite ion temperature, high amplitude plasma blobs. *Physics of Plasmas*, 21:092301, 2014.
- [98] M. Held, M. Wiesenberger, J. Madsen, and A. Kendl. The influence of temperature dynamics and dynamic finite ion Larmor radius effects on seeded high amplitude plasma blobs. *Nuclear Fusion*, 56:126005, 2016.
- [99] T. T. Ribeiro and B. Scott. Tokamak turbulence computations on closed and open magnetic flux surfaces. *Plasma Physics and Controlled Fusion*, 47:1657, 2005.
- [100] T. T. Ribeiro and B. Scott. Gyrofluid turbulence studies of the effect of the poloidal position of an axisymmetric Debye sheath. *Plasma Physics and Controlled Fusion*, 50:055007, 2008.
- [101] S. I. Braginskii. Transport processes in a plasma. *Reviews of Plasma Physics*, 1965.

- [102] N. Bian, S. Benkadda, J. V. Paulsen, and O. E. Garcia. Blobs and front propagation in the scrape-off layer of magnetic confinement devices. *Physics of Plasmas*, 10:671, 2003.
- [103] J. R. Angus, M. V. Umansky, and S. I. Krasheninnikov. Effect of drift waves on plasma blob dynamics. *Physical Review Letters*, 108:215002, 2012.
- [104] N .R. Walkden, B. D. Dudson, and G. Fishpool. Characterization of 3D filament dynamics in a MAST SOL flux tube geometry. *Plasma Physics and Controlled Fusion*, 55:105005, 2013.
- [105] L. Easy, F. Militello, J. Omotani, B. Dudson, E. Havlíčková, P. Tamain, V. Naulin, and A. H. Nielsen. Three dimensional simulations of plasma filaments in the scrape off layer: A comparison with models of reduced dimensionality. *Physics of Plasmas*, 21:122515, 2014.
- [106] L. Easy, F. Militello, J. Omotani, N. R. Walkden, and B. Dudson. Investigation of the effect of resistivity on scrape off layer filaments using three-dimensional simulations. *Physics of Plasmas*, 23:012512, 2016.
- [107] F. Militello, N. R. Walkden, T. Farley, W. A. Gracias, J. Olsen, F. Riva, L. Easy, N. Fedorczak, I. Lupelli, J. Madsen, A. H. Nielsen, P. Ricci, P. Tamain, and J. Young. Multi-code analysis of scrape-off layer filament dynamics in MAST. *Plasma Physics and Controlled Fusion*, 58:105002, 2016.
- [108] F. Riva, C. Colin, J. Denis, L. Easy, I. Furno, J. Madsen, F. Militello, V. Naulin, A. H. Nielsen, J. M. B. Olsen, J. T. Omotani, J. Juul Rasmussen, P. Ricci, E. Serre, P. Tamain, and C. Theiler. Blob dynamics in the TORPEX experiment: a multi-code validation. *Plasma Physics and Controlled Fusion*, 58:044005, 2016.
- [109] W. Lee, J. R. Angus, M. V. Umansky, and S. I. Krasheninnikov. Electromagnetic effects on plasma blob-filament transport. *Journal of Nuclear Materials*, 463:765, 2015.
- [110] P. W. Gingell, S. C. Chapman, R. O. Dendy, and C. S. Brady. Transport and evolution of ion gyro-scale plasma blobs in perpendicular magnetic fields. *Plasma Physics and Controlled Fusion*, 54:065005, 2012.
- [111] P. W. Gingell, S. C. Chapman, and R. O. Dendy. Plasma blob formation by ion kinetic Kelvin-Helmholtz and interchange instabilities. *Plasma Physics and Controlled Fusion*, 56:035012, 2014.

- [112] O. E. Garcia, N. H. Bian, V. Naulin, A. H. Nielsen, and J. Juul Rasmussen. Mechanism and scaling for convection of isolated structures in nonuniformly magnetized plasmas. *Physics of Plasmas*, 12:090701, 2005.
- [113] R. Kube and O. E. Garcia. Velocity scaling for filament motion in scrape-off layer plasmas. *Physics of Plasmas*, 18:102314, 2011.
- [114] F. Militello, B. Dudson, L. Easy, A. Kirk, and P. Naylor. On the interaction of scrape off layer filaments. *Plasma Physics and Controlled Fusion*, 59:125013, 2017.
- [115] A. Kendl. Gyrofluid vortex interaction. *Plasma Physics and Controlled Fusion*, 60:025017, 2018.
- [116] O. Pogutse, W. Kerner, V. Gribkov, S. Bazdenkov, and M. Osipenko. The resistive interchange convection in the edge of tokamak plasmas. *Plasma Physics and Controlled Fusion*, 36:1963, 1994.
- [117] P. Beyer and K. H. Spatschek. Center manifold theory for the dynamics of the L-H-transition. *Physics of Plasmas*, 3:995, 1996.
- [118] W. Horton, G. Hu, and G. Laval. Turbulent transport in mixed states of convective cells and sheared flows. *Physics of Plasmas*, 3:2912, 1996.
- [119] M. Berning and K. H. Spatschek. Bifurcations and transport barriers in the resistive-g paradigm. *Physical Review E*, 62:1162, 2000.
- [120] O. E. Garcia, N. H. Bian, J. V. Paulsen, S. Benkadda, and K. Rypdal. Confinement and bursty transport in a flux-driven convection model with sheared flows. *Plasma Physics and Controlled Fusion*, 45:919, 2003.
- [121] O. E. Garcia and N. H. Bian. Bursting and large-scale intermittency in turbulent convection with differential rotation. *Physical Review E*, 68: 047301, 2003.
- [122] O. E. Garcia, N. H. Bian, V. Naulin, A. H. Nielsen, and J. Juul Rasmussen. Two-dimensional convection and interchange motions in fluids and magnetized plasmas. *Physica Scripta*, 2006:104, 2006.
- [123] G. Dechristoforo, A. Theodorsen, and O. E. Garcia. Intermittent fluctuations due to Lorentzian pulses in turbulent thermal convection. *Physics of Fluids*, 32:085102, 2020.
- [124] S. Benkadda, X. Garbet, and A. Verga. Interchange instability turbulence model in edge tokamak plasma. *Contributions to Plasma Physics*, 34:247, 1994.

- [125] Y. Sarazin and P. Ghendrih. Intermittent particle transport in two-dimensional edge turbulence. *Physics of Plasmas*, 5:4214, 1998.
- [126] V. Naulin, A. H. Nielsen, and J. Juul Rasmussen. Dispersion of ideal particles in a two-dimensional model of electrostatic turbulence. *Physics of Plasmas*, 6:4575, 1999.
- [127] O. E. Garcia. Two-field transport models for magnetized plasmas. *Journal of Plasma Physics*, 65:81, 2001.
- [128] P. Ghendrih, Y. Sarazin, G. Attuel, S. Benkadda, P. Beyer, G. Falchetto, C. Figarella, X. Garbet, V. Grandgirard, and M. Ottaviani. Theoretical analysis of the influence of external biasing on long range turbulent transport in the scrape-off layer. *Nuclear Fusion*, 43:1013, 2003.
- [129] Y. Sarazin, Ph. Ghendrih, G. Attuel, C. Clément, X. Garbet, V. Grandgirard, M. Ottaviani, S. Benkadda, P. Beyer, N. Bian, et al. Theoretical understanding of turbulent transport in the SOL. *Journal of Nuclear Materials*, 313:796, 2003.
- [130] N. Bisai, A. Das, S. Deshpande, R. Jha, P. Kaw, A. Sen, and R. Singh. Simulation of plasma transport by coherent structures in scrape-off-layer tokamak plasmas. *Physics of Plasmas*, 11:4018, 2004.
- [131] O. E. Garcia, V. Naulin, A. H. Nielsen, and J. Juul Rasmussen. Turbulence and intermittent transport at the boundary of magnetized plasmas. *Physics of Plasmas*, 12:062309, 2005.
- [132] N. Bisai, A. Das, S. Deshpande, R. Jha, P. Kaw, A. Sen, and R. Singh. Formation of a density blob and its dynamics in the edge and the scrape-off layer of a tokamak plasma. *Physics of Plasmas*, 12:102515, 2005.
- [133] O. E. Garcia, V. Naulin, A. H. Nielsen, and J. Juul Rasmussen. Turbulence simulations of blob formation and radial propagation in toroidally magnetized plasmas. *Physica Scripta*, 2006:89, 2006.
- [134] F. Militello, W. Fundamenski, V. Naulin, and A. H. Nielsen. Simulations of edge and scrape off layer turbulence in mega ampere spherical tokamak plasmas. *Plasma Physics and Controlled Fusion*, 54:095011, 2012.
- [135] V. Naulin. Electromagnetic transport components and sheared flows in drift-alfvén turbulence. *Physics of Plasmas*, 10:4016, 2003.
- [136] V. Naulin, O. E. Garcia, A. H. Nielsen, and J. Juul Rasmussen. Statistical properties of transport in plasma turbulence. *Physics Letters A*, 321:355, 2004.

- [137] G. Decristoforo, A. Theodorsen, J. Omotani, T. Nicholas, and O. E. Garcia. Numerical turbulence simulations of intermittent fluctuations in the scrape-off layer of magnetized plasmas. *arXiv:2102.04723*, 2021.
- [138] F. Nespoli, I. Furno, B. Labit, P. Ricci, F. Avino, F. D. Halpern, F. Musil, and F. Riva. Blob properties in full-turbulence simulations of the TCV scrape-off layer. *Plasma Physics and Controlled Fusion*, 59:055009, 2017.
- [139] F. Nespoli, P. Tamain, N. Fedorczak, G. Ciraolo, D. Galassi, R. Tatali, E. Serre, Y. Marandet, H. Bufferand, and P. Ghendrih. 3D structure and dynamics of filaments in turbulence simulations of WEST diverted plasmas. *Nuclear Fusion*, 59:096006, 2019.
- [140] P. Paruta, C. Beadle, P. Ricci, and C. Theiler. Blob velocity scaling in diverted tokamaks: A comparison between theory and simulation. *Physics of Plasmas*, 26:032302, 2019.
- [141] G. Decristoforo, F. Militello, T. Nicholas, J. Omotani, C. Marsden, N. Walkden, and O. E. Garcia. Blob interactions in 2D scrape-off layer simulations. *Physics of Plasmas*, 27:122301, 2020.
- [142] V. Naulin, A. Kendl, O. E. Garcia, A. H. Nielsen, and J. Juul Rasmussen. Shear flow generation and energetics in electromagnetic turbulence. *Physics of Plasmas*, 12:052515, 2005.
- [143] P. Ricci, F. D. Halpern, S. Jolliet, J. Loizu, A. Mosetto, A. Fasoli, I. Furno, and C. Theiler. Simulation of plasma turbulence in scrape-off layer conditions: the GBS code, simulation results and code validation. *Plasma Physics and Controlled Fusion*, 54:124047, 2012.
- [144] P. Tamain, H. Bufferand, G. Ciraolo, C. Colin, P. Ghendrih, F. Schwander, and E. Serre. 3D Properties of Edge Turbulent Transport in Full-Torus Simulations and their Impact on Poloidal Asymmetries. *Contributions to Plasma Physics*, 54:555, 2014.
- [145] B. D. Dudson and J. Leddy. Hermes: global plasma edge fluid turbulence simulations. *Plasma Physics and Controlled Fusion*, 59:054010, 2017.
- [146] A. Stegmeir, D. Coster, A. Ross, O. Maj, K. Lackner, and E. Poli. GRILLIX: a 3D turbulence code based on the flux-coordinate independent approach. *Plasma Physics and Controlled Fusion*, 60:035005, 2018.
- [147] T. E. G. Nicholas, J. Omotani, F. Riva, F. Militello, and B. Dudson. Comparing Two- and Three-Dimensional Models of Scrape-Off-Layer Turbulent Transport. *arXiv:2103.09727*, 2021.

- [148] F. Riva, F. Militello, S. Elmore, J. T. Omotani, B. Dudson, N. R. Walkden, and the MAST team. Three-dimensional plasma edge turbulence simulations of the Mega Ampere Spherical Tokamak and comparison with experimental measurements. *Plasma Physics and Controlled Fusion*, 61: 095013, 2019.
- [149] F. Militello. *Boundary plasma physics - An accessible guide to transport, detachment and divertor design*. To be published in Springer Nature, 2021.
- [150] D. Hoare, F. Militello, J. T. Omotani, F. Riva, S. Newton, T. Nicholas, D. Ryan, and N. R. Walkden. Dynamics of scrape-off layer filaments in high  $\beta$  plasmas. *Plasma Physics and Controlled Fusion*, 61:105013, 2019.
- [151] M. Kočan, R. Pánek, J. Stöckel, M. Hron, J. P. Gunn, and R. Dejarnac. Ion temperature measurements in the tokamak scrape-off layer. *Journal of Nuclear Materials*, 363:1436, 2007.
- [152] M. Kočan, F. P. Gennrich, A. Kendl, H. W. Müller, and ASDEX Upgrade Team. Ion temperature fluctuations in the ASDEX Upgrade scrape-off layer. *Plasma Physics and Controlled Fusion*, 54, 2012.
- [153] S. Ahmed. Effects of ion temperature on Scrape-off layer filaments. *Master thesis, University of Bath*, 2020.
- [154] N. R. Walkden, L. Easy, F. Militello, and J. T. Omotani. Dynamics of 3D isolated thermal filaments. *Plasma Physics and Controlled Fusion*, 58:115010, 2016.
- [155] W. Fundamenski, O. E. Garcia, V. Naulin, R. A. Pitts, A. H. Nielsen, J. Juul Rasmussen, J. Horacek, J. P. Graves, and JET EFDA contributors. Dissipative processes in interchange driven scrape-off layer turbulence. *Nuclear Fusion*, 47:417, 2007.
- [156] P. M. Bellan. *Fundamentals of plasma physics*. Cambridge University Press, 2008.
- [157] O. Meyer. Drift wave turbulence and zonal flows. *Master thesis, University of Tromsø*, 2012.
- [158] T. Nicholas. Reduced Simulations of Scrape-Off-Layer Turbulence. *PhD thesis, University of York*, 2021.
- [159] J. L. Terry, S. J. Zweben, K. Hallatschek, B. LaBombard, R. J. Maqueda, B. Bai, C. J. Boswell, M. Greenwald, D. Kopon, W. M. Nevins, C. S.

- Pitcher, B. N. Rogers, D. P. Stotler, and X. Q. Xu. Observations of the turbulence in the scrape-off-layer of Alcator C-Mod and comparisons with simulation. *Physics of Plasmas*, 10:1739, 2003.
- [160] M. Wensing, B. P. Duval, O. Février, A. Fil, D. Galassi, E. Havlickova, A. Perek, H. Reimerdes, C. Theiler, K. Verhaegh, M. Wischmeier, the EUROfusion MST1 team, and the TCV team. SOLPS-ITER simulations of the TCV divertor upgrade. *Plasma Physics and Controlled Fusion*, 61: 085029, 2019.
- [161] J. G. Bak, H. S. Kim, M. K. Bae, J. W. Juhn, D. C. Seo, E. N. Bang, S. B. Shim, K. S. Chung, H. J. Lee, and S. H. Hong. Investigation of SOL parameters and divertor particle flux from electric probe measurements in KSTAR. *Journal of Nuclear Materials*, 463:424, 2015.
- [162] F. Militello and W. Fundamenski. Multi-machine comparison of drift fluid dimensionless parameters. *Plasma Physics and Controlled Fusion*, 53:095002, 2011.
- [163] O. E. Garcia. Convecive Transport and Shear Flows in Fluids and Magnetized Plasmas. *PhD thesis, University of Tromsø*, 2002.
- [164] H. Bénard. Les tourbillons cellulaires dans une nappe liquide.-Méthodes optiques d'observation et d'enregistrement. *Journal de Physique Théorique et Appliquée*, 10:254, 1901.
- [165] Lord Rayleigh. On convection currents in a horizontal layer of fluid, when the higher temperature is on the under side. *The London, Edinburgh, and Dublin Philosophical Magazine and Journal of Science*, 32:529, 1916.
- [166] F. H. Busse. Non-linear properties of thermal convection. *Reports on Progress in Physics*, 41:1929, 1978.
- [167] E. D. Siggia. High Rayleigh number convection. *Annual Review of Fluid Mechanics*, 26:137, 1994.
- [168] E. Bodenschatz, W. Pesch, and G. Ahlers. Recent developments in Rayleigh-Bénard convection. *Annual Review of Fluid Mechanics*, 32: 709, 2000.
- [169] L. P. Kadanoff. Turbulent heat flow: structures and scaling. *Physics Today*, 54:34, 2001.
- [170] G. Ahlers and D. Grossmann, S. Lohse. Heat transfer and large scale dynamics in turbulent Rayleigh-Bénard convection. *Reviews of Modern Physics*, 81:503, 2009.

- [171] N. Campbell. The study of discontinuous phenomena. In *Proceedings of the Cambridge Philosophical Society*, volume 15, page 117, 1909.
- [172] S. O. Rice. Mathematical analysis of random noise. *The Bell System Technical Journal*, 23:282, 1944.
- [173] S. O. Rice. Mathematical analysis of random noise. *The Bell System Technical Journal*, 24:46, 1945.
- [174] J. R. Segal, B. Ceccarelli, R. Fesce, and W. P. Hurlbut. Miniature end-plate potential frequency and amplitude determined by an extension of Campbell's theorem. *Biophysical Journal*, 47:183, 1985.
- [175] R. Fesce, J. R. Segal, and W. P. Hurlbut. Fluctuation analysis of nonideal shot noise. Application to the neuromuscular junction. *The Journal of General Physiology*, 88:25, 1986.
- [176] J. W. Jang. Martingale approach for moments of discounted aggregate claims. *Journal of Risk and Insurance*, 71:201, 2004.
- [177] P. Claps, A. Giordano, and F. Laio. Advances in shot noise modeling of daily streamflows. *Advances in Water Resources*, 28:992, 2005.
- [178] M. Lefebvre. Generalized filtered Poisson processes and application in hydrology. *Statistics & Probability Letters*, 78:3274, 2008.
- [179] E. Daly and A. Porporato. Effect of different jump distributions on the dynamics of jump processes. *Physical Review E*, 81:061133, 2010.
- [180] Z. Elter, C. Jammes, I. Pázsit, L. Pál, and P. Filliatre. Performance investigation of the pulse and Campbeling modes of a fission chamber using a Poisson pulse train simulation code. *Nuclear Instruments and Methods in Physics Research Section A: Accelerators, Spectrometers, Detectors and Associated Equipment*, 774:60, 2015.
- [181] O. E. Garcia and A. Theodorsen. Skewed Lorentzian pulses and exponential frequency power spectra. *Physics of Plasmas*, 25:014503, 2018.
- [182] J. E. Maggs and G. J. Morales. Generality of deterministic chaos, exponential spectra, and Lorentzian pulses in magnetically confined plasmas. *Physical Review Letters*, 107:185003, 2011.
- [183] B. P. Van Milligen, R. Sánchez, and C. Hidalgo. Relevance of Uncorrelated Lorentzian Pulses for the Interpretation of Turbulence in the Edge of Magnetically Confined Toroidal Plasmas. *Physical Review Letters*, 109:105001, 2012.

- [184] J. E. Maggs, T. L. Rhodes, and G. J. Morales. Chaotic density fluctuations in L-mode plasmas of the DIII-D tokamak. *Plasma Physics and Controlled Fusion*, 57:045004, 2015.
- [185] Z. Zhu, A. E. White, T. A. Carter, S. G. Baek, and J. L. Terry. Chaotic edge density fluctuations in the Alcator C-Mod tokamak. *Physics of Plasmas*, 24:042301, 2017.
- [186] O. E. Garcia and A. Theodorsen. Power law spectra and intermittent fluctuations due to uncorrelated Lorentzian pulses. *Physics of Plasmas*, 24:020704, 2017.
- [187] A. Theodorsen and O. E. Garcia. Probability distribution functions for intermittent scrape-off layer plasma fluctuations. *Plasma Physics and Controlled Fusion*, 60:034006, 2018.
- [188] O. E. Garcia and A. Theodorsen. Intermittent fluctuations due to uncorrelated Lorentzian pulses. *Physics of Plasmas*, 25:014506, 2018.
- [189] Y. Marandet, N. Nace, M. Valentinuzzi, P. Tamain, H. Bufferand, G. Ciraolo, P. Genesio, and N. Mellet. Assessment of the effects of scrape-off layer fluctuations on first wall sputtering with the TOKAM-2D turbulence code. *Plasma Physics and Controlled Fusion*, 58:114001, 2016.
- [190] A. Theodorsen and O. E. Garcia. Level crossings and excess times due to a superposition of uncorrelated exponential pulses. *Physical Review E*, 97:012110, 2018.
- [191] F. Militello and J. T. Omotani. On the relation between non-exponential scrape off layer profiles and the dynamics of filaments. *Plasma Physics and Controlled Fusion*, 58:125004, 2016.
- [192] N. R. Walkden, A. Wynn, F. Militello, B. Lipschultz, G. Matthews, C. Guillemaut, J. Harrison, D. Moulton, and JET Contributors. Interpretation of scrape-off layer profile evolution and first-wall ion flux statistics on JET using a stochastic framework based on filamentary motion. *Plasma Physics and Controlled Fusion*, 59:085009, 2017.
- [193] F. Militello, T. Farley, K. Mukhi, N. Walkden, and J. T. Omotani. A two-dimensional statistical framework connecting thermodynamic profiles with filaments in the scrape off layer and application to experiments. *Physics of Plasmas*, 25:056112, 2018.

- [194] F. Militello. Understanding density decay lengths and particle exhaust in tokamaks. *16th European Fusion Theory Conference*, 2015.
- [195] R. Kube, A. Theodorsen, O. E. Garcia, D. Brunner, B. LaBombard, and J. L. Terry. Comparison between mirror Langmuir probe and gas puff imaging measurements of intermittent fluctuations in the Alcator C-Mod scrape-off layer. *arXiv:2005.02145*, 2020.
- [196] W. H. Richardson. Bayesian-based iterative method of image restoration. *Journal of the Optical Society of America*, 62:55, 1972.
- [197] L. B. Lucy. An iterative technique for the rectification of observed distributions. *The Astronomical Journal*, 79:745, 1974.
- [198] F. Dell'Acqua, G. Rizzo, P. Scifo, R. A. Clarke, G. Scotti, and F. Fazio. A model-based deconvolution approach to solve fiber crossing in diffusion-weighted MR imaging. *IEEE Transactions on Biomedical Engineering*, 54:462, 2007.
- [199] M. Wiesenberger. Gyrofluid computations of filament dynamics in tokamak scrape-off layers. *PhD thesis, University of Innsbruck*, 2014.
- [200] M. Held, M. Wiesenberger, R. Kube, and A. Kendl. Non-Oberbeck–Boussinesq zonal flow generation. *Nuclear Fusion*, 58:104001, 2018.
- [201] D. A. Russell, J. R. Myra, D. A. D'Ippolito, T. L. Munsat, Y. Sechrest, R. J. Maqueda, D. P. Stotler, S. J. Zweben, and NSTX Team. Comparison of scrape-off layer turbulence simulations with experiments using a synthetic gas puff imaging diagnostic. *Physics of Plasmas*, 18:022306, 2011.
- [202] Y. Marandet, P. Tamain, R. Futterer, P. Ghendrih, H. Bufferand, P. Genesio, and A. Mekkaoui. Influence of neutral particles on scrape-off layer turbulence with application to the interpretation of fast camera data. *Journal of Nuclear Materials*, 438:S518, 2013.
- [203] A. S. Thrysøe, M. Løiten, J. Madsen, V. Naulin, A. H. Nielsen, and J. Juul Rasmussen. Plasma particle sources due to interactions with neutrals in a turbulent scrape-off layer of a toroidally confined plasma. *Physics of Plasmas*, 25:032307, 2018.
- [204] N. Bisai and P. K. Kaw. Influence of hot and cold neutrals on scrape-off layer tokamak plasma turbulence. *Physics of Plasmas*, 25:012503, 2018.



# Paper I: Intermittent fluctuations due to Lorentzian pulses in turbulent ther- mal convection

G. Decristoforo, A. Theodorsen and O. E. Garcia,  
Physics of Fluids **32**, 085102 (2020),  
doi:10.1063/5.0012017



## Intermittent fluctuations due to Lorentzian pulses in turbulent thermal convection

Cite as: Phys. Fluids **32**, 085102 (2020); <https://doi.org/10.1063/5.0012017>

Submitted: 30 April 2020 . Accepted: 14 July 2020 . Published Online: 03 August 2020

G. Decristoforo , A. Theodorsen , and O. E. Garcia 



View Online



Export Citation



CrossMark

### ARTICLES YOU MAY BE INTERESTED IN

[Analysis of combustion acoustic phenomena in compression-ignition engines using large eddy simulation](#)

Physics of Fluids **32**, 085101 (2020); <https://doi.org/10.1063/5.0011929>

[Smoothed particle hydrodynamics simulation of converging Richtmyer-Meshkov instability](#)

Physics of Fluids **32**, 086102 (2020); <https://doi.org/10.1063/5.0015589>

[Visualizing the effectiveness of face masks in obstructing respiratory jets](#)

Physics of Fluids **32**, 061708 (2020); <https://doi.org/10.1063/5.0016018>

NEW!

Sign up for topic alerts  
New articles delivered to your inbox





# Paper II: Dirac comb and exponential frequency spectra in chaotic dynamics

A. Theodorsen, G. Decristoforo and O. E. Garcia,  
To be submitted to Chaos: An Interdisciplinary Journal of Nonlinear Science



## **Dirac comb and exponential frequency spectra in chaotic dynamics**

A. Theodorsen, G. Decristoforo and O. E. Garcia

*Department of Physics and Technology, UiT The Arctic University of Norway,  
N-9037 Tromsø, Norway*

An exponential frequency power spectral density is a well known property of many continuous time chaotic systems and has been attributed to the presence of Lorentzian-shaped pulses. Here a stochastic modelling of such fluctuations are presented, describing these as a super-position of pulses with fixed shape and constant duration. Closed form expressions are derived for the lowest order moments, auto-correlation function and frequency power spectral density in the case of periodic pulse arrivals and a random distribution of pulse amplitudes. In general, the spectrum is a Dirac comb located at multiples of the periodicity time and modulated by the pulse spectrum. Randomness in the pulse arrival times is investigated by numerical realizations of the process and the results are discussed in the context of some well-known chaos models.

## I. INTRODUCTION

An intrinsic property of deterministic chaos in continuous time systems is an exponential frequency power spectral density (PSD) for the fluctuations.<sup>1–10</sup> This has been observed in numerous experiments and model simulations of fluids and magnetized plasmas. Recently, the exponential spectrum has been attributed to the presence of Lorentzian pulses in the temporal dynamics.<sup>11–21</sup> Weakly non-linear systems are often characterized by a quasi-periodic oscillations, resulting in a frequency power spectral density resembling a Dirac comb.<sup>19–27</sup> Far from the linear instability threshold the spectral peaks broaden and in many cases an exponential spectrum results.<sup>1–27</sup>

Many chaotic systems, including the Lorenz and the Rössler models, display quasi-periodic orbits with Lorentzian-shaped pulses close to the primary instability threshold. The associated PSD has sharp peaks at frequencies corresponding to the periodicity of the oscillations, resembling a Dirac comb. The Lorentzian-shaped pulses lead to an exponential modulation of the amplitude of the spectral peaks. With period-doubling the density of spectral peaks increases and in the chaotic state the spectral peaks broadens and the PSD is eventually an exponential function of frequency.

In this contribution, we present a stochastic model that describes a super-position of Lorentzian pulses and the resulting frequency spectra.<sup>28–30</sup> The model is based on the process known as shot noise or filtered Poisson process.<sup>31–41</sup> This model has recently been used to describe intermittent fluctuations in turbulent fluids and plasmas.<sup>17,18</sup>

For a super-position of pulses with fixed shape and constant duration closed form expressions are here derived for the lowest order moments, auto-correlation function and frequency power spectral density in the case of periodic pulse arrivals and a random distribution of pulse amplitudes. In general, the spectrum is a Dirac comb located at multiples of the periodicity time and modulated by the pulse spectrum. Randomness in the pulse arrival times is investigated by numerical realizations of the process and the results are discussed in the context of some well-known chaos models.

The contribution is structured as follows. In Sec. II, a motivating example for studying periodic pulse trains in connection to chaotic motion is presented. In Sec. III the stochastic model for a super-position of pulses is presented and its PSD for general arrival times is derived. In Sec. IV the case of periodic pulse arrivals is analyzed in detail with a particular

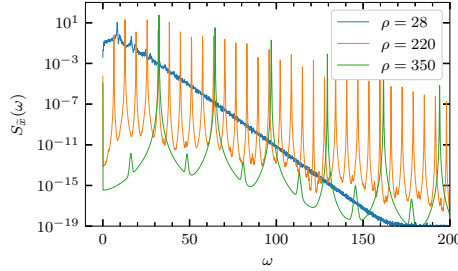


FIG. 1. Power spectral density of the  $x$ -variable in the Lorenz system for  $\sigma = 10$ ,  $\beta = 8/3$  and various values of  $\rho$ .

focus on Lorentzian pulses. Finally, in Sec. VI it is demonstrated that the stochastic model describes the chaotic dynamics of the Lorenz system.

## II. THE LORENZ SYSTEM

A canonical chaos system is given by the Lorenz equations describing weakly non-linear thermal convection in an inversely stratified fluid

$$\frac{dx}{dt} = \sigma(y - x), \quad (1)$$

$$\frac{dy}{dt} = x(\rho - z) - y, \quad (2)$$

$$\frac{dz}{dt} = xy - \beta z. \quad (3)$$

Here  $x$ ,  $y$  and  $z$  are the variables and  $\sigma$ ,  $\rho$  and  $\beta$  are the model parameters. Time series of the  $x$ -variable and the associated frequency PSD are presented in Figs. 2 and 1 for  $\sigma = 10$ ,  $\beta = 8/3$  and three different values of the model parameter  $\rho$ .

For  $\rho = 350$  the solution consists of periodic oscillations and the frequency PSD resemble a Dirac comb with an exponential modulation of the peak amplitudes. As shown in Fig. 2, the oscillations are well described by Lorentzian-shaped pulses. Following a period doubling bifurcation, the solution for  $\rho = 220$  is still regular and the PSD is again dominated by a Dirac-like comb. For  $\rho = 28$  the solution is chaotic and the PSD has an exponential shape for high frequencies and some narrow peaks for low frequencies. In the following, these features of the chaotic dynamics will be analyzed by describing the fluctuations as a super-position

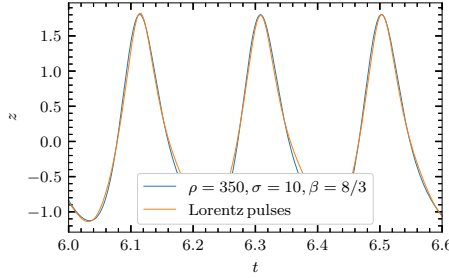


FIG. 2. Excerpt of the time series of the  $z$ -variable in the Lorenz system for  $\sigma = 10$ ,  $\beta = 8/3$  and  $\rho = 350$  compared to a superposition of Lorentz pulses.

of Lorentzian-shaped pulses.

### III. THE POWER SPECTRAL DENSITY OF A SUM OF PULSES

In this section, we develop an expression for the power spectral density of the shot noise process for general arrival times. This is based on the formalism developed for filtered Poisson processes, also called shot noise processes.

We consider a train of  $K(T)$  pulses arriving in the interval  $[0, T]$  with randomly distributed arrival times  $\{t_k\}_{k=1}^{K(T)}$  and randomly distributed amplitudes  $\{A_k\}_{k=1}^{K(T)}$ . The pulses have a characteristic shape  $\varphi$  and a characteristic duration time  $\tau_d$ .

Following these remarks, the process is written as a convolution between a pulse train  $f_K$  and a pulse shape  $\varphi$ :

$$\Phi_K(t) = \int_{-\infty}^{\infty} ds \varphi\left(\frac{t}{\tau_d} - s\right) f_K(s), \quad (4)$$

where

$$f_K(s) = \sum_{k=1}^{K(T)} A_k \delta\left(s - \frac{t_k}{\tau_d}\right) \quad (5)$$

and  $\delta$  denotes the Dirac delta function. This can be viewed as a point process  $f_K$  passed through a filter with response function  $\varphi$ , hence the name. Note that for i.i.d. uniform pulse arrivals,  $K(T)$  is a Poisson process.

We normalize the pulse shape such that

$$\int_{-\infty}^{\infty} |\varphi(s)| ds = 1. \quad (6)$$

We also introduce the notation

$$\rho_\varphi(s) = \frac{1}{I_2} \int_{-\infty}^{\infty} du \varphi(u) \varphi(u + s) \quad (7)$$

and

$$\varrho_\varphi(\theta) = \frac{1}{I_2} |\mathcal{F}[\varphi](\theta)|^2 \quad (8)$$

for the auto-correlation and the power spectral density of the pulse shape, respectively. Here,

$$I_n = \int_{-\infty}^{\infty} \varphi(s)^n ds. \quad (9)$$

Note that the functions  $\rho_\varphi$  and  $\varrho_\varphi$  form a Fourier transform pair, where the definition of the Fourier transform is given in Appendix A. Throughout this contribution, we will use Lorentzian pulses, which are detailed in Appendix D.

To find the PSD, we start from Eq. (4), and take the Fourier transform as defined in Appendix A:

$$\mathcal{F}_T[\Phi_K](\omega) = \int_0^T dt \exp(-i\omega t) \Phi_K(t) = \int_0^T dt \exp(-i\omega t) \int_{-\infty}^{\infty} ds \varphi(s) f_K\left(\frac{t}{\tau_d} - s\right) \quad (10)$$

where we have exchanged the functions in the convolution given by Eq. (4). A change of variables  $u(t) = t - \tau_d s$  gives

$$\mathcal{F}_T[\Phi_K](\omega) = \int_{-\infty}^{\infty} ds \varphi(s) \exp(-i\tau_d \omega s) \int_{-\tau_d s}^{T - \tau_d s} du f_K\left(\frac{u}{\tau_d}\right) \exp(-i\omega u). \quad (11)$$

We assume that  $\varphi(s)$  is negligible after a few  $\tau_d$ . Moreover, since no pulses arrive for negative times,  $f_K(u) = 0$  for  $u < 0$ . Assuming  $T/\tau_d \gg 1$ , we can therefore approximate the limits of the second integral in Eq. (11) as  $u \in [0, T]$ , and the two integrals become independent. This gives

$$\mathcal{F}_T[\Phi_K](\omega) = \mathcal{F}[\varphi](\tau_d \omega) \mathcal{F}_T[f_K](\omega). \quad (12)$$

The power spectral density (PSD) of the stationary process  $\Phi$  is therefore

$$\mathcal{S}_\Phi(\omega) = \lim_{T \rightarrow \infty} \frac{1}{T} \langle |\mathcal{F}_T[\Phi_K](\omega)|^2 \rangle = |\mathcal{F}[\varphi](\tau_d \omega)|^2 \lim_{T \rightarrow \infty} \frac{1}{T} \langle |\mathcal{F}_T[f_K](\omega)|^2 \rangle, \quad (13)$$

where  $\mathcal{S}_\Phi(\omega)$  is independent of  $K$ , since the average is over all random variables. The power spectrum is thus the product of the power spectrum of the pulse shape and the power

spectrum of the point process. Non-uniform arrivals only affect the point process, so this will be isolated in the analysis in Sec. III A.

Using Eq. (8), the full power spectral density of  $\Phi$  can be written as

$$\mathcal{S}_\Phi(\omega) = I_2 \varrho_\varphi(\tau_d \omega) \lim_{T \rightarrow \infty} \frac{1}{T} \langle |\mathcal{F}_T[f_K](\omega)|^2 \rangle. \quad (14)$$

### A. The power spectral density for general arrival times

The Fourier transform of the point process is

$$\mathcal{F}_T[f_K](\omega) = \tau_d \sum_{k=1}^K A_k \exp(-i\omega t_k). \quad (15)$$

Multiplying this expression with its complex conjugate and averaging over all random variables gives (for a general distribution of arrivals  $P_{t_1, t_2, \dots, t_K}(t_1, t_2, \dots, t_K)$ , assuming amplitudes are i.i.d. and independent of the arrival times):

$$\begin{aligned} & \frac{1}{T} \langle |\mathcal{F}_T[f_K](\omega)|^2 \rangle \\ &= \sum_{K=0}^{\infty} P_K(K; T, \tau_w) \frac{\tau_d^2}{T} \sum_{k=1}^K \sum_{l=1}^K \int_{-\infty}^{\infty} dt_1 \cdots \int_{-\infty}^{\infty} dt_K P_{t_1, \dots, t_K}(t_1, \dots, t_K) \\ & \quad \times \int_0^{\infty} dA_1 P_A(A_1) \cdots \int_0^{\infty} dA_K P_A(A_K) A_k A_l \exp(i\omega(t_l - t_k)). \\ &= \sum_{K=0}^{\infty} P_K(K; T, \tau_w) \frac{\tau_d^2}{T} \sum_{k,l=1}^K \langle A_k A_l \rangle \langle \exp(i\omega(t_l - t_k)) \rangle. \end{aligned} \quad (16)$$

In this equation, there are  $K$  terms where  $k = l$  and  $K(K - 1)$  terms where  $k \neq l$ . Summing over all these terms, we have

$$\begin{aligned} \frac{1}{T} \langle |\mathcal{F}_T[f_K](\omega)|^2 \rangle &= \tau_d^2 \sum_{K=0}^{\infty} P_K(K; T, \tau_w) \\ & \quad \left\{ \frac{K}{T} \langle A^2 \rangle + \frac{1}{T} \langle A \rangle^2 \sum_{k=1}^K \sum_{l \neq k} \langle \exp(i\omega(t_l - t_k)) \rangle \right\}. \end{aligned} \quad (17)$$

The average inside the exponential sum is the joint characteristic function of  $t_l$  and  $t_k$ . Exchanging the order of  $k$  and  $l$  in the double sum is the same as taking the complex

conjugate of this characteristic function, so we get

$$\begin{aligned} \frac{1}{T} \langle |\mathcal{F}_T[f_K](\omega)|^2 \rangle &= \frac{\tau_d^2 \langle K \rangle}{T} \langle A^2 \rangle + \\ &\quad \frac{\tau_d^2}{T} \langle A \rangle^2 \sum_{K=0}^{\infty} P_K(K; T, \tau_w) \sum_{k=2}^K \sum_{l=1}^{k-1} 2\text{Re}[\langle \exp(i\omega(t_l - t_k)) \rangle]. \end{aligned} \quad (18)$$

### 1. Uniformly distributed i.i.d arrivals

As an example, we show that the expression in Eq. (18) is consistent with the established result for  $K(T)$  a pure Poisson point process.

Now  $t_l, t_k$  are i.i.d. uniformly distributed arrivals on  $[0, T]$ . We therefore have that

$$\langle \exp(i\omega(t_l - t_k)) \rangle = \langle \exp(i\omega t_l) \rangle \langle \exp(-i\omega t_k) \rangle = 2 \frac{1 - \cos(\omega T)}{\omega^2 T^2}. \quad (19)$$

All terms in the double sum are equal, and we get

$$\frac{1}{T} \langle |\mathcal{F}_T[f_K](\omega)|^2 \rangle = \frac{\tau_d^2 \langle K \rangle}{T} \langle A^2 \rangle + 2 \frac{\tau_d^2}{T} \langle A \rangle^2 \langle K(K-1) \rangle \frac{1 - \cos(\omega T)}{\omega^2 T^2}. \quad (20)$$

In this case,  $K$  is Poisson distributed with mean and variance equal to  $T/\tau_w$  and we get

$$\frac{1}{T} \langle |\mathcal{F}_T[f_K](\omega)|^2 \rangle = \frac{\tau_d^2}{\tau_w} \langle A^2 \rangle + \frac{2\tau_d^2}{\tau_w^2} \langle A \rangle^2 \frac{1 - \cos(\omega T)}{\omega^2 T^2}, \quad (21)$$

which gives, using  $\gamma = \tau_d/\tau_w$ ,

$$\lim_{T \rightarrow \infty} \frac{1}{T} \langle |\mathcal{F}_T[f_K](\omega)|^2 \rangle = \tau_d \gamma \langle A^2 \rangle + 2\pi \tau_d \gamma^2 \langle A \rangle^2 \delta(\tau_d \omega), \quad (22)$$

which is the standard expression for the Poisson process.<sup>39</sup> Identifying the last term as containing a Dirac delta in the limit  $T \rightarrow \infty$  makes sense in the theory of distributions<sup>46</sup>. A Poisson process gives a flat spectrum, so the only frequency variation in the full spectrum will be due to the pulse function.

### 2. Periodic arrival times

We consider the situation where the periodicity is known, but the exact arrivals are not. This corresponds to uncertainty in where the measurement starts in relation to the first arrival time. If the arrivals are periodic, the marginal PDF of arrival  $k$  given that the starting time is  $s$ , is

$$P_{t_k|s}(t_k|s) = \delta(t_k - \tau_p k - s). \quad (23)$$

Since each arrival is deterministic, the joint PDF with known starting point is the product of the marginal PDFs, and we have

$$\langle \exp(i\omega(t_l - t_k)) \rangle = \exp(i\omega\tau_p(l - k)). \quad (24)$$

Note that this is independent of  $s$  for all starting points, so for now we need not consider  $s$  further. We have from Eq. (18)

$$\begin{aligned} \sum_{k=2}^K \sum_{l=1}^{k-1} 2\text{Re}[\langle \exp(i\omega(t_l - t_k)) \rangle] &= \sum_{k=2}^K \sum_{l=1}^{k-1} 2 \cos(\tau_p\omega(l - k)) \\ &= \frac{K - 1 + \cos(\tau_p\omega K) - K \cos(\tau_p\omega)}{\cos(\tau_p\omega) - 1} = \frac{\cos(\tau_p\omega K) - 1}{\cos(\tau_p\omega) - 1} - K. \end{aligned} \quad (25)$$

Due to the periodicity, there are  $\lfloor T/\tau_p \rfloor$  events in a time series of length  $T$ . We use  $P_K(K; T, \tau_p) = \delta(K - \lfloor T/\tau_p \rfloor)$ . Inserting this and Eq. (25) into Eq. (18) gives

$$\frac{1}{T} \langle |\mathcal{F}_T[f_K](\omega)|^2 \rangle = \frac{\tau_d^2}{T} \lfloor T/\tau_p \rfloor \langle A^2 \rangle + \frac{\tau_d^2}{T} \lfloor T/\tau_p \rfloor \langle A \rangle^2 \left[ \lfloor T/\tau_p \rfloor^{-1} \frac{\cos(\tau_p\omega \lfloor T/\tau_p \rfloor) - 1}{\cos(\tau_p\omega) - 1} - 1 \right]. \quad (26)$$

For  $T/\tau_p \gg 1$ ,  $\lfloor T/\tau_p \rfloor/T \approx 1/\tau_p$ , and we have (writing  $K = \lfloor T/\tau_p \rfloor$ )

$$\lim_{K \rightarrow \infty} \frac{1}{T} \langle |\mathcal{F}_T[f_K](\omega)|^2 \rangle = \frac{\tau_d^2}{\tau_p} \langle A^2 \rangle - \frac{\tau_d^2}{\tau_p} \langle A \rangle^2 + \frac{\tau_d^2}{\tau_p} \langle A \rangle^2 \lim_{K \rightarrow \infty} \frac{1}{K} \frac{\cos(\tau_p\omega K) - 1}{\cos(\tau_p\omega) - 1}. \quad (27)$$

Let us consider the last part of the last term,

$$\lim_{K \rightarrow \infty} \frac{1}{K} \frac{\cos(\tau_p\omega K) - 1}{\cos(\tau_p\omega) - 1}. \quad (28)$$

For integer  $n$  and  $\tau_p\omega \neq 2\pi n$ , this limit is zero. For  $\tau_p\omega \rightarrow 2\pi n$ , this limit tends to  $\infty$ . We might therefore consider Eq. (28) proportional to a train of  $\delta$ -pulses located at  $\tau_p\omega = 2\pi n$ .

Setting  $\tau_p\omega = 2\pi n + \epsilon$  where  $\epsilon \ll 1$  and expanding the cosine in the denominator, we have

$$\lim_{K \rightarrow \infty} \frac{1}{K} \frac{\cos(\tau_p\omega K) - 1}{\cos(\tau_p\omega) - 1} \approx \lim_{K \rightarrow \infty} \frac{2}{K} \frac{1 - \cos(\epsilon K)}{\epsilon^2}. \quad (29)$$

This is on the same form as we had when deriving Eq. (22), so we conclude that

$$\lim_{K \rightarrow \infty} \frac{1}{K} \frac{\cos(\tau_p\omega K) - 1}{\cos(\tau_p\omega) - 1} \sim 2\pi \sum_{n=-\infty}^{\infty} \delta(\tau_p\omega - 2\pi n). \quad (30)$$

Inserting this into Eq. (26) gives the full expression for the PSD of a train of delta pulses with randomly distributed amplitudes:

$$\lim_{T \rightarrow \infty} \frac{1}{T} \langle |\mathcal{F}_T[f_K](\omega)|^2 \rangle = \tau_d \gamma A_{\text{rms}}^2 + 2\pi \tau_d \gamma^2 \langle A \rangle^2 \sum_{n=-\infty}^{\infty} \delta(\tau_d\omega - 2\pi n\gamma). \quad (31)$$

This equation will be discussed in the following section.

## IV. THE SHOT NOISE PROCESS WITH PERIODIC ARRIVALS

The full power spectral density of  $\Phi$  is given by multiplying Eq. (31) by the power spectrum of the pulse functions, Eq. (8), as given by Eq. (14):

$$\mathcal{S}_\Phi(\omega) = \tau_d \gamma A_{\text{rms}}^2 I_2 \varrho_\varphi(\tau_d \omega) + 2\pi \tau_d \gamma^2 \langle A \rangle^2 I_2 \varrho_\varphi(\tau_d \omega) \sum_{n=-\infty}^{\infty} \delta(\tau_d \omega - 2\pi n \gamma). \quad (32)$$

There are two main differences from the uniformly distributed pulses, given by Eq. (22):  $A_{\text{rms}}$  enters into the first term instead of  $\langle A^2 \rangle$ , and there is a contribution of delta spikes at integer multiples of  $2\pi/\tau_p$ , with an envelope given by the pulse shape. We may view the first term as the average spectrum, due to the randomness of the amplitude distribution, while the second term containing the sum of delta pulses is due to the periodicity of the pulse arrivals. Accordingly, the first term vanishes for degenerately distributed amplitudes,  $p_A(A) = \delta(A - \langle A \rangle)$ . For a symmetric amplitude distribution around 0,  $\langle A \rangle = 0$  and  $A_{\text{rms}}^2 = \langle A^2 \rangle$ . The periodicity is canceled out and only the first term remains.

In Fig. 3, the power spectral density of a synthetically generated shot noise is presented for exponentially distributed amplitudes (blue line) and symmetrically Laplace distributed amplitudes (orange line). The arrivals are periodic and the pulses have a Lorentzian shape. The analytic expression Eq. (32) for both cases is given by the black and green dashed lines respectively. The Dirac comb with decaying amplitudes is easily seen in the case with exponential amplitudes. We emphasize that the main effect of the periodicity, the Dirac comb, is completely cancelled out by the symmetrically distributed pulse amplitudes.

### A. The correlation function

By the Wiener-Khinchin theorem,

$$R_\Phi(t) = \frac{1}{2\pi} \int_{-\infty}^{\infty} d\omega \mathcal{S}_\Phi(\omega) \exp(i\omega t) \quad (33)$$

$$= \gamma A_{\text{rms}}^2 I_2 \rho_\varphi(t/\tau_d) + \gamma^2 \langle A \rangle^2 I_2 \sum_{n=-\infty}^{\infty} \varrho_\varphi(2\pi n \gamma) \exp(i2\pi n \gamma t/\tau_d). \quad (34)$$

By using the Poisson summation formula and properties of the Fourier transform as detailed in Appendix C, we can write  $R_\Phi$  as

$$R_\Phi(t) = \gamma A_{\text{rms}}^2 I_2 \rho_\varphi\left(\frac{t}{\tau_d}\right) + \gamma \langle A \rangle^2 I_2 \sum_{m=-\infty}^{\infty} \rho_\varphi\left(\frac{m}{\gamma} + \frac{t}{\tau_d}\right). \quad (35)$$

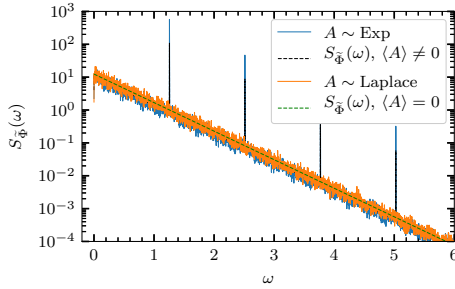


FIG. 3. The power spectral density of a shot noise process with periodic arrival times for exponentially (blue) and Laplace (orange) distributed amplitudes. The analytic expression is given by the black and green dashed lines, respectively.

Writing  $m/\gamma + t/\tau_d = (m + t/\tau_p)/\gamma$ , we see that the correlation function consists of a central peak with followed by periodic modulations at integer multiples of  $\tau_p$ . Again, for degenerate amplitudes the correlation function only consists of the periodic train: there is no randomness left in the signal and so the correlation function does not decay for large times. For symmetric amplitudes, only the central peak remains.

In Fig. 4, the auto-correlation function of a synthetically generated shot noise is presented for exponentially distributed amplitudes (blue line) and symmetrically Laplace distributed amplitudes (orange line). The arrivals are periodic and the pulses have a Lorentzian shape. The analytic expression Eq. (32) for both cases is given by the black and green dashed lines respectively. For exponentially distributed amplitudes, the periodicity is clearly seen. This effect is again completely cancelled out by symmetrically distributed amplitudes.

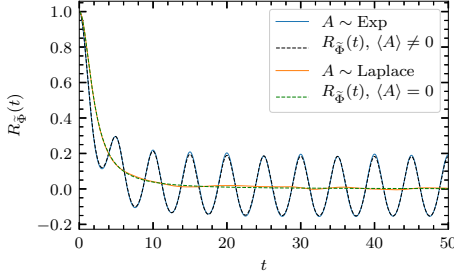


FIG. 4. The auto-correlation function of a shot noise process with periodic arrival times for exponentially (blue) and Laplace (orange) distributed amplitudes. The analytic expression is given by the black and green dashed lines, respectively.

## B. The mean value and standard deviation

The mean value of the shot noise process with periodic pulses, assuming a uniform starting time distribution in  $[0, \tau_p]$ , is given by

$$\begin{aligned}
\langle \Phi_K \rangle &= \sum_{k=1}^K \int dA P_A(A) \int ds P_s(s) A \varphi\left(\frac{t - \tau_p k - s}{\tau_d}\right) \\
&= \frac{\langle A \rangle}{\tau_p} \sum_{k=1}^K \int_0^{\tau_p} ds \varphi\left(\frac{t - \tau_p k - s}{\tau_d}\right) \\
&= \frac{\langle A \rangle}{\tau_p} \sum_{k=1}^K \int_{(t-\tau_p(k+1))/\tau_d}^{(t-\tau_p k)/\tau_d} \tau_d du \varphi(u) = \gamma \langle A \rangle \int_{(t-(K+1)\tau_p)/\tau_d}^{(t-\tau_p)/\tau_d} du \varphi(u) \\
\langle \Phi \rangle &= \lim_{T \rightarrow \infty} \sum_{K=1}^{\infty} p_K(K; \tau_w, T) \langle \Phi_K \rangle = \gamma \langle A \rangle I_1.
\end{aligned} \tag{36}$$

In the last step, we let  $T \rightarrow \infty$  giving  $K \rightarrow \infty$  and set the upper integration limit to  $\infty$  to avoid the effect due to the signal starting at  $t = 0$ . This is the expected result from Campbell's theorem. This is also consistent with the fact that the square mean value is given by the zero-frequency delta function in the power spectrum,  $\mathcal{S}_\Phi(\omega) = 2\pi \langle \Phi \rangle^2 \delta(\omega) + \dots$ .

The second moment is most conveniently found by noting that

$$\langle \Phi \rangle^2 = \langle \Phi(t) \Phi(t) \rangle = R_\Phi(0) = \gamma A_{\text{rms}}^2 I_2 + \gamma \langle A \rangle^2 I_2 \sum_{m=-\infty}^{\infty} \rho_\varphi\left(\frac{m}{\gamma}\right), \tag{37}$$

where we have used that  $\rho_\varphi(0) = 1$ . This can be verified by calculating the second moment directly as was done for the first. In Appendix B, it is shown that this is also equivalent to an extention of Campbell's theorem. We get the variance

$$\Phi_{\text{rms}}^2 = \gamma A_{\text{rms}}^2 I_2 + \gamma \langle A \rangle^2 I_2 \left( \sum_{m=-\infty}^{\infty} \rho_\varphi(m/\gamma) - \gamma \frac{I_1^2}{I_2} \right). \quad (38)$$

In the case  $\gamma \ll 1$ , only the  $m = 0$  term in the sum gives a contribution,  $\rho_\varphi(0) = 1$ , giving

$$\lim_{\gamma \rightarrow 0} \Phi_{\text{rms}}^2 = \gamma \langle A^2 \rangle I_2, \quad (39)$$

where we neglect the  $\gamma^2$ -contribution of the last term in the bracket. Thus, in the limit of no pulse overlap, the variance for the case of periodic pulses is equivalent to the case of Poisson distributed pulses.

In the case  $\gamma \gg 1$ , we can write  $m/\gamma = m\Delta_t \rightarrow t$  and treat the sum as an integral,  $\gamma \sum_m \rho(m/\gamma)(1/\gamma) \approx \gamma \int \rho(t)\Delta_t = \gamma I_1^2/I_2$ , where the sum is over all integers and the integral is over all reals. The terms inside the bracket cancel, and we get

$$\lim_{\gamma \rightarrow \infty} \Phi_{\text{rms}}^2 = \gamma A_{\text{rms}}^2 I_2. \quad (40)$$

Since  $A_{\text{rms}}^2 = \langle A^2 \rangle - \langle A \rangle^2 \leq \langle A^2 \rangle$ , the periodic pulse overlap gives lower variance than the Poisson distributed pulses as there is less randomness in the signal. For exponential amplitudes, the variance in the periodic case is a factor 2 smaller. For amplitudes with zero mean value, it is equal to the Poisson case while for fixed amplitudes, the signal has no variance as pulses will accumulate until the rate of accumulation exactly matches the rate of decay, after which the signal will remain constant.

### C. Quasi-periodic pulses

In this section, we present the effect of quasi-periodicity in the arrival time distribution on the second-order statistics of the shot noise process. Here, we model quasi-periodicity using a uniform distribution for each arrival around the periodic arrival time, so that the distribution of the  $k$ 'th arrival time given the starting time  $s$  is

$$P_{t_k}(t_k|s) = \begin{cases} \frac{1}{2\tau_p \kappa}, & -\tau_p \kappa \leq t_k - \tau_p k - s \leq \tau_p \kappa \\ 0, & \text{else} \end{cases}. \quad (41)$$

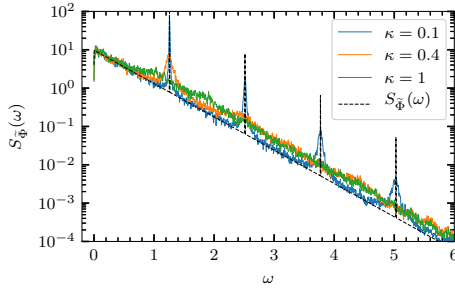


FIG. 5. The power spectral density of a shot noise process with quasi-periodic arrival times for different values of the  $\kappa$ -parameter. The analytic expression for purely periodic pulses is given by the black dashed line.

In the limit  $\kappa \rightarrow 0$ , we recover the periodic arrivals, while for  $\kappa > 1$ , the probability distributions of adjacent arrivals overlap. We emphasize that this is still a very restrictive formulation: even for  $\kappa > 1$ , each arrival is guaranteed to be centered on the time corresponding to the periodic arrival time, and the number of arrivals in a given interval is fixed up to end effects.

In Figs. 5 and 6, the effect of this quasi-periodicity is presented. The full lines give the power spectral densities and the auto-correlation functions of the shot noise process with quasi-periodic arrival times for different values of the  $\kappa$ -parameter, Lorentzian pulses and exponentially distributed amplitudes. The black dashed line gives the analytic prediction for purely periodic pulses. Even moderate deviations from pure periodicity quickly destroy the Dirac comb. For  $\kappa = 1$ , the spectrum and correlation function are already difficult to distinguish from the case of Poisson distributed arrivals. Thus, quasi-periodic phenomena in for example turbulent fluids cannot be expected to produce more than the first peak of the Dirac comb.

## V. MULTIPLE PERIODICITIES: ROUTE TO CHAOS

We now consider a situation where we have multiple periodicities, each with their own amplitudes and possible offsets, such that we can write the Fourier transform of the point

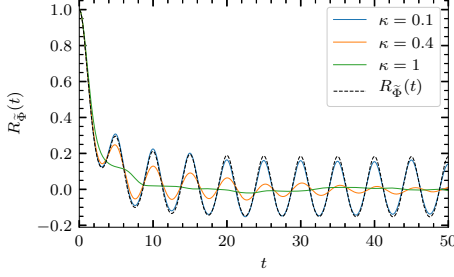


FIG. 6. The auto-correlation function of a shot noise process with quasi-periodic arrival times for different values of the  $\kappa$ -parameter. The analytic expression for purely periodic pulses is given by the black dashed line.

process as

$$\mathcal{F}_T[f_K](\omega) = \tau_d \sum_{p=1}^P \sum_{k=1}^{K^p} A_k^p \exp(-i\omega[\tau^p k + \alpha^p]), \quad (42)$$

where  $\tau^p$  are the periods,  $\{A_k^p\}_{k=1}^{K^p}$  are the arrivals connected to the  $p$ 'th periodicity,  $\alpha^p$  are constant offsets for the first arrivals and  $K^p = \lfloor (T - \alpha^p)/\tau^p \rfloor$ . We assume that arrivals for different periodicities are independent. Further, we arrange the periods in decreasing order,  $\tau^1 \geq \tau^2 \geq \tau^3 \geq \dots$ . For large enough  $T$  that the offsets can be neglected, this leads to an increasing order in the number of events,  $K^1 \leq K^2 \leq K^3 \leq \dots$ . We get

$$\begin{aligned} & |\mathcal{F}_T[f_K](\omega)|^2 \\ &= \tau_d^2 \sum_{p,q=1}^P \sum_{k=1}^{K^p} \sum_{l=1}^{K^q} A_k^p A_l^q \exp(-i\omega[\tau^p k - \tau^q l + \alpha^p - \alpha^q]) \\ &= \tau_d^2 \sum_{p=1}^P \sum_{k=1}^{K^p} (A_k^p)^2 \\ &+ \tau_d^2 \sum_{p=1}^P \sum_{\substack{k,l=1 \\ k \neq l}}^{K^p} A_k^p A_l^p \exp(-i\omega\tau^p[k - l]) \\ &+ \tau_d^2 \sum_{\substack{p,q=1 \\ p \neq q}}^P \sum_{k=1}^{K^p} \sum_{l=1}^{K^q} A_k^p A_l^q \exp(-i\omega[\tau^p k - \tau^q l + \alpha^p - \alpha^q]). \end{aligned}$$

Taking the average over all amplitudes and gathering terms  $(k, l) + (l, k)$  in the second double sum as well as terms  $(p, q) + (q, p)$  in the triple sum, we get

$$\begin{aligned} & \frac{1}{T} \langle |\mathcal{F}_T[f_K](\omega)^2| \rangle \\ &= \frac{\tau_d^2}{T} \sum_{p=1}^P K^p \langle (A^p)^2 \rangle + \frac{\tau_d^2}{T} \sum_{p=1}^P \sum_{k=2}^{K^p} \sum_{l=1}^{k-1} \langle A^p \rangle^2 2 \cos(\omega \tau^p [k - l]) \\ & \quad + \frac{\tau_d^2}{T} \sum_{p=2}^P \sum_{q=1}^{p-1} \sum_{k=1}^{K^p} \sum_{l=1}^{K^q} 2 \langle A^p \rangle \langle A^q \rangle \\ & \quad \exp\left(i\omega \frac{(k-l)(\tau^p + \tau^q)}{2}\right) \cos\left(\omega \frac{(k+l)(\tau^p - \tau^q)}{2} + \omega(\alpha^p - \alpha^q)\right). \end{aligned}$$

The first two terms just gives a sum of the result in (31) over all periods. To investigate the last term, we consider the special case where  $\tau^p = \tau \forall p$  so  $K^p = K \forall p$ . Then we have that the last term is

$$\begin{aligned} & \frac{\tau_d^2}{T} \sum_{p=2}^P \sum_{q=1}^{p-1} \langle A^p \rangle \langle A^q \rangle 2 \cos(\omega(\alpha^p - \alpha^q)) \sum_{k=1}^K \sum_{l=1}^K \exp(i\omega\tau(k - l)) \\ &= \frac{\tau_d^2}{T} \sum_{p=2}^P \sum_{q=1}^{p-1} \langle A^p \rangle \langle A^q \rangle 2 \cos(\omega(\alpha^p - \alpha^q)) \frac{\cos(K\omega\tau) - 1}{\cos(\omega\tau) - 1}. \quad (43) \end{aligned}$$

This contains exactly the expression found in Eq. (29), so we have that

$$\begin{aligned} & \lim_{T \rightarrow \infty} \frac{1}{T} \langle |\mathcal{F}_T[f_K](\omega)^2| \rangle \\ &= \sum_{p=1}^P \left\{ \tau_d \gamma (A_{\text{rms}}^p)^2 + 2\pi \tau_d \gamma^2 \langle A^p \rangle^2 \sum_{n=-\infty}^{\infty} \delta(\tau_d \omega - 2\pi n \gamma) \right\} \\ & \quad + \sum_{p=2}^P \sum_{q=1}^{p-1} \langle A^p \rangle \langle A^q \rangle 2 \cos(\omega(\alpha^p - \alpha^q)) 2\pi \tau_d \gamma \sum_{n=-\infty}^{\infty} \delta(\tau \omega - 2\pi n). \end{aligned} \quad (44)$$

Here,  $\gamma = \tau_d/\tau$ . Seeing that we can exchange  $2\sum_{p=2}^P \sum_{q=1}^{p-1}$  with  $\sum_{p=1}^P \sum_{q=1, q \neq p}^P$ , we can write the full expression as

$$\begin{aligned} \lim_{T \rightarrow \infty} \frac{1}{T} \langle |\mathcal{F}_T[f_K](\omega)|^2 \rangle &= \sum_{p=1}^P \tau_d \gamma (A_{\text{rms}}^p)^2 + \\ &\quad \sum_{p=1}^P 2\pi \tau_d \gamma^2 \langle A^p \rangle \left[ \langle A^p \rangle + \sum_{q \neq p} \langle A^q \rangle \cos(\omega(\alpha^p - \alpha^q)) \right] \sum_{n=-\infty}^{\infty} \delta(\tau_d \omega - 2\pi n \gamma) \\ &= \sum_{p=1}^P \tau_d \gamma (A_{\text{rms}}^p)^2 + 2\pi \tau_d \gamma^2 \sum_{p=1}^P \sum_{q=1}^P \langle A^p \rangle \langle A^q \rangle \cos(\omega(\alpha^p - \alpha^q)) \sum_{n=-\infty}^{\infty} \delta(\tau_d \omega - 2\pi n \gamma). \quad (45) \end{aligned}$$

Thus, we get the same expression as for only one periodicity, except that we make the replacements

$$\begin{aligned} A_{\text{rms}}^2 &\rightarrow \sum_{p=1}^P (A_{\text{rms}}^p)^2, \\ \langle A \rangle^2 &\rightarrow \sum_{p=1}^P \sum_{q=1}^P \langle A^p \rangle \langle A^q \rangle \cos(\omega(\alpha^p - \alpha^q)). \end{aligned}$$

In this case, the correction to the second term in the expression for the PSD depends on the offset between the different pulse trains. In particular, if there is no offset,  $\alpha^p - \alpha^q = 0$ , we just get the double sum over all mean values of the amplitudes. In this model, this means that adding further pulses with the same periodicity does not affect the density of the spikes in the Dirac comb. As period doubling can be seen as both decreasing  $\tau_p$  and adding more pulses, this result shows that only decreasing  $\tau_p$  affects the density of the Dirac comb.

## VI. APPLICATION TO THE LORENZ ATTRACTOR

The predictions for the PSD of the stochastic model can be compared to that from numerical simulations of Lorenz system. In Fig. 7 the low-frequency part of the spectrum is presented for  $\rho = 350$  as well as the predicted Dirac comb for a super-position of Lorentzian pulses with duration  $\tau_d = 0.039$  and periodicity  $\tau_p = 0.194$ . This is clearly a good description of the oscillations in the Lorenz system.

In the chaotic state for  $\rho = 28$  the PSD presented in Fig. 8 has some low-frequency peaks with higher harmonics on top of a exponential spectrum. This spectrum can be reproduced by a super-position of quasi-periodic Lorentzian with duation  $\tau_d = 0.135$ , periodicity  $\tau_p =$

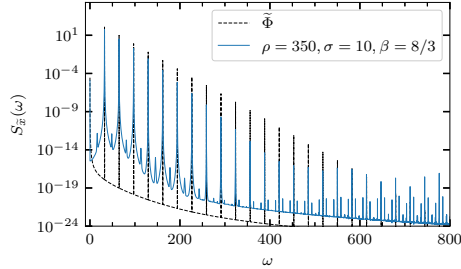


FIG. 7. The power spectral density of a Lorenz system with  $\rho = 350$ ,  $\sigma = 10$  and  $\beta = 8/3$  compared to the frequency power spectral density of a synthetic shot noise process with periodic arrival times and exponentially distributed amplitudes.

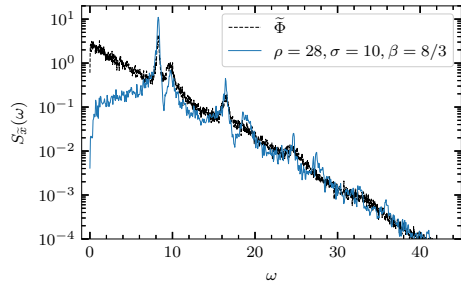


FIG. 8. The power spectral density of a Lorenz system with  $\rho = 28$ ,  $\sigma = 10$  and  $\beta = 8/3$  compared to the power spectral density of a synthetic shot noise process with quasi-periodic arrival times, exponentially distributed amplitudes and  $\kappa = 0.1$ .

0.643 and  $\kappa = 0.1$  for the distribution of pulse arrivals. This is an excellent description of the PSD for the Lorenz system except for the very lowest frequencies which is likely due to the chaotic nature of the fluctuations.

## VII. ACKNOWLEDGEMENTS

This work was supported by the UiT Aurora Centre Program, UiT The Arctic University of Norway (2020) and the Tromsø Research Foundation under grant number 19\_SG\_AT. Discussions with M. Rypdal and M. Overholt are gratefully acknowledged.

## Appendix A: Definitions of the Fourier transform and the Power spectral density

The PSD of a random process  $\Phi(t)$  is defined as

$$\mathcal{S}_\Phi(\omega) = \lim_{T \rightarrow \infty} \frac{1}{T} \langle |\mathcal{F}_T[\Phi](\omega)|^2 \rangle, \quad (\text{A1})$$

where

$$\mathcal{F}_T[\Phi_K](\omega) = \int_0^T dt \exp(-i\omega t) \Phi(t) \quad (\text{A2})$$

is the Fourier transform of the random variable over the domain  $[0, T]$ .

Analytical functions which fall rapidly enough to zero (such as the pulse function) have the Fourier transform

$$\mathcal{F}[\varphi](\theta) = \int_{-\infty}^{\infty} ds \varphi(s) \exp(-i\theta s) \quad (\text{A3})$$

and the inverse transform

$$\varphi(s) = \mathcal{F}^{-1}[\mathcal{F}[\varphi](\theta)](s) = \frac{1}{2\pi} \int_{-\infty}^{\infty} d\theta \exp(i\theta s) \mathcal{F}[\varphi](\theta). \quad (\text{A4})$$

Note that here,  $\theta$  and  $s$  are non-dimensional variables, as opposed to  $t$  and  $\omega$ .

## Appendix B: The extended Campbell's theorem

For a full discussion of Campbell's theorem for the mean value of a shot noise process as well as various extentions, we refer to [Rice, Campbell, Pecseli]. It can be shown that for i.i.d. waiting times  $W$  with distribution  $p_W$  and mean value  $\tau_w$ , we have in our notation

$$\begin{aligned} \langle \Phi^2 \rangle &= \gamma \langle A^2 \rangle I_2 + \\ &2\gamma \langle A \rangle^2 I_2 \sum_{k=1}^{\infty} \int_0^{\infty} ds_1 \int_0^{\infty} ds_2 \cdots \int_0^{\infty} ds_k p_W(s_1) p_W(s_2) \cdots p_W(s_k) \rho_\varphi \left( \frac{1}{\tau_d} \sum_{n=1}^k s_n \right). \end{aligned} \quad (\text{B1})$$

The  $k$ 'th order integral can be compactly written as  $\langle \rho_\phi(S_k/\tau_d) \rangle$ , where  $S_k = \sum_{n=1}^k s_n$ . All  $s_n$  are i.i.d., with distribution  $p_W$ , and we denote the corresponding characteristic function as  $C_W$ . We get

$$\left\langle \rho_\varphi \left( \frac{1}{\tau_d} S_k \right) \right\rangle = \int_{-\infty}^{\infty} dS p_S(S; k) \rho_\varphi \left( \frac{1}{\tau_d} S \right) = \frac{1}{2\pi} \int_{-\infty}^{\infty} du \int_{-\infty}^{\infty} dS C_S(u; k) \exp(-iSu) \rho_\varphi \left( \frac{1}{\tau_d} S \right). \quad (\text{B2})$$

As  $C_S$  is the characteristic function of the sum of  $k$  i.i.d. random variables, we get  $C_S(u; k) = C_W(u)^k$ . Further, we see that this equation contains the Fourier transform of  $\rho_\varphi$ , so we have

$$\left\langle \rho_\varphi\left(\frac{1}{\tau_d}S_k\right) \right\rangle = \frac{\tau_d}{2\pi} \int_{-\infty}^{\infty} du C_W(u)^k \rho_\varphi(\tau_d u), \quad (\text{B3})$$

which gives

$$\langle \Phi^2 \rangle = \gamma \langle A^2 \rangle I_2 + 2\gamma \langle A \rangle^2 I_2 \sum_{k=1}^{\infty} \frac{\tau_d}{2\pi} \int_{-\infty}^{\infty} du C_W(u)^k \rho_\varphi(\tau_d u). \quad (\text{B4})$$

Note that in this equation, only  $C_W^k$  depends on  $k$ , so we may take the sum over  $k$  into the integral and investigate  $\sum_k$ . For periodic arrivals,  $p_W(w) = \delta(w - \tau_w)$ , giving  $C_W(u) = \exp(iu\tau_w)$ , and we get

$$\langle \Phi^2 \rangle = \gamma \langle A^2 \rangle I_2 + 2\gamma \langle A \rangle^2 I_2 \sum_{k=1}^{\infty} \rho_\varphi\left(\frac{1}{\tau_d}k\tau_w\right). \quad (\text{B5})$$

As  $A_{\text{rms}}^2 I_2 = \langle A^2 \rangle I_2 - \langle A \rangle^2 I_2 = \langle A^2 \rangle I_2 - \langle A \rangle^2 I_2 \rho_\varphi(0)$  and  $\rho_\varphi(s) = \rho_\varphi(-s)$ , this is equivalent to Eq. (37).

## Appendix C: The Poisson summation formula

Here, we briefly present the well-known Poisson summation formula, which is treated in a number of textbooks<sup>42–45</sup>. For our purposes, the formulation used in Corollary VII.2.6 in<sup>45</sup> is the most useful. The statement in the book is for functions on general Euclidian spaces, but we repeat it here only for our special case (the real line):

**The Poisson summation formula** Suppose the Fourier transform of  $f$  and its inverse are defined as in Eq. (A3) and Eq. (A4) respectively. Further suppose that  $|f(s)| \leq A(1 + |s|)^{-1-\delta}$  and  $|\mathcal{F}[f](\theta)| \leq A(1 + |\theta|/2\pi)^{-1-\delta}$  with  $A > 0$  and  $\delta > 0$ . Then

$$\sum_{m=-\infty}^{\infty} f(m) = \sum_{n=-\infty}^{\infty} \mathcal{F}[f](2\pi n), \quad (\text{C1})$$

where both series converge absolutely.

- Note that the inequality conditions guarantee that both  $|f(s)|$  and  $|\mathcal{F}[f](\theta)|$  are integrable, which again guarantees that both  $f$  and its Fourier transform are continuous and vanish at  $\infty$  (Theorem I.1.2 in<sup>45</sup>).

- Using properties of the Fourier transform, the summation formula can be cast to a number of different forms:

$$\sum_{n=-\infty}^{\infty} \mathcal{F}[f](2\pi n) = \sum_{m=-\infty}^{\infty} f(m) \quad (\text{C2})$$

$$\sum_{n=-\infty}^{\infty} \gamma \mathcal{F}[f](2\pi n\gamma) = \sum_{m=-\infty}^{\infty} f(m/\gamma) \quad (\text{C3})$$

$$\sum_{n=-\infty}^{\infty} \gamma \mathcal{F}[f](2\pi n\gamma) \exp(i2\pi n\gamma t/\tau_d) = \sum_{m=-\infty}^{\infty} f(m/\gamma + t/\tau_d). \quad (\text{C4})$$

- By using the definitions of  $\rho$  and  $\varrho$  given in Eq. (7) and Eq. (8) respectively, as well as the Fourier transform, we have that if Eq. (C1) holds for  $\varphi$ , then by Eq. (C4) we have

$$\begin{aligned} \sum_{m=-\infty}^{\infty} \varphi(m+s) &= \sum_{n=-\infty}^{\infty} \mathcal{F}[\varphi](2\pi n) \exp(i2\pi ns), \\ \int_{-\infty}^{\infty} du \varphi(u) \sum_{m=-\infty}^{\infty} \varphi(s+m) &= \int_{-\infty}^{\infty} du \varphi(u) \sum_{m=-\infty}^{\infty} \mathcal{F}[\varphi](2\pi n) \exp(i2\pi ns), \\ \sum_{m=-\infty}^{\infty} \rho_{\varphi}(m) &= \sum_{n=-\infty}^{\infty} \varrho_{\varphi}(2\pi n), \end{aligned}$$

which means that the summation formula holds for the correlation function and power spectrum of the pulse as well. This does not necessarily work in reverse - if one of the sums over  $\varphi$  or its Fourier transform diverges, we cannot exchange the summation and the integral in the second step. Consider as an example the one-sided exponential pulse (detailed in Appendix E). Here, the pulse function does not fulfill the Poisson summation formula as the Fourier transform goes as  $\theta^{-1}$ , and so the sum diverges. Its correlation function and power spectrum do, however, fulfill the conditions and therefore the formula.

## Appendix D: The Lorentz pulse

The Lorentz pulse is given by

$$\varphi(s) = (1 + s^2)^{-1}/\pi. \quad (\text{D1})$$

Its Fourier transform is

$$\mathcal{F}[\varphi](\theta) = \exp(-|\theta|), \quad (\text{D2})$$

the integrals are  $I_n =$ , and we have the correlation function

$$\rho_\varphi(s) = 4(4+s^2)^{-1}, \quad (\text{D3})$$

and spectrum

$$\varrho_\varphi(\theta) = 2\pi \exp(-2|\theta|). \quad (\text{D4})$$

In general, the full sum of the correlation function is given by

$$\sum_{m=-\infty}^{\infty} \rho_\varphi\left(\frac{m}{\gamma} + \frac{t}{\tau_d}\right) = \gamma\pi[\coth(2\gamma\pi - i\gamma\pi t/\tau_d) + \coth(2\gamma\pi + i\gamma\pi t/\tau_d)]. \quad (\text{D5})$$

Two special cases of this are of interest in the current contribution. For  $t = 0$ , we get

$$\sum_{m=-\infty}^{\infty} \rho_\varphi\left(\frac{m}{\gamma}\right) = 2\gamma\pi \coth(2\gamma\pi), \quad (\text{D6})$$

while in the limit  $\gamma \rightarrow 0$  we get the expected result

$$\lim_{\gamma \rightarrow 0} \sum_{m=-\infty}^{\infty} \rho_\varphi\left(\frac{m}{\gamma} + \frac{t}{\tau_d}\right) = \rho_\varphi(t/\tau_d). \quad (\text{D7})$$

## Appendix E: Table of pulses

For reference, we here present some relations for other pulse functions.

Name	$\varphi(s)$	$\mathcal{F}[\varphi](\theta)$	$\rho_\varphi(s)$	$\varrho_\varphi(\theta)$
One-sided exponential	$\begin{cases} 0, & s < 0 \\ \exp(-s), & s \geq 0 \end{cases}$	$(1+i\theta)^{-1}$	$\exp(- s )$	$2(1+\theta^2)^{-1}$
Symmetric exponential	$\exp(- s )$	$2(1+\theta^2)^{-1}$	$2\exp(- s )[1+ s ]$	$8(1+\theta^2)^{-2}$
Sech	$\operatorname{sech}(s)/\pi$	$\operatorname{sech}[\pi\theta/2]$	$s \operatorname{csch}(s)$	$\pi^2 \operatorname{sech}[\pi\theta/2]^2/2$
Gauss	$\exp(-s^2/2)/\sqrt{2\pi}$	$\exp(-\theta^2/2)$	$\exp(-s^2/4)$	$2\sqrt{\pi} \exp(-\theta^2)$

A few reasonable results for the infinite sums can be obtained:

Name	$\sum_{m=-\infty}^{\infty} \rho_\varphi(m/\gamma)$
One-sided exponential	$\coth\left(\frac{1}{2\gamma}\right)$
Symmetric exponential	$2\coth\left(\frac{1}{2\gamma}\right) + \frac{1}{\gamma} \operatorname{csch}\left(\frac{1}{2\gamma}\right)^2$

## Appendix F: Representation of delta functions under finite sampling

In this contribution, we frequently plot delta functions superposed on a waveform. A true representation of a continuous-time delta function would be a line extending out of the plot domain. Alternatively, we could indicate the delta spikes by arrows or stars on the ends. The first solution does not give an indication of the amplitude of the delta, while the second makes for very busy figures.

We have instead elected to represent the Dirac delta by its discrete analog, the Kronecker delta. For  $t \rightarrow \Delta_t n$ , we have  $\omega = 2\pi f \rightarrow 2\pi m/\Delta_t$ . A Dirac delta at a given angular frequency  $\omega_*$  is then given by  $\delta(\omega - \omega_*) = \delta(2\pi(m - k)/\Delta_t) = \frac{\Delta_t}{2\pi} \delta_{m-k}$  where  $k$  is the nearest integer to  $\Delta_t \omega_*/2\pi$ . That is, the Dirac delta is approximated as a boxcar of width equal to the sampling step and a height equal to the inverse of the sampling step. This indicates the amplitude of the delta spikes, separates them from any superposed functions and tends to better approximations for finer sampling.

## REFERENCES

- <sup>1</sup>P. Atten, J. C. Lacroix, and B. Malraison, *Phys. Lett. A* **79**, 255 (1980).
- <sup>2</sup>U. Frisch and R. Morf, *Phys. Rev. A* **23**, 2673 (1981).
- <sup>3</sup>H. S. Greenside, G. Ahlers, P. C. Hohenberg, and R. W. Walden, *Physica D* **5**, 322 (1982).
- <sup>4</sup>D. S. Broomhead and G. P. King, *Physica* **10D**, 217 (1986).
- <sup>5</sup>A. Brandstater and H. L. Swinney, *Phys. Lett. A* **35**, 2207 (1987).
- <sup>6</sup>C. L. Streett and M. Y. Hussaini, *Applied Numerical Mathematics* **7**, 41 (1991).
- <sup>7</sup>D. E. Sigeti, *Physica D* **82**, 136 (1995).
- <sup>8</sup>D. E. Sigeti, *Phys. Rev. E* **52**, 2443 (1995).
- <sup>9</sup>M. R. Paul, M. C. Cross, P. F. Fischer, and H. S. Greenside, *Phys. Rev. Lett.* **87**, 154501 (2001).
- <sup>10</sup>C. L. E. Franzke, S. M. Osprey, P. Davini and N. W. Watkins, *Sci. Rep.* **5**, 9068 (2015).
- <sup>11</sup>D. C. Pace, M. Shi, J. E. Maggs, G. J. Morales, and T. A. Carter, “Exponential frequency spectrum in magnetized plasmas” *Phys. Rev. Lett.* **101**, 085001 (2008).
- <sup>12</sup>D. C. Pace, M. Shi, J. E. Maggs, G. J. Morales, and T. A. Carter, “Exponential frequency spectrum and Lorentzian pulses in magnetized plasmas” *Phys. Plasmas* **15**, 122304 (2008).

- <sup>13</sup>G. Hornung, B. Nold, J. E. Maggs, G. J. Morales, M. Ramisch, and U. Stroth, “Observation of exponential spectra and Lorentzian pulses in the TJ-K stellarator” *Phys. Plasmas* **18**, 082303 (2011).
- <sup>14</sup>J. E. Maggs and G. J. Morales, “Origin of Lorentzian pulses in deterministic chaos” *Phys. Rev. E* **86**, 015401 (2012).
- <sup>15</sup>J. E. Maggs, T. L. Rhodes, and G. J. Morales, “Chaotic density fluctuations in L-mode plasmas of the DIII-D tokamak” *Plasma Phys. Contr. Fusion* **55**, 085014 (2013).
- <sup>16</sup>Z. Zhu, A. E. White, T. A. Carter, S. G. Baek, and J. L. Terry, “Chaotic edge density fluctuations in the Alcator C-Mod tokamak” *Phys. Plasmas* **24**, 042301 (2017).
- <sup>17</sup>G. Decristoforo, A. Theodorsen, and O. E. Garcia, ‘Intermittent fluctuations due to Lorentzian pulses in turbulent thermal convection’ *Phys. Fluids* **32**, 085102 (2020).
- <sup>18</sup>G. Decristoforo, A. Theodorsen, J. Omotani, T. Nicholas, and O. E. Garcia, “Intermittent fluctuations due to Lorentzian pulses in turbulent thermal convection” *Phys. Fluids* **32**, 085102 (2020).
- <sup>19</sup>N. Ohtomo, K. Tokiwano, Y. Tanaka, A. Sumi, S. Terachi, and H. Konno, “Exponential characteristics of power spectral densities caused by chaotic phenomena” *J. Phys. Soc. Japan* **64**, 1104 (1995).
- <sup>20</sup>J. E. Maggs and G. J. Morales, “Generality of deterministic chaos, exponential spectra, and Lorentzian pulses in magnetically confined plasmas” *Phys. Rev. Lett.* **107**, 185003 (2011).
- <sup>21</sup>J. E. Maggs and G. J. Morales, “Exponential power spectra, deterministic chaos and Lorentzian pulses in plasma edge dynamics” *Plasma Phys. Contr. Fusion* **54**, 124041 (2012).
- <sup>22</sup>J. D. Farmer, *Physica D* **4**, 366 (1982).
- <sup>23</sup>A. Libchaber, S. Fauve, and C. Laroche, *Physica D* **7**, 73 (1983).
- <sup>24</sup>E. F. Stone, *Phys. Lett. A* **148**, 434 (1990).
- <sup>25</sup>T. Klinger, A. Latten, A. Piel, G. Bonhomme, T. Pierre, and T. Dudok de Wit, *Phys. Rev. Lett.* **79**, 3913 (1997).
- <sup>26</sup>B. Mensour and A. Longtin, *Physica D* **113**, 1 (1998).
- <sup>27</sup>L. A. Safonov, E. Tomer, V. V. Strygin, Y. Ashkenazy, and S. Havlin, *Chaos* **12**, 1006 (2002).
- <sup>28</sup>O. E. Garcia and A. Theodorsen, “Power law spectra and intermittent fluctuations due to

- uncorrelated Lorentzian pulses” *Phys. Plasmas* **24**, 020704 (2017).
- <sup>29</sup>O. E. Garcia and A. Theodorsen, “Skewed Lorentzian pulses and exponential frequency power spectra” *Phys. Plasmas* **25**, 014503 (2018).
- <sup>30</sup>O. E. Garcia and A. Theodorsen, “Intermittent fluctuations due to uncorrelated Lorentzian pulses” *Phys. Plasmas* **25**, 014506 (2018).
- <sup>31</sup>E. Parzen, *Stochastic processes* (Holden-Day, Oakland, CA, 1962).
- <sup>32</sup>H. L. Pécseli, *Fluctuations in Physical Systems* (Cambridge University Press, Cambridge, 2000).
- <sup>33</sup>S. O. Rice, “Mathematical analysis of random noise” *Bell Sys. Tech. J.* **23**, 282 (1944).
- <sup>34</sup>O. E. Garcia, “Stochastic modeling of intermittent scrape-off layer plasma fluctuations” *Phys. Rev. Lett.* **108**, 265001 (2012).
- <sup>35</sup>R. Kube and O. E. Garcia, “Convergence of statistical moments of particle density time series in scrape-off layer plasmas” *Phys. Plasmas* **22**, 012502 (2015).
- <sup>36</sup>A. Theodorsen and O. E. Garcia, “Level crossings, excess times, and transient plasma-wall interactions in fusion plasmas” *Phys. Plasmas* **23**, 040702 (2016).
- <sup>37</sup>O. E. Garcia, R. Kube, A. Theodorsen, and H. L. Pécseli, “Stochastic modelling of intermittent fluctuations in the scrape-off layer: Correlations, distributions, level crossings, and moment estimation” *Phys. Plasmas* **23**, 052308 (2016).
- <sup>38</sup>O. E. Garcia and A. Theodorsen, “Auto-correlation function and frequency spectrum due to a super-position of uncorrelated exponential pulses” *Phys. Plasmas* **24**, 032309 (2017).
- <sup>39</sup>A. Theodorsen, O. E. Garcia, and M. Rypdal, “Statistical properties of a filtered Poisson process with additive random noise: distributions, correlations and moment estimation” *Phys. Scripta* **92**, 054002 (2017).
- <sup>40</sup>A. Theodorsen and O. E. Garcia, “Level crossings and excess times due to a superposition of uncorrelated exponential pulses” *Phys. Rev. E* **97**, 012110 (2018).
- <sup>41</sup>A. Theodorsen and O. E. Garcia, “Probability distribution functions for intermittent scrape-off layer plasma fluctuations’ *Plasma Phys. Contr. Fusion* **60**, 034006 (2018)
- <sup>42</sup>M. Overholt, A Course in Analytic Number Theory. American Mathematical Society (AMS) 2014 ISBN 978-1-4704-1706-2.
- <sup>43</sup>S. Bochner, Lectures on Fourier Integrals, Annals of Math. Studies 42, Princeton University press, Princeton, NJ, 1959
- <sup>44</sup>L. Grafakos, “Classical Fourier Analysis”, <https://doi.org/10.1007/978-0-387-09432-8>

<sup>45</sup>E. M. Stein and G. Weiss, “Introduction to Fourier Analysis on Euclidian Spaces”, Princeton University Press, Princeton, NJ, 1971

<sup>46</sup>I. Richards and H. Youn, “Theory of Distributions”, Cambridge University Press,  
<https://doi.org/10.1017/CBO9780511623837>



# Paper III: Numerical turbulence simulations of intermittent fluctuations in the scrape-off layer of magnetized plas- mas

G. Decristoforo, A. Theodorsen, J. Omotani, T. Nicholas, and O. E. Garcia,  
Submitted to Physics of Plasmas on 15.2.2021,  
Available online: arXiv:2102.04723 [physics.plasm-ph]



## Numerical turbulence simulations of intermittent fluctuations in the scrape-off layer of magnetized plasmas

Cite as: Phys. Plasmas **28**, 072301 (2021); <https://doi.org/10.1063/5.0047566>

Submitted: 15 February 2021 . Accepted: 10 June 2021 . Published Online: 01 July 2021

 G. Dechristoforo,  A. Theodorsen,  J. Omotani,  T. Nicholas, and  O. E. Garcia



View Online



Export Citation



CrossMark





# Paper IV: Blob interactions in 2D scrape- off layer simulations

G. Dechristoforo, F. Militello, T. Nicholas, J. Omotani, C. Marsden, N. Walkden  
and O. E. Garcia,  
Physics of Plasmas **27**, 122301 (2020),  
doi:10.1063/5.0021314



## Blob interactions in 2D scrape-off layer simulations

Cite as: Phys. Plasmas 27, 122301 (2020); <https://doi.org/10.1063/5.0021314>

Submitted: 10 July 2020 . Accepted: 26 October 2020 . Published Online: 01 December 2020

 G. Decristoforo,  F. Militello,  T. Nicholas,  J. Omotani,  C. Marsden,  N. Walkden, and  O. E. Garcia



[View Online](#)



[Export Citation](#)



[CrossMark](#)

AIP Advances

Fluids and Plasmas Collection

[READ NOW](#)